A Combined Near-field Scanning Microwave Microscope and Transport Measurement System for Characterizing Dissipation in Conducting and High-T_c Superconducting Films at Variable Temperatures

Jonathan Reyes Dizon
BS Applied Physics, University of the Philippines Los Baños, 1997
MS Physics, University of Kansas, 2006

Submitted to the Department of Physics and Astronomy
and the Faculty of the Graduate School of the University of Kansas
in partial fulfillment of the requirements for the degree of
Doctor of Philosophy

Thesis Committee:

_____
Judy Z. Wu, Ph.D (Chair)

_____
Siyuan Han, Ph.D

_____
Hui Zhao, Ph.D

_____
Phil Baringer, Ph.D

_____
Carey Johnson, Ph.D

Date of Defense: April 9, 2009

The Dissertation Committee for Jonathan Dizon certifies that

This is the approved version of the following dissertation:

A Combined Near-field Scanning Microwave Microscope and Transport Measurement System for Characterizing Dissipation in Conducting and High-T_c Superconducting Films at Variable Temperatures

Thesis Committee Chair:

_____

Judy Z. Wu, Ph.D

Date Signed: _____

Abstract

Identifying defects and non-superconducting regions in high-temperature superconductors (HTS) is of great importance because they limit the material's capability to carry higher current densities and serve as nucleation spots for "hot spots" that can evolve over time and drive a HTS from superconducting (SC) to normal state. A technique that combines near-field scanning microwave microscopy (NSMM) with transport measurement was developed to image defects and non-uniformities at room temperature and detect low-level dissipation at low temperatures. At room temperature, macroscopic and microscopic defects in both conducting and HTS films were clearly identified and imaged with adequate sensitivity and resolution. At low temperatures, low-level dissipation was detected by observing the NSMM's response during the HTS' transition from SC to normal state. Measuring the time-dependent self-heating effect due to a bias current at a fixed temperature provided insight into the dynamics of thermal instability due to hot-spot nucleation. When the HTS is far from the transition state, a bi-modal evolution of the thermal quench was observed beginning with a nucleation of a local hot spot followed by a spreading/coalescence of them via self-heating. When the HTS is brought closer to transition by increasing either temperature or bias current, this effect is diminished due to faster hot spot growth and continuous spread by self-heating. Observations were obtained for both the bulk and grain boundary regions of a HTS.

Acknowledgements

"And we know that in all things God works for the good of those who love Him, who have been called according to His purpose." *Romans 8: 28*

The completion of this work would not have been possible without these people who shared their time, talent and resources to me. I would like to take this opportunity to express my sincerest gratitude to …

Prof. Judy Wu, my adviser, for all the encouragements, support and knowledge that she willingly imparted to me during the course of this study. I thank you, too, for believing in me.

Prof. Siyuan Han, Prof. Hui Zhao, Prof. Phil Baringer and ***Prof. Carey Johnson***, my dissertation committee members, for their invaluable insights and constructive criticism of my work.

Shramana, for her work on the simulation and help with the lithography of some samples.

Doc Aga, for the invaluable knowledge, tutorials and hands-on assistance in the lab.

Xiang, for the help in the fabrication and preparation of my samples.

my professors in the Department, for all the challenges, knowledge and teaching me how to think and work like a true physicist.

Teri, Tiffany, Tess, Kim, Allan, Zach, John, Doug and Nicky, the Department staff, for all the technical help and support.

Rose, Hua, Javier, Ronald, Xiang, Zhuangzhi, Rongtao, Xin, Shramana, Lalani, Caitlin, Dan, Allan, Jesse, and Jason, my laboratory group mates, for all the discussions, experiments, gimmicks, camaraderie and endless encouragements. Physics is fun, but it won't be as much memorable and easier without you guys.

Kuya Robert, Ate Rachel, Kuya Ronald, Ate Anna, Kuya Jhun, Ate Bhev, Kuya Brian, Ate Cheryl, Kuya Darin, Ate Jackie, Rose, Ate Lynn, Julius, Carl, Robert, Aileen, Maila, Ferdz, Nette and Joseph, my small circle of Filipino friends in Lawrence, for all the invited dinners, cookouts, movies, conversations, road trips, gimmicks and encouragements. You always gave me a taste of home with your presence and friendships.

Fr. Steve, Fr. Mitchell, Fr. Zach, Fr. Brian, Fr. James, Sr. Susan, Sr. Elena, Sr. Loredana, Sr. Clara, Sr. Debbie, all the staff and students from the St. Lawrence Catholic Campus Center for providing a healthy and life-giving community that fosters growth in faith, spirituality and active participation in the Catholic Church … for making me realize my true vocation in life.

Jimmy, Susan, Jomar and Jeph, my parents and my brothers, for believing in me, supporting me and loving me … from a thousand miles away.

.. and finally to ***God***, my Creator and personal savior, for the strength, divine inspiration and intervention that kept me going during the most difficult times of my life … for a second chance, for which I am truly grateful.

Jonathan Reyes Dizon
May 2009

Contents

List of Figures

Chapter 1

Introduction and Motivation

For the past several decades, the field of scanning probe microscopy (SPM) has developed enormously and spawned unique and innovative techniques to explore the micrometer to nanometer-scale domain. The fact that its own growth pushed the advancement of other major fields of study such as physics, chemistry and biology makes SPM a very important and indispensable tool for conducting both fundamental and applied research. Non-destructive and non-invasive evaluation of materials is one such area that has become increasingly popular because it allows study of the sample's different properties while keeping the integrity and structure of the material intact. This study proposes a microwave scanning probe technique that is capable of multi-variable imaging of current-obstructing defects at room temperature and detecting low-level dissipation at cryogenic temperatures. This chapter will provide an overview of the near-field scanning microwave microscopy/microscope (NSMM) technique, its possible unique use for imaging dissipation as compared to existing techniques and some background information on grain boundaries in superconductors where the NSMM can be applied to detect low-level dissipation.

1.1 Brief Overview of Scanning Probe Microscopy

Scanning probe microscopy (SPM) refers to a family of powerful imaging techniques that utilizes a probe or tip positioned very close to the sample to measure localized properties that depend on the nature of interaction between the sample and the probe. As the probe is scanned across the surface, a one-dimensional profile (1D) or a two-dimensional (2D) map of the sample properties can be obtained. The sample surface morphology usually forms one aspect of the image, but images can also be collected to show the other surface properties such as mechanical, electrostatic, optical or magnetic.

The origin of SPM can be traced back to the invention of the scanning tunneling microscope (STM) in 1981 by two scientists from IBM: Binnig and Rohrer [Binnig 1982]. Five years later, they were awarded the Nobel Prize in Physics for their efforts and Binnig, along with Quate and Gerber [Binnig 1986], developed yet another popular microscopic imaging technique: the atomic force microscope (AFM). While the use of STM is restricted to imaging conducting surfaces and samples because it relies on tunneling electrons from the probe tip to the sample, the AFM is in principle capable of imaging both conducting and non-conducting surfaces because it is based on the force of interaction between atoms at the tip and atoms at the sample surface. To this date, numerous versions of SPM [Weisendanger 1994, Meyer 2004] with unique imaging capabilities have emerged and their applications have exponentially

increased as well spanning diverse fields that include physics, chemistry, geology, medicine, and biology.

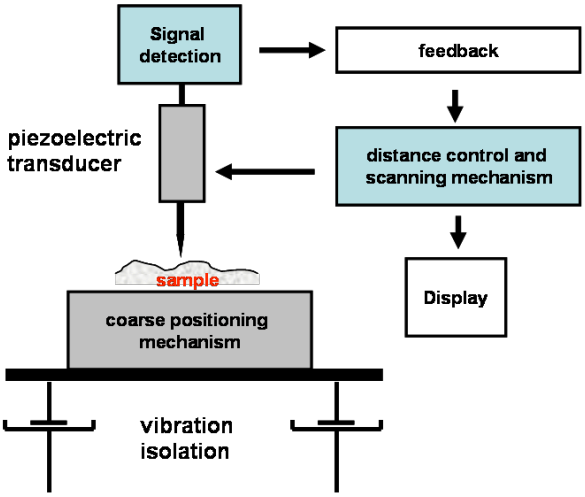

Fig 1.1 Schematic diagram of a basic SPM set-up.

Figure 1.1 depicts a standard schematic set-up for a scanning probe microscopy system. A microscopic probe such as a sharpened tip is attached to a piezoelectric x-y-z transducer capable of moving the tip across or towards the surface of a sample in micrometer-scale or even atomic scale resolution. The sample to be scanned or imaged is fixed right below the tip and may be placed on a coarse positioning mechanism in case there is a need to move the sample over millimeter distances. For other techniques, like AFM, the probe may be fixed while the sample is the one attached to the piezoelectric transducer. The signal detected from the probe tip is dependent on the tip-to-sample distance. If this distance needs to be maintained at a constant height, a feedback mechanism is employed to adjust this height during scanning. The relevant signal is then recorded as a function of spatial position and a 1D profile or 2D map of the physical property can be obtained using available signal or image processing techniques and software. In order to achieve high-resolution images, mechanical stability and isolation from vibration are also important factors to consider.

1.2 Near-field Scanning Microwave Microscopy (NSMM)

1.2.1 Brief History of NSMM

The classical diffraction limit, known as the Abbe barrier, indicates that the resolving power of an optical microscope or any other instrument based on the propagation of electromagnetic radiation over distances greater than the wavelength (λ) is limited to $\lambda/2$. This follows from the Fourier analysis of the optical image formation and leads to the conclusion that spatial frequencies greater than $1/\lambda$, known as evanescent waves, decay exponentially. In principle, a device or technique that manages to recover all the spatial frequency components of the original signal, including the decaying components, would be able to focus the radiation to a sub-wavelength spot and obtain an image with sub-wavelength dimension. One such technique was proposed by Synge in 1928 where he developed a scanning optical microscope which used the near-field evanescent fields for detection [Synge 1928]. When a point-like field source or aperture-based illumination is brought in close proximity to a sample (see Fig 1.2), the evanescent field is still strong enough (for most cases, tip-to-sample separations of up to $\lambda/100$) to substantially interact with the sample which allows imaging at a resolution surpassing the Abbe barrier. This idea spawned efforts in the development of near-field microscopy using evanescent microwave fields [Sohoo 1962, Ash 1972] in the early 60's and 70's and later using visible light [Pohl 1984, Lewis 1984] in the early 80's. The latter led to the development of near-field scanning optical microscopy (NSOM).

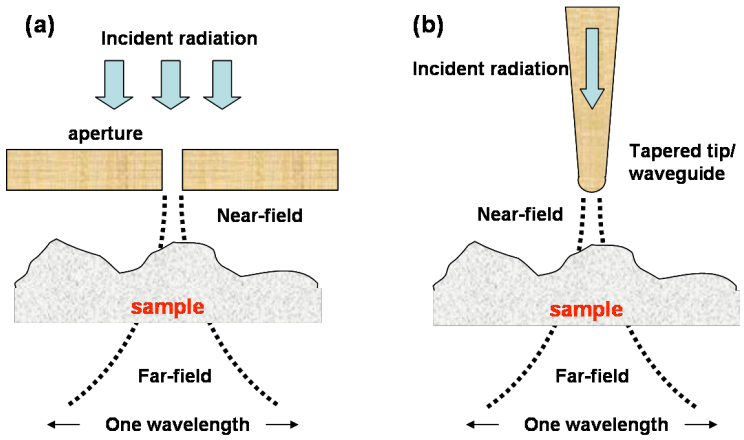

Fig.1.2 Illustration of evanescent near-fields for high resolution imaging using (a) aperture or (b) tapered tip / waveguide

1.2.2 Resonant NSMM Designs

Microwave near-field probes are either broadband or resonant. The broadband probes typically use electromagnetic waveguides while the resonant probes normally employ a resonant cavity that is coupled through a sub-wavelength-sized probe. Resonant probes are more sensitive because the signal-to-noise ratio in a resonator increases with resonator quality factor (**Q**). Thus, they are very efficient in the narrow frequency band for which they were designed. This increase in sensitivity and field strength is accompanied by a narrower frequency band, with the drop in amplitude depending on **Q**, which results from the shift in resonant frequency with different dielectric environments [Rosner 2002]. Four independent research groups developed different resonant probe designs and published their works in close succession to one another starting in 1993.

Tabib-azar *et.al*. introduced a **microstrip** or **stripline resonator** for near-field microwave microscopy in his first two publications. The first [Tabib-Azar 1993] involved fabricating a quarter-wavelength microstrip line resonator operating at a frequency of 1 GHz as illustrated in Fig 1.3(a). The conductor is tapered to a fine point at the end of the substrate where a short wire representing the probe is connected. This wire can either be attached to the backplane (magnetic probe) or an open circuit (electric probe) as depicted in Fig 1.3(b) and 1.3(c). They used the magnetic probe to scan across the width of a 254 μm-diameter wire and obtained a resolution between 400 – 600 μm. The electric dipole probe, meanwhile, was used to scan across the width of a patterned 100 μm-wide Al strip. They found the resolution for this probe to be 100 μm. In their second paper [Tabib-Azar 1999[a]], they modified the geometry and used a stripline instead of a microstrip. Figure 1.3(d) shows this configuration where the signal conductor is sandwiched between two substrates and backed by two ground planes.

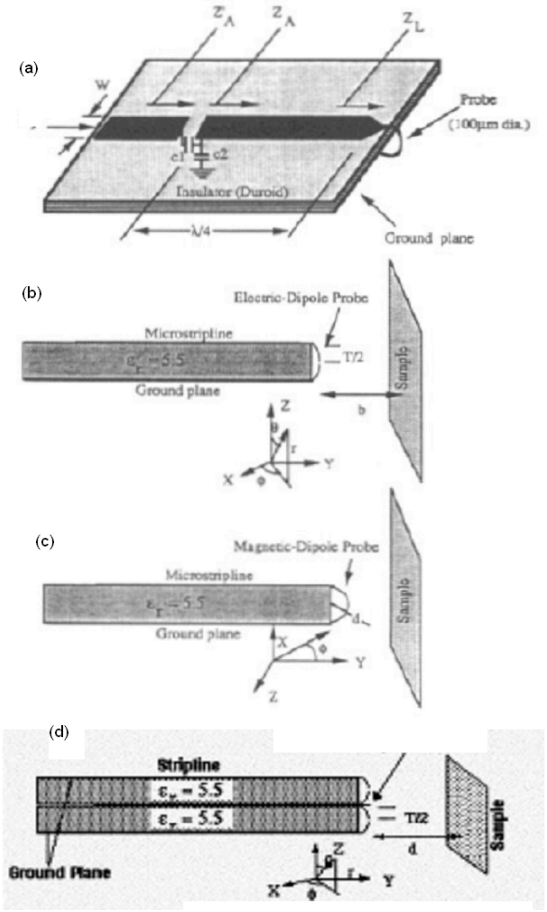

Fig. 1.3 Schematic drawings of (a) microstrip resonator probe including (b) electric dipole and (c) magnetic dipole probe configurations. (d) Stripline variant of the resonator probe [Tabib-azar 1993].

The resonator follows the previous design and a sharp chemically-etched stainless steel tip with a diameter of approximately 1-2 μm is connected at the tapered end to be used as probe. With this probe, they were able to identify 2-μm wide lines in a MEMS chip with a reported resolution of 0.4 μm at a 1 GHZ operating frequency. Their succeeding publications reported a handful of different applications for the resonant NSMM they developed [Tabib-Azar 1999[c-g], Tabib-Azar 2000].

A group from Jerusalem led by Golosovsky and Davidov were able to develop another class of NSMMs which are based on **resonant slots**. Their first design [Golosovsky 1996] utilizes a rectangular hollow waveguide with a narrow resonant slot (see Fig.1.4(a)) as a near-field source with a high transmission coefficient and resolution constrained only by the dimension of the slot. They were able to demonstrate 70-100 μm resolution at an operating frequency of 80 GHz. However, this design has an unequal resolution in the x and y axis thus requiring additional deconvolution techniques to reconstruct the image. The design was later modified into a cylindrical waveguide [Lann 1999[b]] with a hemispherical insert that contains the slot (Fig. 1.4(b)). The curvature of the hemisphere structure ensures that only a small portion of the slot will contribute to detection since the outer parts of the slot will be positioned farther away from the sample. This probe was integrated into a cryogenic environment so that it can operate as a transmitting/receiving antenna that is capable of measuring local resistance as a function of temperature. They obtained a resolution of ~ $\lambda/60$ to $\lambda/160$ at an operating frequency of 90 GHz.

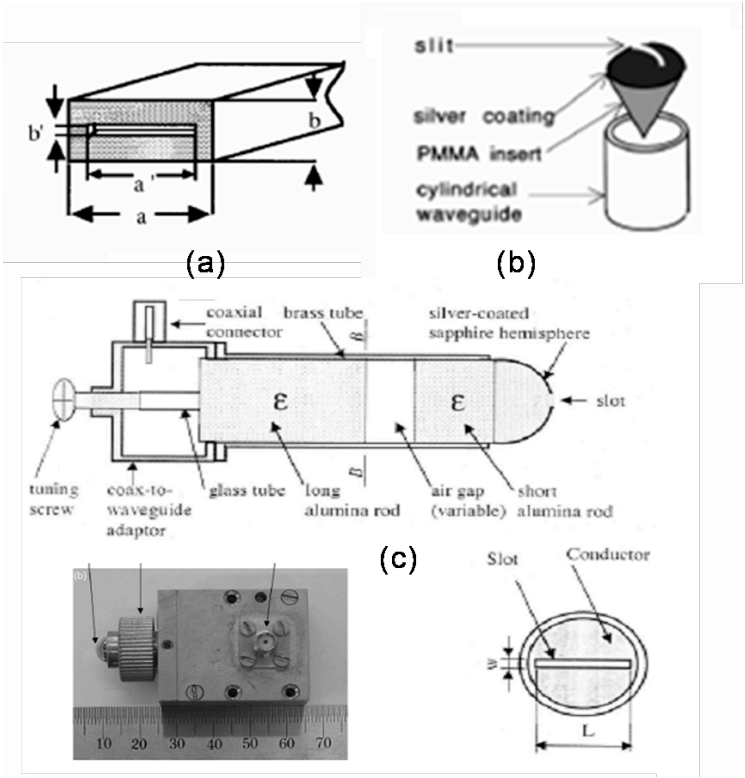

Fig. 1.4 Resonant slot microwave probes: (a) hollow rectangular waveguide design, (b) cylindrical antenna with slot, and (c) dielectric resonator with slot [Golosovsky 1996, Lann 1999[b], Abu-Teir 2001].

Several years later, another modification in the design was implemented [Abu-Teir 2001]. The narrow, microfabricated slot now sits on the convex surface of a dielectric resonator mounted on a cylindrical waveguide as shown in Figure 1.4(c). The dielectric-filled waveguide has a variable gap that allows for tunable coupling to effectively match the impedance of the resonant slot and the feeding waveguide. They reported a spatial resolution of 1-10 μm at an operating frequency of 25-30 GHz for this modified probe.

At about the same time, a group of researchers from the Lawrence Berkeley National Laboratory led by Wei and Xiang independently developed another design for a NSMM based on **coaxial cavity resonators** [Wei 1996]. A sharp STM-like tip, obtained by tapering the center conductor of a quarter-wavelength cavity, is used as a point-like field emitter. The center conductor is enclosed in a cylindrical shielding plate except for the tip which protrudes out from a small circular hole of diameter 1-2 mm. The resolution of this probe depends only on the diameter of the sharp tip since the evanescent field intensity is much stronger at the tip apex compared to the intensity radiated from the aperture hole or the tapered portion of the tip. With this probe, they were able to demonstrate spatial resolution of approximately 5 μm at an operating frequency between 500 MHz and 1 GHz. Gao later improved this design by decreasing the size of the aperture and sharpening the tip further [Gao 1997]. A small sapphire disk with inner diameter of ~ 100-200 μm was inserted in the aperture area (see Fig. 1.5). A thin metal coating was also grown on the exterior side of the sapphire disk to shield far-field propagating signals. A resolution of around 100 nm was reported for this probe operating at 2.3 GHz.

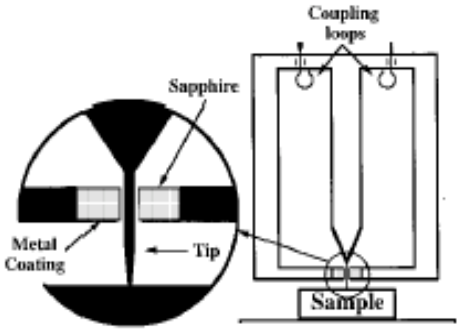

Fig 1.5 Schematic of microwave probe based on a coaxial cavity resonator. Inset: the modified design with the sapphire disk [Gao 1997].

Finally, a group from the University of Maryland led by Anlage and Wellstood published several papers on the various applications of their NSMM constructed from an **open-ended coaxial resonator** [Vlahacos 1996]. The initial design of this probe, as presented by Vlahacos *et al.*, consist of an open-end rigid coaxial resonator with an inner diameter of 100 μm operated at a frequency between 7.5 – 12.4 GHz. The coaxial cable, as shown in Fig. 1.6, can be modeled as a resonant coaxial transmission line terminated at the sample end with a capacitance that represents the interaction between the probe's inner conductor and the sample surface. As the probe scans through the sample surface, the variation in the value of this capacitance is responsible for the contrast in the microwave properties. They reported a resolution of 100 μm equivalent to the probe's tip diameter for this set-up. In later works, they were able to increase the spatial resolution of this probe by using a tapered probe tip [Steinhauer 1999, Steinhauer 2000].

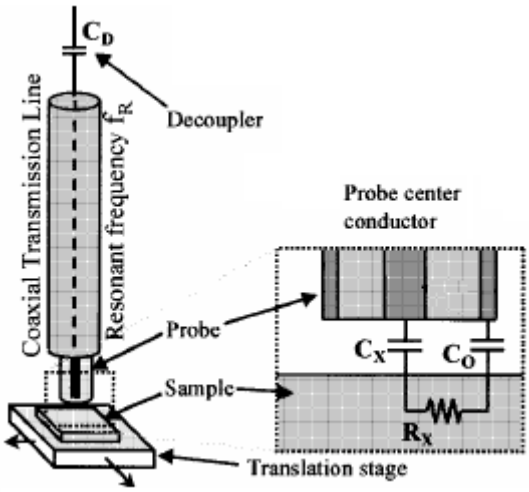

Fig. 1.6 Open-ended coaxial resonator. Inset shows the equivalent circuit model of the probe when brought close to the sample [Steinhauer 1997].

In some cases, it is helpful to obtain maps of several correlated variables to obtain better insight. The first attempt to extend the capability of a NSMM to measure two simultaneous physical properties was made by Aga *et al.* [Aga 2003, 2004]. The group developed a dual-channel scanning microprobe capable of simultaneously mapping the microwave and optical properties of the sample. The probe design was based on a tunable open-ended coaxial resonator with a tapered and metal-coated fiber optic tip, from which microwave and light can be emitted/collected simultaneously. The microwave channel operates at 1.5 GHz and has a spatial resolution of 5-10 μm while the optical channel has a spatial resolution of ~ 1 μm. They used the probe to diagnose the poor performance of a Tl-2212 microwave resonator. An image from the optical channel was able to identify localized spots of higher light transmission possibly corresponding to pinhole-type defects in that specific region. A microwave image of the same region shows non-uniformity in the microwave loss.

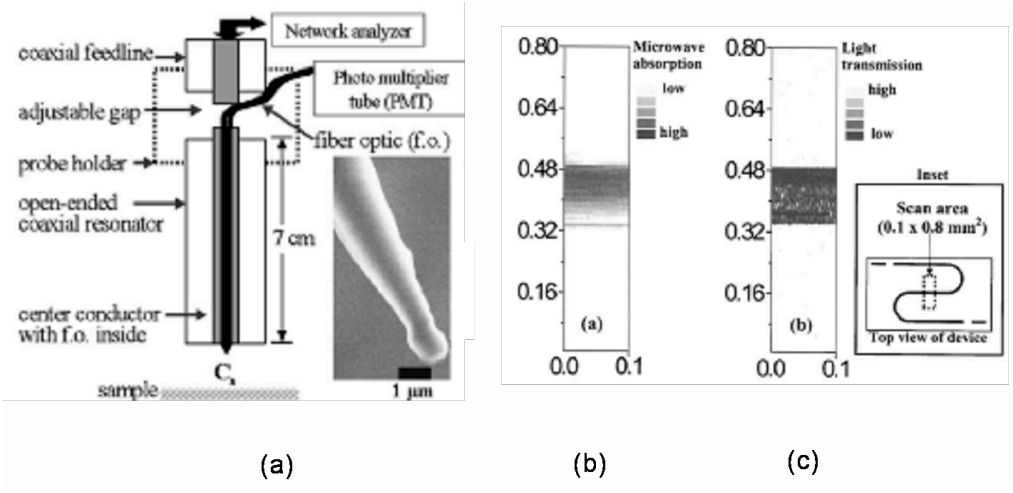

Fig.1.7 (a) Schematic design of the microwave/optical dual probe. (b) Microwave and (c) optical image of the center portion of a Tl-2212 microwave resonator taken by the dual probe at room temperature [Aga 2003,2004]

Therefore, the poor performance of the resonator due to non-uniformity in the microwave properties was confirmed by the optical channel as well. Figure 1.7 shows the schematic of the probe and the images of the resonator region obtained from scanning at room temperature.

1.2.3 Applications of NSMM

In conjunction with the construction of the different probe designs by their respective developers came an assortment of interesting applications that led to the realization that this technique can be used to characterize various types of materials. Using their microstrip resonator probe, Tabib-Azar *et al*. experimented with samples covering the entire conductivity range (metallic to insulating) to show the versatility of the technique in imaging conductivity [Tabib-Azar 1999[b]]. Fig.1.8 shows the images obtained by their microstrip probe on (a) dielectric, (b) semiconducting, (c) metallic, (d) magnetic and (e) biological samples.

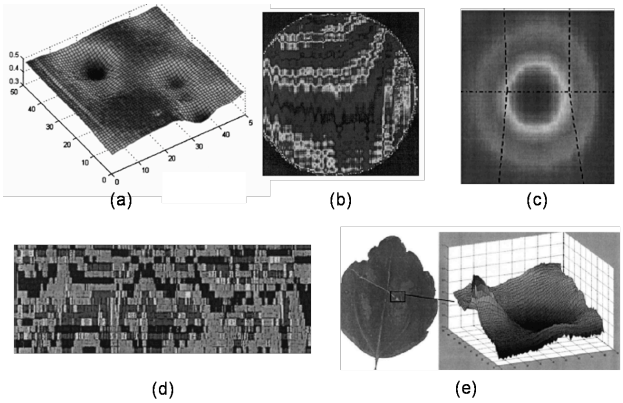

Fig.1.8 Images obtained by a microwave probe: (a) delaminated regions of a carbon dielectric composite, (b) resistive regions in a Si wafer, (c) copper metal with a 2 mm diameter hole, (d) magnetic domains of a hard disk drive and (e) image of a plant leaf region [Tabib-Azar 1999[b]]

In their succeeding publications, they also used the NSMM for several unconventional and innovative sensing applications such as displacement sensing [Tabib-Azar 1999[d]], transient thermography [Tabib-Azar 1999[e]], hydrogen gas sensing [Tabib-Azar 1999[f]] and imaging semiconductor space-charge regions [Tabib-Azar 2000].

The group from Jerusalem, meanwhile, used their resonant-slit type probe to identify regions of a superconductor sample with different oxygen content and regions bombarded by light ions [Lann 1999[b]]. The NSMM was able to detect the changes in the microwave reflectivity across these regions because of the differences in conductivity. They also used the probe to study the temperature dependence of the localized microwave reflectivity in the superconducting samples [Lann 1999[a]]. In their more recent papers [Copty 2004], they were able to use the probe as a microwave emitter to locally heat particular regions of various biological media. They demonstrated the potential use of the NSMM for tissue repair and other biomedical treatments in the future.

The group from Lawrence Berkeley National Laboratory, on the other hand, focused early efforts on using their coaxial resonator-type probe to image a sample's ferroelectric domains by measuring the variations in the dielectric constant [Gao 1998]. Periodic ferroelectric domain structures in crystals have found considerable interest in microelectronic, optic and acoustic applications. However, characterization

of such structures has previously employed destructive techniques and none of them have the ability to analyze variations in the dopant concentration (as provided by the variations in the dielectric constant) which actually gives rise to the formation of the ferroelectric domains. Figure 1.9 shows the images of the linear and non-linear dielectric constants showing the ferroelectric domains. In another publication, they were also able to observe defects in the ferroelectric domain structure induced by growth-instability and lattice-edge dislocations [Lu 1997].

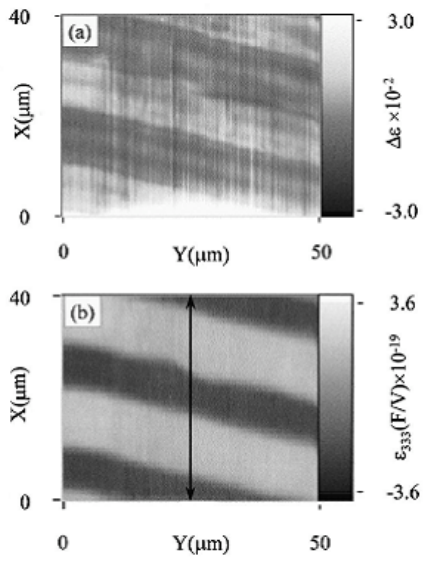

Fig.1.9 (a) Linear and (b) Non-linear dielectric constant images obtained using a coaxial resonator microwave probe by Lu *et al.* [Lu 1997].

The Maryland group led by Anlage provided a systematic approach to demonstrating the capabilities of their microwave resonant probe. Their earlier efforts were geared towards imaging surface resistance [Steinhauer 1997], sheet resistance [Steinhauer 1998] and topography [Vlahacos 1998] of passive samples including conductors and superconductors. Then they also showed that the probe is capable of imaging microwave electric fields [Dutta 1999] and intermodulation fields [Hu 1999] of an active superconducting microstrip resonator. In their later publications, they also provided imaging capability in terms of microwave permittivity and tunability [Steinhauer 1999, Steinhauer 2000], magnetic permeability [Lee 2000], ferroelectric domains [Steinhauer 2001] and even HTS grain boundaries [Lee 2003].

1.2.4 Improving Sensitivity and Spatial Resolution

When a NSMM scans over a particular sample, the detected changes in the microwave properties correspond to changes in the samples properties. However, the response of the probe is extremely sensitive to variations in the tip-to-sample separation. Therefore, for a sample which possesses modulation both in topography and material properties, the image will be dominated by morphological modulation and the information containing modulation in material properties will be buried underneath it. For this reason, several groups worked to address this issue by providing a feedback mechanism that can disentangle the two effects. The Berkeley group implemented a feedback mechanism to control the tip-sample separation based on an analytic model that provides a calibration curve that correlates the microwave response as a function of tip-sample distance for a material of given dielectric constant [Duewer 1999]. From the calibration curve, specific voltage inputs to a piezoelectric transducer are provided to maintain the tip-sample separation given a specific change in resonant frequency. By monitoring the voltage inputs sent to the actuator, images of the topography and microwave properties are obtained simultaneously. The group from Maryland later adopted a similar approach [Tselev 2003] and demonstrated

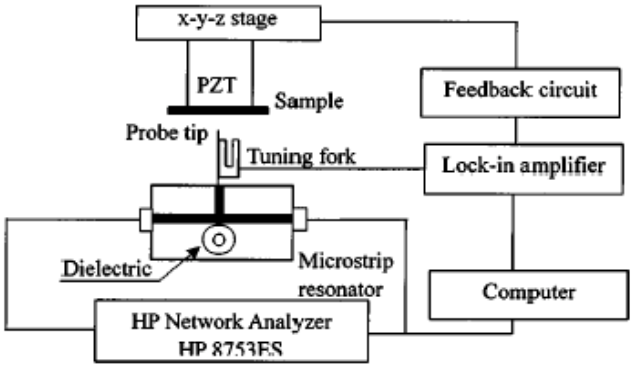

Fig.1.10 Feedback mechanism using a tuning fork as implemented by Kim *et al.* [Kim 2005]

improved sensitivity with the reduction of noise in its images. Another intriguing and unique approach was proposed by a group of researchers from Sogang University in Korea. They demonstrated the use of a tuning fork shear-force feedback method, as shown in Figure 1.10, to control the distance between the tip and the sample [Kim 2005]. A STM-assisted feedback mechanism has also been proposed [Imtiaz 2003].

Another related approach to increase sensitivity and spatial resolution is to provide a mechanism to tune the resonant cavity. This extra feature allows for adjustment to find the best impedance matching condition to fine-tune the resonant frequency. This was earlier integrated in the design of the resonant-slot type probe by the group from Jerusalem [Abu-Teir 2001]. But more recently, the same group from Korea demonstrated that this also works well for a coaxial resonator type probe [Hong 2002, Kim 2003[a]] and a waveguide cavity-type probe [Kim 2004]. Significant improvements in the resolution and sensitivity of the images were observed.

The use of sharp probe tips has also proven to be effective in increasing the spatial resolution of the NSMMs. However, Kim *et al.* showed that while sharp tapered probe tips increase the spatial resolution of the images, the transmission efficiency decreases considerably because of the sharp cone angle resulting in low probe sensitivity [Kim 2003[b]]. They suggested a hybrid probe that consists of a flat shoulder and a reduced length of the tapered part that creates a sort of compromise to optimize both resolution and sensitivity without sacrificing the other. Figure 1.11 shows a

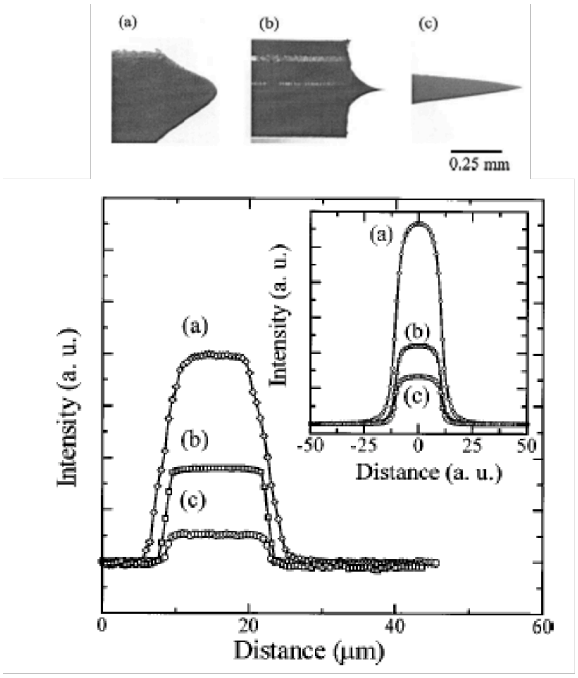

Fig.1.11 Different tip geometries and corresponding signal intensities measured in an experiment conducted by Kim *et al.* (a) round apex probe, (b) hybrid probe and (c) sharp tapered probe [Kim 2003[b]].

rendering of the probe tips along with the results of a one-dimensional scan over a patterned Cr film using the different tips. Tip (a) corresponds to the round apex probe and the scan confirms that this type of probe has the best sensitivity but suffers in providing the sharp transition at the edges. Tip (c) on the other hand is the sharp tapered tip with the small cone angle and small apex. This tip provides the best resolution but suffers from low signal sensitivity. The hybrid probe is given by tip (b) and clearly provides a mix of good sensitivity and high resolution.

1.3 Techniques for Imaging Electrical Current Flow and Dissipation in HTS

Existing techniques for imaging electrical current density or distribution in superconductors can broadly be classified under two categories: ***indirect techniques*** which involve mapping the spatial distribution of the magnetic field and ***direct techniques***, commonly known as "hot spot techniques", which measures the voltage induced on a current-biased sample by localized heating generated by an electron beam or laser.

For indirect techniques, the current distribution is obtained from the magnetic field distribution by numerically solving the Biot-Savart law. Since magnetic field exclusion (Meissner effect) only takes place when the superconductors are below their critical temperature T_c, then low-temperature operation is a requirement for most of these methods. Magneto-optical imaging (MOI) has been previously used to observe the influence of grain boundaries on the flux penetration pattern in YBCO coated conductors and how they serve as barriers to supercurrent flow [Feldmann 2000]. Hall-probe magnetometry was also used to obtain high-resolution images of the local magnetic flux distribution even in the presence of a large applied field [Karapetrov 1999]. A group from Japan was also able to take advantage of the inherent sensitivity of a superconducting quantum interference device (SQUID) sensor to magnetic flux and used it as a scanning probe to map current distributions that contain contributions from both the transport supercurrent and vortex current [Sugimoto 2000]. Figures 1.12(a) and 1.12(b) show the observed magnetic field distribution in the absence and presence of a transport supercurrent, respectively. The magnetic vortices are clearly visible in the first image. The maps on the right correspond to the calculated current distributions.

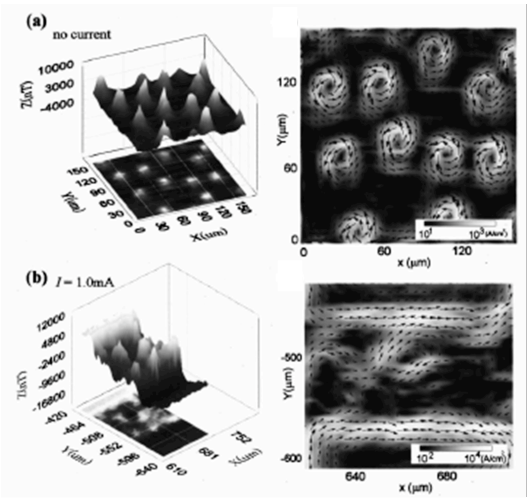

Fig. 1.12 Magnetic field images of a YBCO film in the (a) absence and (b) presence of transport current. Matching calculated current distributions are given on the right. [Sugimoto 2000].

A similar approach is used by magnetic force microscopy (MFM) to image the spatial distribution of the magnetic vortices on a superconducting sample [Hug 1999, Roseman 2002]. Yongsunthon and Rous were even able to use the technique at room temperature to map the current distribution on a current-biased Cr/Au line which contains a slanted slit defect [Yongsunthon 2003, Rous 2004]. A 200 nm resolution was reported.

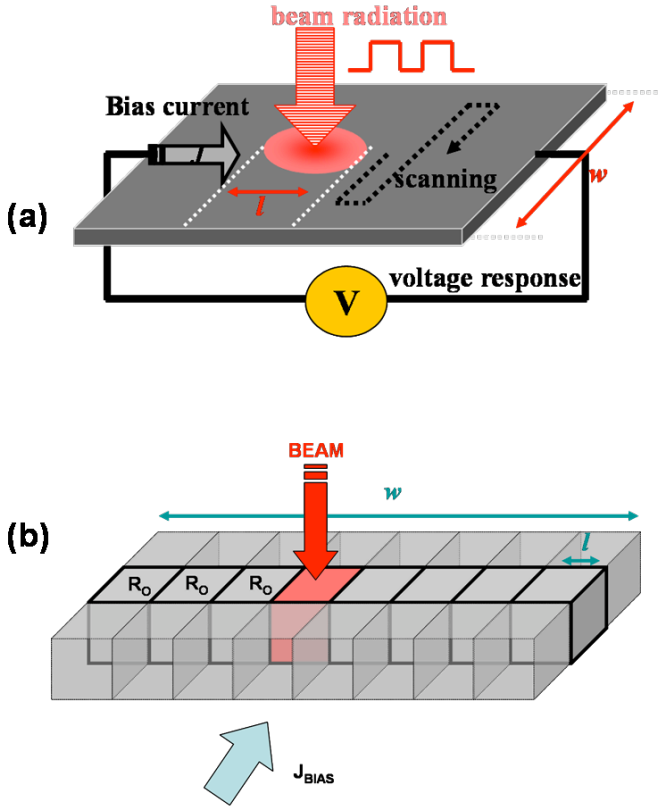

Fig.1.13 (a) Schematic drawing of a hot spot based technique for mapping current distribution. (b) The width of a sample modeled as a network of cells having parallel resistances.

For direct techniques, the principle is based on mapping the spatial distribution of an induced voltage on a current-biased sample by heating a specific spot on the sample

surface. The schematic of the set-up for a hot spot-based technique is shown in Fig. 1.13(a). A focused beam of electrons or laser is directed on a small spot of dimension $\boldsymbol{l}$ on the surface of a sample of thickness $\boldsymbol{t}$ and width $\boldsymbol{w}$ biased with current $\boldsymbol{J_{bias}}$. The effect of heating by a focused laser or electron beam is an increase in temperature at the beam spot and a corresponding increase in the local resistance as given by $\boldsymbol{\Delta R_{local}} = \boldsymbol{(}\partial R/\partial T\boldsymbol{)}\ \boldsymbol{\Delta T}$. At a fixed bias current density $\boldsymbol{J_b}$, Ohm's law gives the measured induced voltage $\boldsymbol{\Delta V}$ in relation to the change in total resistance as $\boldsymbol{\Delta V = I_b\ \Delta R_{total}}$. If the sample is viewed as a network of cells each having resistance $\boldsymbol{R_0}$ and having cubic dimensions of $\boldsymbol{l}$, then the effect of beam radiation can be considered as one of these cells increasing its resistance by $\boldsymbol{\Delta R_{local}}$ (see Fig.1.13(b)). If there are $\boldsymbol{n}$ cells comprising the whole width, then $\boldsymbol{\Delta R_{total}} = (\boldsymbol{\Delta R_{local}} / \boldsymbol{n})$. And since $\boldsymbol{n = w/l}$, we can express the induced voltage as

$$\Delta V = I_{BIAS} \bullet \Delta R_{total} = I_{BIAS} \bullet \left[\left(\frac{l}{wt} \right) \frac{\partial \rho}{\partial T} \Delta T \right]$$

This equation, thus, provides a framework on how to increase the sensitivity of the $\boldsymbol{\Delta V}$ measurement for a fixed-thickness sample because it is linearly proportional to these three terms: (i) the bias current, (ii) the beam spot-sample width ratio, and (iii) heating efficiency of the incident radiation. Since hot-spot techniques rely on detecting an induced voltage due to a corresponding change in the sample's resistance, the ability to detect these small changes in resistance is critical and becomes more challenging when dealing with thicker samples. Furthermore, note that $\boldsymbol{\Delta R_{local}}$ is also dependent on the ratio $\boldsymbol{l/w}$. While a smaller $\boldsymbol{l/w}$ value translates to a

higher spatial resolution, higher sensitivity is required in the detection of ΔV. If the heating is assumed uniform through the film thickness t, a more general expression for ΔV may apply to samples of any given thickness: $\Delta V = J_{bias} l \bullet \frac{\partial \rho}{\partial T} \Delta T$. The hot spot dimension l, therefore, not only dictates the imaging resolution but also affects the signal sensitivity of the induced voltage measurements. While a larger hot spot dimension should increase the sensitivity of the ΔV measurements, the cost is the reduced imaging resolution.

Two major hot spot methods have been developed in the past years. Low-temperature SEM (LTSEM) has been used to image the spatial distribution of the critical current density and grain boundary networks in YBCO ramp-edge Josephson junctions with a resolution of about 1 μm. The focused electron beam of a scanning electron microscope serves as the local heating agent to affect an increase in temperature at the beam position [Marx 1994]. The system, however, is a modified scanning electron microscope and as such is expensive and rather difficult to operate. Furthermore, the technique might be sensitive to magnetic fields that are produced by high-current applications.

These hurdles can be overcome by using a scanning laser instead of an electron beam system. Low-temperature scanning laser microscopy (LTSLM) was first introduced as a method for probing vortex structures and electrical inhomegeneity in Josephson

junctions by Schuerman *et al.* in 1983 [Schuermann 1983]. Divin and Shadrin explored the same applications a decade later and were even able to obtain good resolution for room temperature imaging of electrical inhomegeneities and grain boundaries in YBCO [Divin 1994, Shadrin 1998]. With the rapid development of coated conductors, a number of other groups were able to further develop the same technique to image sources of dissipation and the transport current distribution in HTS thin films [Klein 2002], coated conductors [Abraimov 2004] and even IBAD (ion beam-assisted deposition) tapes [Kiss 2005].

1.4 Grain Boundaries in High-T_c Superconductors (HTS)

The discovery of high-T_c superconductivity in the mid-to-late 1980's generated great excitement among scientists [Lehndorff 2001, Larbalestier 2001]. Widespread applications of superconducting technologies were envisioned due to the practically high critical temperatures (T_c) of these cuprate superconductors. Applications of these superconductors, however, hinged upon another critical property, the transport critical-current density (J_c). The inherent limitation of these materials to carry currents way below its perceived theoretical limit and its unfavorable

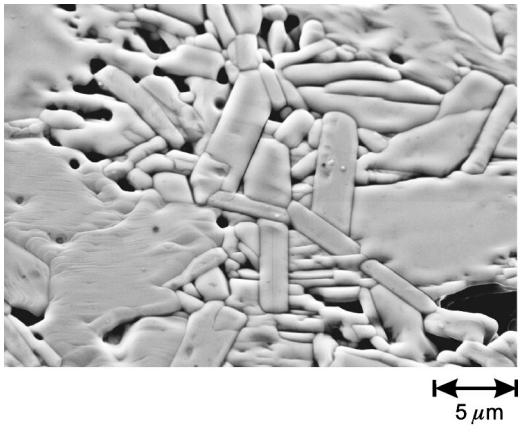

Figure 1.14. SEM micrograph of a poly-crystalline YBCO sample. The grains and their boundaries are clearly visible.

dependence on an applied magnetic field, **H**, has spawned numerous efforts for research to understand and improve these characteristics. This problem is further compounded in polycrystalline samples where J_c is much lower compared to single-crystal samples due to the presence of grain boundary interfaces (Figure 1.14).

Grain boundaries (GBs) are structural defects which interrupt the lattice structure of the adjacent crystals and thereby affect most of the properties of the correlated electron system. Over the years, several mechanisms have been proposed to explain the presence of an experimentally-observed insulating layer at the boundary, which causes a characteristic normal state boundary resistivity of $R_nA \sim 10^{-9}$ to 10^{-7} Ω cm^2 at 4.2K and the strongly angular-dependent J_c [Hilgenkamp 2002].

To understand the behavior of bulk polycrystals, information about the properties of the individual and well-defined interfaces is required. Analyzing properties of individual interfaces in a polycrystalline sample, however, presents a huge challenge due to the inherent complexity of the GB networks and small grain dimension typically on the order of few-to-sub micrometers. The development of bicrystal technology, thus, became necessary as it allows the study of single, well-defined grain boundaries that can be fabricated and analyzed in thin film samples. This technology consists of growing a film epitaxially on a bicrystalline substrate, which contains a grain boundary of a desired configuration. The epitaxial growth of the film allows the grain boundary to be replicated from the substrate to the film. This

technique enables one to fabricate well-defined grain boundaries of many misorientations and to analyze their properties in direct comparison to those of the adjacent grains. There have been other approaches/technologies that have been developed to study grain boundaries which do not require the use of bicrystalline substrates but they will not be discussed as they fall outside the scope of this proposed study.

Grain boundaries are normally classified according to the displacement and the rotation of the adjacent crystals, as shown in Figure 1.15. For rotational GBs, a distinction is made between the tilt and twist components of the misorientation. Here, tilt refers to a rotation around an axis in the plane of the GB while twist refers to a rotation of the crystal grains around the axis perpendicular to the GB plane. A 12^0 [001]-tilt boundary, for example, connects two crystals rotated with respect to each other by 12^0 around the [001] direction (normal to the x-y plane), which is common to both crystals and lies in the GB plane. Furthermore, combinations of tilt and twist components may occur, leading to so-called mixed boundaries [Hilgenkamp 2002].

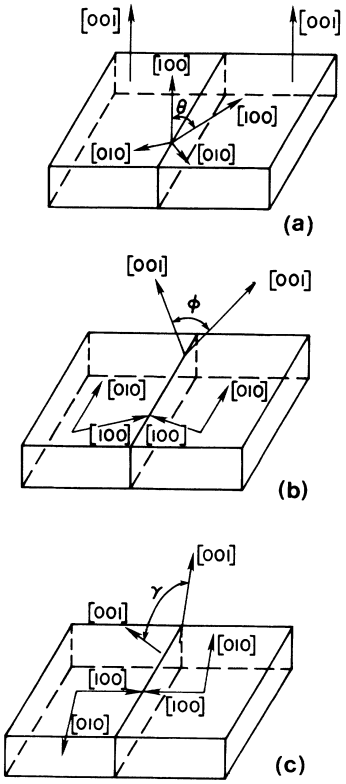

Figure 1.15 Schematic diagram showing crystallography of three grain boundary geometries: (a) [001] tilt boundary, (b) [100] tilt boundary and (c) [100] twist boundary [Dimos 1990].

The microstructure of grain boundaries in HTS has been investigated by several means, of which transmission electron microscopy (TEM), proved to be very useful. From these early studies, it was found that an array of separate dislocations is formed to accommodate the lattice mismatch at small-angle grain boundaries. In standard grain boundary dislocation theory, the distance ***d*** between the dislocations of a certain set is given by Frank's formula: $d = \frac{|b|}{\sin\theta}$ where $|b| = \frac{a}{2}\sqrt{h^2 + k^2 + l^2}$, the magnitude of the Burges vector ***b***. In this expression, ***a*** is the unit cell length of the crystal and ***h,k,l*** are the components of the Burges vector b = <h k l>. The Burges vector represents the magnitude and direction of the lattice distortion of a dislocation in a crystal lattice. It is obtained by comparing a closed contour in the undisturbed crystal and a contour connecting corresponding lattice points around the dislocation, called the Burges circuit. The vector that has to be added to close the Burges circuit, the ***closure failure***, defines the Burges vector. Figure 1.16 illustrates this procedure. In materials of which the unit cell is composed of smaller sub cells, dissociation of the dislocations into partial dislocations can occur, especially for smaller misorientations. For these partial dislocations, the Burges vector is given by a base vector of the sub unit cell, instead of the large base vectors of the complete cell.

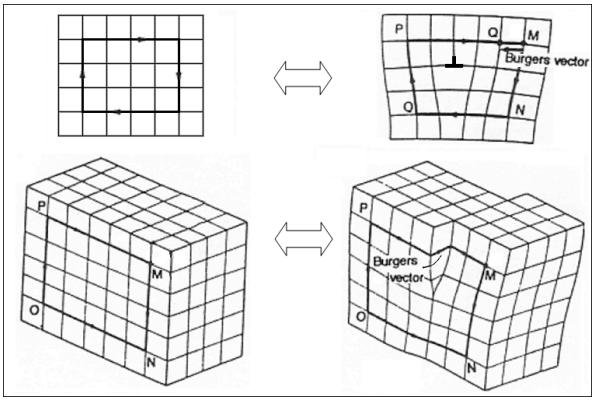

Figure 1.16. Illustration of the Burges vector in a distorted crystal lattice.

This can be the case for high-T_c superconductors, the unit cells of which are composed of stacks of perovskite cells [Hilgenkamp 2002].

As the grain boundary angle increases, the dislocations are spaced closer together until they merge into a continuous interface layer. This layer may be structurally distorted or composed of well-defined structural units as observed by Browning *et al.* [Browning 1996, 1998]. These structural units were observed to be similar to the core structures that make up the isolated dislocations. The resulting width of the non-superconducting regions adjacent to the grains were found based on the arrangements of the ions in the structural units and ranges from 2 Å to 9 Å for misorientation angles between 11^0 and 45^0. For such high-angle GBs, Frank's formula no longer holds and another convenient model used to characterize high-angle boundaries involves defining a coincidence site lattice (CSL). The CSL is the lattice obtained from superimposing the two lattices of the adjacent crystals and can be described by a parameter Σ defined by: $\Sigma = \dfrac{\left|\overrightarrow{C_1} \bullet (\overrightarrow{C_2} \times \overrightarrow{C_3})\right|}{\left|\vec{a} \bullet (\vec{b} \times \vec{c})\right|}$ where a, b and c are the lattice vectors of the crystal grains and C_1, C_2 and C_3 are the primitive vectors of the CSL. A small value of Σ implies that the two grains share many lattice sites at the interface and therefore the boundary is expected to have low energy [Hilgenkamp 2002].

Figure 1.17 shows two images distinguishing between separated and merged dislocations for low-angle and high-angle grain boundaries, respectively. Aside from TEM, spatially-resolved electron energy loss spectroscopy (EELS) has also been used to study the charge carrier concentration at the grain boundary interfaces. Results from these experiments confirm the presence of a layer with a reduced density of holes at the boundary [Browning 1998].

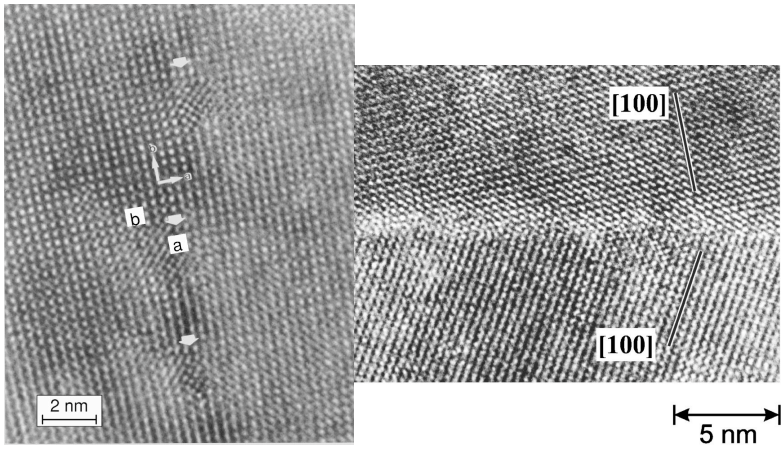

Figure 1.17. Transmission electron micrograph of (a) a 3.5^0 [001]-tilt and a (b) 31^0 [001]-tilt grain boundary in a YBCO film. Three dislocations are presented by arrows in (a) while the horizontal boundary interface is visible in (b) [Gao 1991, Babcock 1994].

Typical plots of the current density versus voltage (J_c-V) are shown in Figure 1.18(a), depicting curves obtained from a single YBCO thin film that contains 2 microbridges: one that straddles a grain boundary and one that sits purely on a single-grain. The sharpness of the transitions clearly identifies the critical current density for both cases and the J_c reduction is attributed mainly to the presence of the grain boundary [Chaudhari 1988, Dimos 1988].

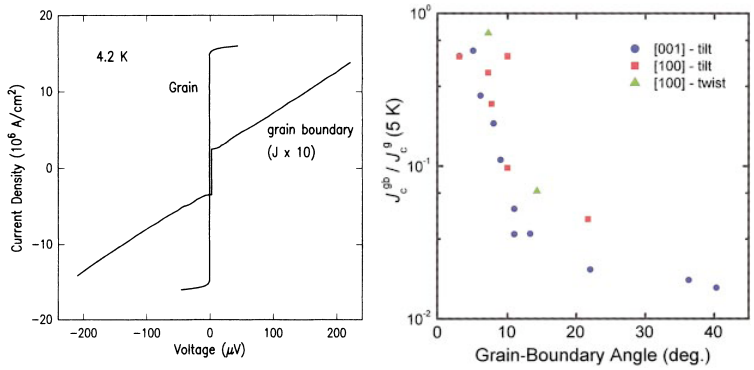

(a) (b)

Figure 1.18. (a) Current density versus voltage for intragrain and intergrain microbridge at 4.2K (b) Ratio of the intergrain and intragrain critical current densities of grain boundaries in bicrystal YBCO thin films as a function of misorientation angle [Dimos 1990].

Further distinction between small-angle and large-angle grain boundary misorientations can be made based on their effect on the macroscopic critical current density [Dimos 1990] as suggested by Dimos, *et al.* In this study, the J_c of the boundary [$J_c(gb)$] was measured and compared with the J_c of the neighboring grain interiors [$J_c(g)$] for several sets of YBCO samples epitaxially deposited onto bicrystal $SrTiO_3$ substrates with [001]-tilt, [100]-tilt, and [100]-twist boundaries of pre-determined angles of misorientations. As shown in Figure 1.18(b), the $J_c(gb)/J_c(g)$ ratio decreased rapidly with a θ^{-1} like dependence for θ values up to ~20^0. Beyond this value, an approximate θ-independent, uniformly low value of the J_c ratio was observed. The $J_c(gb)$ and voltage-current (V-I) behavior of the boundaries with θ >~5-10^0 were found to reflect the presence of weak electromagnetic coupling across the boundary.

The critical current of GBs also exhibits an interesting magnetic field behavior, which strongly depends on the misorientation angle. For low-angle grain boundaries, the critical current is almost insensitive to applied magnetic field. At angles of ~ 8^0 or more, Fraunhofer-like field dependence with small distortions is observed and these distortions become more pronounced as the angles are further increased. This behavior is attributed to the GB microstructure and the d-wave pairing symmetry of the high-T_c cuprates [Humphreys 1993, Copetti 1995, Hilgenkamp 1996, Mannhart 1996]. A relatively low and constant J_c (**H**) dependence for high angle grain boundaries at high fields was found by Verebelyi *et al.* and is shown in Figure 1.20. They also demonstrated that at high fields and angles smaller than 4.5^0, the grain boundary J_c, $J_c(gb)$, and the grain J_c, $J_c(g)$, become almost indistinguishable because in this regime, the critical current density is limited by the grains and not the grain boundaries [Verebelyi 2000].

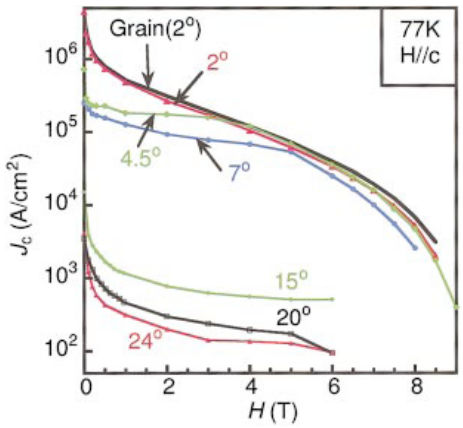

Figure 1.19. Magnetic field dependence of the critical current density of various [001]-tilt GBs in YBCO bicrystalline films. The magnetic field was applied in the boundary plane, along the c-axis of both grains [Verebelyi 2000].

From this, it can be deduced that the properties of high-angle GBs control the macroscopic J_c(**H**) characteristics of all polycrystalline high-T_c superconductors. This occurs because most high-angle GBs act like barriers to the current and have electromagnetic properties that are Josephson junction-like. The high-angle GBs in

the microstructure introduce a network of weak links (reduced $\boldsymbol{J_c}$ regions) into a superconducting path which includes a strongly magnetic field dependent $\boldsymbol{J_c}$ that can decrease by more than an order of magnitude even in weak fields. Such $\boldsymbol{J_c}(\mathbf{H})$ characteristics are clearly a serious problem for magnet applications and many also view it as the immediate obstacle to further development of wire-form materials for power applications. Ironically, the same GB behavior that plagues the high-field and high-current applications also forms the foundation of thin-film and superconducting integrated-circuit technologies that are based on the Josephson effect. A grain boundary-Josephson junction has a $\boldsymbol{J_c}$ that is extremely sensitive to weak magnetic fields which enables, rather than defeats, applications of high-Tc superconductors in electronics.

Thus from both the high-field, flux-pinning viewpoint and the low-field, Josephson junction-based electronics viewpoint, there is strong motivation to develop a detailed picture of the GB structure and microstructure and to describe their effects on the electromagnetic properties of the GBs. However, a complete understanding of this phenomenon is still unavailable due to the complex interplay of competing mechanisms such as: d-wave pairing symmetry, impurity scattering, oxygen stoichiometry, nanoscale phase separations due to order parameter suppression, and strain effects due to the chain of grain boundary dislocations [Hilgenkamp 2002].

1.5 Motivation of this work: Developing a versatile system to image dissipation at room temperature and detect low-level dissipation at low temperature

Despite the progress made towards optimizing and increasing the current carrying capability of HTS coated conductor tapes, it remains a challenge to achieve such high currents over long lengths of kilometers as required by many electrical applications due to the presence of randomly distributed current-obstructing defects such as large-angle grain boundaries, secondary phase inclusions, and mechanical defects. The majority of the available techniques allow visualization of current flow and dissipative areas with reasonable resolution and sensitivity. However, several critical issues regarding the operation of these techniques still remain. The first is the need to operate at low temperatures below the Tc of the superconductor. When the HTS is in its superconducting state, the temperature coefficient of resistivity is high and therefore facilitates a good sensitive measurement of the induced voltage. However, this is extremely inconvenient and presents logistical difficulties for long-length coated conductor tapes. The second issue pertains to the heating uniformity of a laser beam which is mostly surface heating. Laser radiation does not penetrate deep enough to ensure uniform heating throughout the thickness of the sample. It might not be an issue for thin films but it definitely becomes a factor for thick films, especially for HTS coated conductors that are usually composed of several layers of material and have several micrometers in thickness. Lastly, most of these techniques can only measure one physical property at a time. Even if images or scans of the spatial non-

uniformity in current distribution are acquired, no other information leading to the understanding of the relevant mechanisms involved is made available.

Also, during cryogenic device operations, sufficiently long and large thermal and/or electrical disturbances can cause instability and trigger a quench process [Bellis 1994, Tien 1989, Grabovickic 2003, Ishiyama 2007]. This situation is facilitated by the presence of the aforementioned defects, grain boundaries and secondary phases which may potentially nucleate "hot" spots of microscopic dimension which may turn into the normal state while the rest of the sample remains superconducting [Harrabi 2001]. Hot spots can evolve and result in instability and quench the superconducting devices. Understanding stability and quench properties of the coated conductors has been critical for large-scale device applications. Early detection of the hot spots is hence important but requires approaches of high sensitivity to the low-level dissipation and high spatial resolution of a microscopic hot spot.

This study, thus, intends to address these critical issues in mapping current-obstructing defects in conductors and HTS and detecting and characterizing low-level dissipation by developing a combined system consisting of a NSMM and a transport measurement set–up. This technique has several unique merits. First, the use of microwave radiation, which has a larger penetration depth in conducting films compared to laser light, provides a more uniform heating effect throughout the thickness of a sample. Second, this method takes advantage of the unique capability

of the NSMM to function as both field emitter and detector to measure more than one physical property at a time. As a microwave emitter, the NSMM can be used to locally heat areas on the surface of a current-biased sample and map the current flow and dissipation. As a detector, the NSMM can map the spatial non-uniformity in electromagnetic properties of the sample including loss, dielectric constant, surface morphology, etc. Obtaining multiple sets of complementary information on the same sample area allows correlation of different physical properties at the microscopic scale in both steady-state and dynamic modes. Third, the NSMM + transport system has the flexibility to perform measurements at room and cryogenic temperatures. The capability of room-temperature measurements makes the technique a good candidate for diagnostic studies on HTS coated conductors. Additionally, further investigations on the low-level dissipation in HTS in the superconducting state can be carried out at cryogenic temperatures. The unique advantage of non-contact and non-destructive characterization also presents an additional benefit for a quantitative assessment of the dissipation during the hot spot nucleation and evolution.

Chapter 2

Experimental Set–up

2.1 Near-field Scanning Microwave Microscope (NSMM)

2.1.1 Probe Design and Construction

The NSMM used in this work is based on a coaxial transmission line structure that constitutes an open-ended half-wavelength resonator. As such, it can be modeled as a lumped series LCR circuit with input impedance $Z_{in} = R + 4\pi j L(f - f_0)$ and quality factor $Q = \frac{2\pi f_0}{L}$ [Pozar 1990]. The maximum power transfer to the resonator is attained at resonance when the impedance of the signal source matches the real part of the input impedance (imaginary part becomes zero). If the reflected power of the probe is plotted against the frequency, the resonant frequency appears at the minimum of an inverted Lorentzian curve. The probe's unloaded quality factor is given by $Q_U = Q_L(1+\beta)$, where $Q_L = \frac{f_0}{HPBW}$ is the loaded quality factor and $\beta = \frac{1-|\Gamma|}{1+|\Gamma|}$ is the coupling coefficient. Both can be obtained experimentally with a

network analyzer. ***HPBW*** is the half-power bandwidth and Γ is the reflection coefficient at resonance [Steinhauer 1998]. The schematic, actual picture and equivalent circuit of the probe are shown in Figures 2.1(a), (b) and (c), respectively.

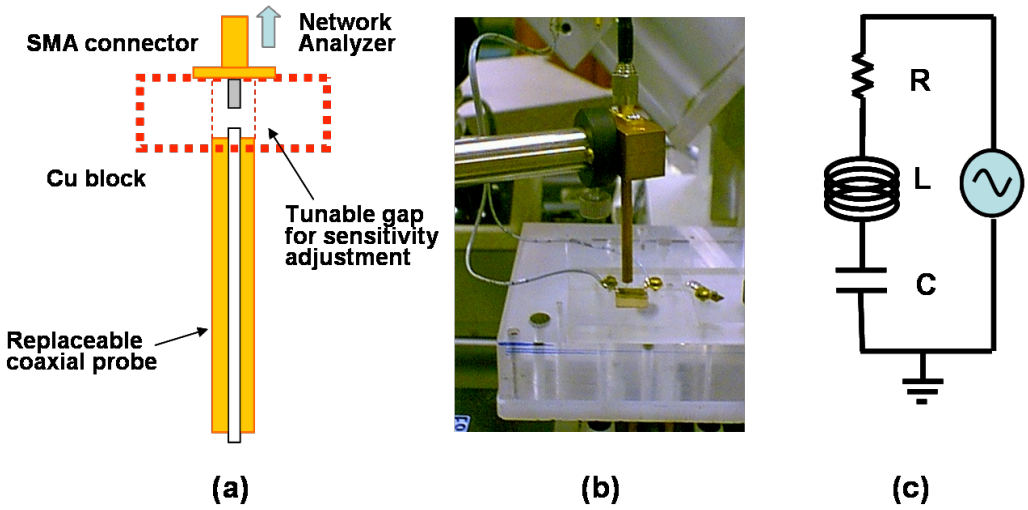

Fig.2.1 (a) Schematic, (b) photograph and (c) LCR circuit model of the home-built coaxial resonator-based microwave probe

This probe was constructed out of commercially available components which made the assembly and optimization procedures easy, straight-forward and inexpensive. The three major components of this probe are: (i) a semi-rigid coaxial cable, (ii) a Cu block and (iii) a subminiature assembly (SMA) connector. The copper block serves to secure both the SMA connector and the coaxial cable together. Since there is only one feed line that can connect the probe to external sources and electronics, only one-port measurements can be performed. The cable can be inserted into a hole that is drilled through the Cu block and is placed along the same axis as the center conductor of the SMA pin that is attached at the other end. The gap between the SMA pin and the

coaxial cable can be adjusted to tune the capacitive coupling of the resonator and achieve critical coupling which would then result in higher $\boldsymbol{Q}$ values and better sensitivity. Details of the assembly and characterization of this probe have been previously discussed [Aga 2003]. This probe design is classified as an open-ended coaxial resonator probe similar to the one developed by the group from Maryland [Steinhauer 1997, Anlage 1999]. The major difference lies in the size of the probe. The Maryland probe has a coaxial transmission line structure that is around 2-m long while our designed probe only has a total length less than 10 cm. The compact size of our probe was designed so that it may be used in ultra-high vacuum (UHV) chambers and low-temperature environments which will be discussed later in this thesis. Another critical area of difference is the tunability of the probe as provided by the small air gap in between the SMA connector and the semi-rigid coaxial cable. This feature allows for better impedance matching so as to achieve the critical coupling.

The length of the coaxial transmission line determines the operating frequency of the fundamental mode and its succeeding harmonics. For an operating frequency of 2 GHz, a resonator length of $\lambda/2$ (in this case, 75 mm) is required. For better imaging resolution, the center conductor of the coaxial probe is replaced with a small brass tube that accommodates a 200-μm diameter copper wire or a 250-μm diameter W wire, both of which can be tapered to form a fine tip at one end.

2.1.2 Metallic Tapered Tip Fabrication

Depending on the application and desired resolution and sensitivity, interchangeable metallic tips may be used for the NSMM. A list of all the metallic tips used in this thesis work and their respective properties is presented in Table I.

Table I. Summary of the metallic NSMM tips used in this experiment

Tip #	*Material*	*Tip Geometry*	*Tip Diameter (μm)*	*Tapering Length (mm)*
T1	stainless steel	blunt	900	NA
T2	Cu	blunt	200	NA
T3	Cu	tapered	20	1.4
T4	Cu	tapered	25	1.5
T5	Cu	tapered	5	1.7
T6	W	hybrid	0.8	0.2

Tip T1 uses the original metallic center conductor of the coaxial cable and has a blunt end of tip diameter ϕ_1 = 900 μm. When using smaller tapered tips, the center conductor of the coaxial probe was replaced with a small brass tube that has an inner diameter to fit a 200-μm diameter Cu wire or a 250-μm diameter W wire that can both be tapered at one end to a fine tip. Tip T2 represents an untapered Cu wire with a blunt end and ϕ_2 = 200 μm. It was made by carefully cutting the end with a diamond saw. In order to obtain higher spatial resolution, the area of the probe tip that interacts with the sample must be reduced. This can be done by effectively tapering the tip using various chemical or electrochemical etching techniques.

For our initial experiments, we used a simple and controlled chemical etching technique that can taper the tip diameter of a thin, 200-μm diameter Cu wire down to microns to tens of microns. Figure 2.2 shows the experimental set–up for this method.

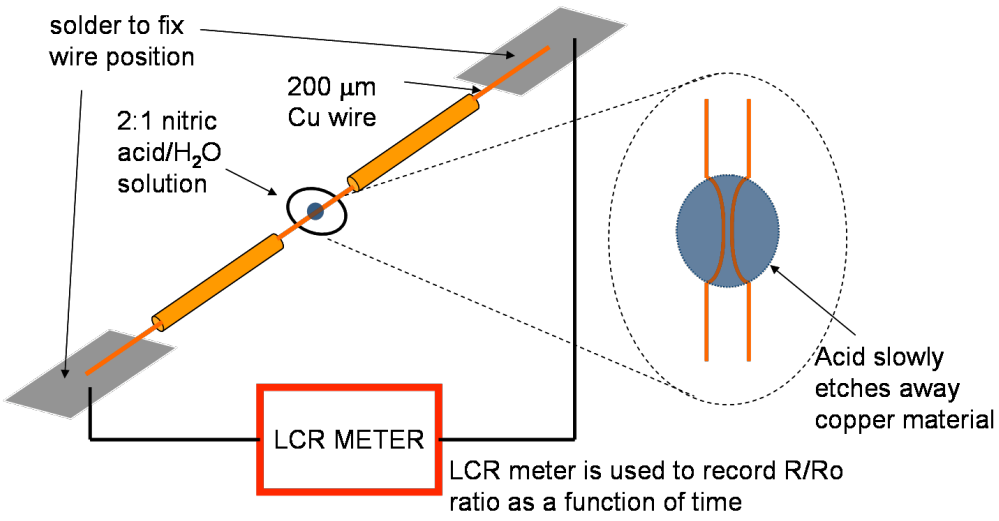

Fig.2.2 Experimental set-up for fabrication of the microprobe's tapered metallic tips.

The thin wire is secured by soldering its two ends to two separate pieces of a printed circuit board (PCB). Two small brass tubes are also used to help maintain the straight position of the wire during etching. The two solder points are then connected to the terminals of an LCR meter capable of obtaining precise measurements of the wire's resistance. A small amount of 2:1 nitric acid/H_2O solution is placed on a small glass slide and positioned in such a way as to bisect the thin copper wire. As the diluted acid solution etches away the copper material, the value of the R/R_0 (ratio of the wire's resistance during etch to its initial value) is observed to increase exponentially. Specific values of the wire's tip diameter can be obtained by monitoring the value of R/R_0 and stopping the etching process when R/R_0 reaches a certain value. When tips

with micron-size diameters are required, the etching process is allowed to continue until the breaking point is reached. This is usually characterized by a very sharp increase in the ratio R/R_0 because the resistance instantly goes to infinity. For tip diameters in the tens to hundreds of microns range, the process is cut short and does not completely separate the two tapered tips. A sharp razor is then used to cut the wire in the middle of the etched region. This process, thus, produces two tips with exactly the same tip diameter. Figure 2.3 shows representative results of the etching process. Tips T3, T4 and T5 were fabricated using this method.

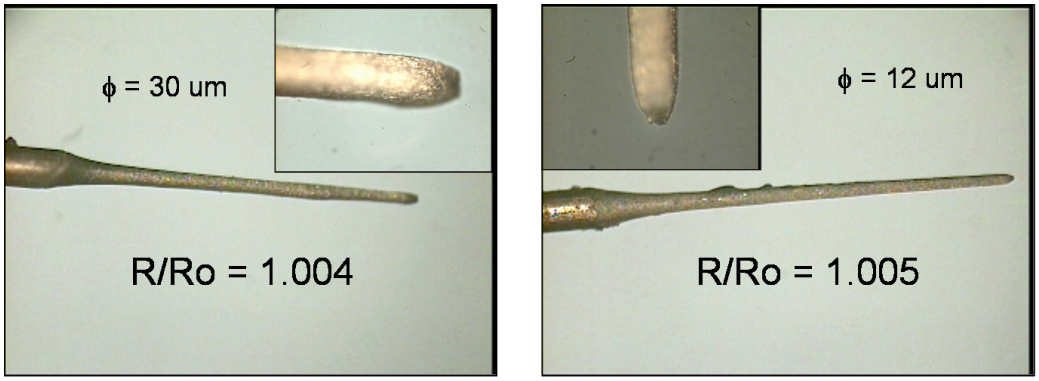

Fig.2.3 Microscope photographs of the fabricated Cu tips captured by a CCD camera. Tips with measured diameters of (a) 30 μm for R/R_0 = 1.004, (b) 12 μm for R/R_0 = 1.005. Inset: magnified images for each tip.

For our succeeding experiments, we have adopted a controlled electrochemical etching technique [Kim 2002] that can effectively taper a thin tungsten wire down to hundreds of nanometers while keeping the tapered part at a much reduced length. Most electrochemical etching techniques were developed for fabricating extremely sharp metallic tips with long tapering lengths for scanning tunneling microscopy

(STM) applications. For microwave microscopy, the use of extremely sharp tips is also favorable to obtain excellent spatial resolution but the sensitivity suffers because the interaction between tip and sample is restricted to only a very small volume. If the tip diameter approximates that of the STM tips while the tapering length is kept within a few hundred microns the interaction between the tip and the sample is expectedly enhanced primarily because a greater volume of the tip is allowed to interact with the sample surface and loss across the tapering length is minimized. With proper control of the parameters for this technique, a tip can be fabricated to only have a small portion of the end tapered so that it almost appears to be blunt at the end. The effect of this "hybrid" probe tip, one that combines the characteristics of a sharp and blunt tip, is an enhanced spatial resolution combined with higher sensitivity [Kim 2003]. A schematic diagram of the set-up is provided in Figure 2.4.

A 15 V bias voltage supplied between the tip and a stainless steel cylindrical electrode, both submerged in the electrolyte, for a 15 minute period has resulted in tip T6 with a tapering length of 200 μm and a tip diameter of 800 nm.

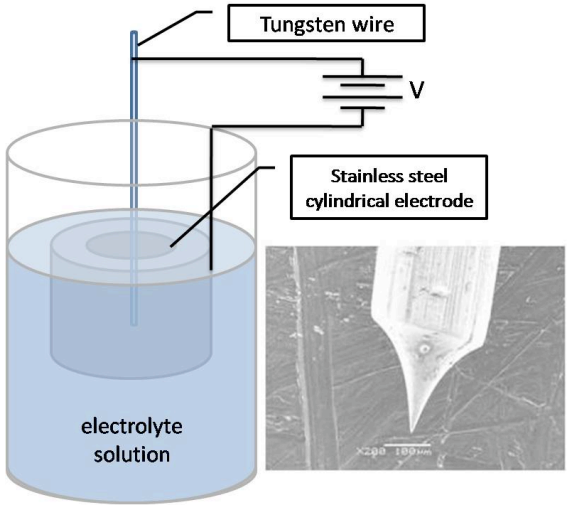

Fig. 2.4 Schematic diagram of the electro-chemical etching set-up for tungsten tips with a SEM image of the resulting W tip.

2.1.3 Characterization

When a sample is placed close to the probe tip, the interaction between sample and tip can be modeled as an additional capacitance C_s to the lumped LCR circuit as shown in Fig. 2.5(a). As the distance between sample and tip is decreased, the corresponding increase in C_s is equivalent to increasing the length of the transmission line [Vlahacos 1996] and thus causes a decrease in the resonant frequency. Since $f_0 = \frac{1}{2\pi\sqrt{LC}}$ and C can be obtained from parallel plate approximations, then $f_0 \sim \sqrt{d}$ where d is the tip-to-sample separation. This relation has been experimentally verified using two types of materials, glass and silver, with different dielectric constants. The sample is a standard glass slide with a thin layer of silver film sputtered on half its area. The sample was positioned at a height of about 200 μm below the tip and gradually brought close to the tip in 10-μm increments using a motorized z-stage.

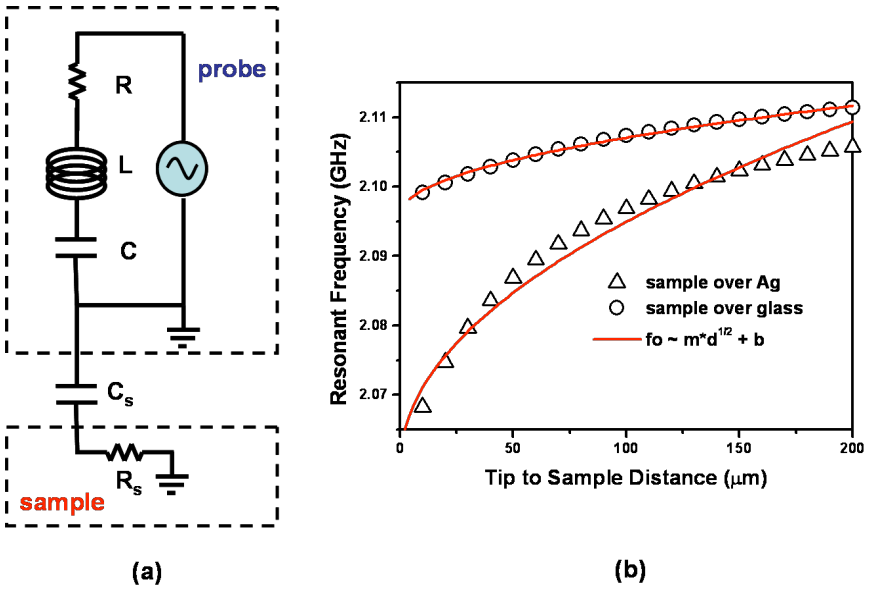

Fig.2.5. (a) Equivalent circuit for probe and sample interaction. (b) Tip-sample separation dependence of the resonant frequency for glass and thin layer of silver.

The resonant frequency was observed and recorded as a function of tip-sample distance and the results are shown in Fig. 2.5(b). Both types of material agree well with the parallel-plate approximation. However, compared to glass, the rate of change in resonant frequency for silver is greater because the capacitive coupling between the metallic center conductor and the silver film is stronger than it is with glass.

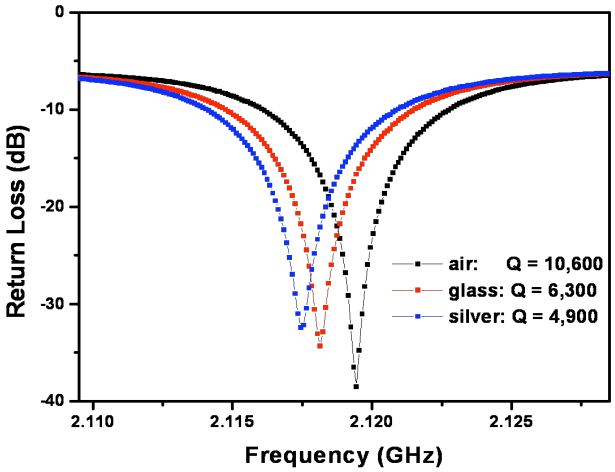

Fig. 2.6 Changes in the probe's reflection property as different materials are placed under the probe tip. Measurement was performed at room temperature.

Using the same sample, the frequency dependence of the reflection coefficient was also measured. Fig. 2.6 shows the inverted Lorentzian curves representing the frequency dependence of the reflected microwave power. A systematic decrease in the probe's resonant frequency is observed as samples of different material are placed underneath the tip. Another noticeable change is in the broadness of the resonance curves. The broadening of the curves signifies a decrease in the resonator's quality factor due to the additional dissipation introduced by the sample.

2.2 Microwave Measurements

For resonant NSMMs, microwave measurements can be performed in either the frequency-sweep mode or the constant-wave mode. In the frequency-sweep mode, a sweep over a frequency range containing the probe's resonant frequency is obtained from the NSMM. With this set-up, shifts in the resonant frequency f_0, changes in the resonator's quality factor **Q** and the signal's reflection coefficient $\mathbf{S_{11}}$ can be measured by a HP8722C vector network analyzer as the probe is scanned across a film's surface. In the constant-wave mode, a low power, constant-wave (CW) mode microwave signal with frequency fixed at or near the resonant frequency is fed by the same network analyzer as input to the NSMM. With this set-up, changes in the reflected power can be measured using a Boonton™ power sensor and meter. Figure 2.7 provides a schematic for both types of measurements where the blue arrow corresponds to frequency-sweep measurements and the red arrow corresponds to the CW-mode measurements. A clear advantage of the frequency–sweep measurement is its ability to provide more information in one scan. Shifts in the resonant frequency f_0 are strongly dependent on the capacitive coupling between

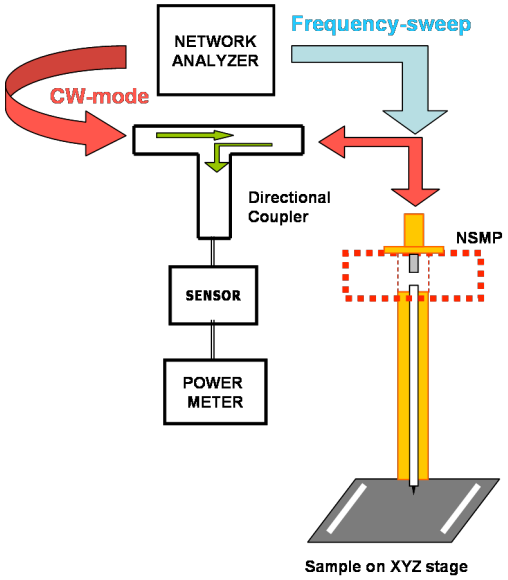

Fig. 2.7 Microwave measurements in CW-mode (red arrows) and frequency-sweep (blue arrow) mode.

the probe and the sample and is, therefore, more sensitive to tip-sample distance than sample properties. Both the quality factor **Q** and reflection coefficient $\mathbf{S_{11}}$, on the other hand, are related to the sample's microwave absorption. For the CW-mode measurement, the measured reflected power does not correlate directly to the sample's microwave absorption. Slight changes in the resonant frequency due to tip-to-sample distance variation will alter the reflected power significantly. Thus, the information containing the sample's microwave absorption becomes entangled with tip-sample distance variation. One way to untangle these two is to provide a tip-to-sample distance feedback mechanism that can maintain a constant height for the probe as has been discussed in the previous chapter. In the current set-up, however, the sensitivity of the frequency-sweep measurement is considerably affected by the sweep range used for the network analyzer. The power sensor and meter, on the other hand, has greater sensitivity as it can detect small changes in the reflected power. Another relevant issue is the speed of the scan. CW-mode measurements tend to have a faster response compared to frequency-sweep measurements because the latter is limited by the sweep time of the microwave network analyzer.

To compare the resolution obtained from frequency-sweep and CW-mode measurements, a map of the morphology variations in a standard TEM grid is obtained using both measurement set-ups. A probe equipped with tip T5 is scanned over an 80 μm x 80 μm area of a TEM grid with a 1 μm step size. The probe tip is fixed at an approximate 1-3 μm distance above the sample. A LABVIEW program

coordinates the movement of the sample stage with respect to the probe and also acquires the data from the network analyzer or the power meter. This data is presented as a two-dimensional array where each element represents the value of the measured property at a specific x-y position. The data are also saved as a binary file that can be opened and converted into a two-dimensional color image by **WSxM version 3.0**. This software, developed and distributed for free by Nanotech Electronica S.L., is specifically designed to create SPM-generated images.

Figure 2.8 shows a two-dimensional color map and a line scan profile along the dark line of the TEM grid acquired through both types of measurements. In terms of morphology variations, the CW-mode measurement clearly provides a much sharper image compared to the frequency-sweep measurement. This is further supported by the line scan profile where features in the TEM structure are identified better by the sharp transitions. According to the profile, a 10% – 90% transition corresponds to a resolution of 2 ~ 3 μm. However, the resolution is theoretically limited by either the tip-to-sample distance or the probe tip diameter, whichever is larger. In this case, the tip diameter equal to 5 μm eventually sets the limit on the spatial resolution of the experimental set – up. The difference in resolution and image sharpness between the two images and scans is attributed mainly to the sensitivity of the measurement electronics.

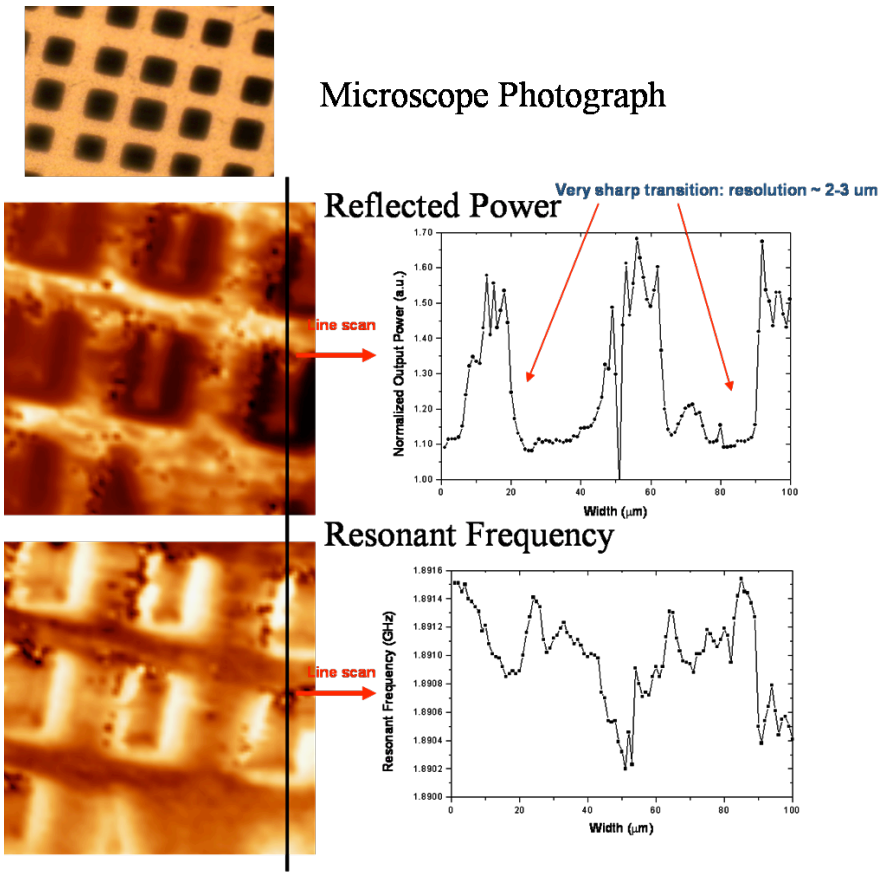

Fig.2.8 Photograph and two-dimensional images of a TEM grid using CW-mode (reflected power) and frequency-sweep (resonant frequency) measurements. A profile along the dark line shows the line scan and the transition when the probe comes across a 15 μm feature on the grid. Sharp transitions are clearly observable in the reflected power and show a resolution of 2-3 μm.

2.3 Room-temperature Scanning Stage

In order to perform scans of a sample's surface morphology and electrical properties at room temperature, either the probe or the sample needs to move relative to the other. In this regard, an x-y-z stage was assembled using three Newport motorized linear stages. The x- and y- stages are identical Newport Model MFA-CC horizontal

linear stages with a maximum translational distance of 25 mm (±12.5 mm relative to center) while the z-stage is a Newport Model UZM vertical linear stage that can move a maximum 4 mm in one direction (± 2 mm from "home" position). Both types have a minimum stepping distance of 100 nm. A Newport motion controller/driver (model ESP3000) allows user control of the individual stages and also facilitates remote control via computer through its general-purpose interface bus (GPIB). A LABVIEW^{TM} subroutine was developed to control the speed, direction and motion of each stage during scanning and to synchronize movement with data acquisition. The three stages are stacked securely on top of each other and the whole assembly is set on an optical table to isolate it from vibrations caused by other machinery inside the room. Since the optical table does not have a self-leveling capability, a separate platform with fine-leveling adjustment mechanism is placed in between the table and the 3-stage assembly. A photograph of the scanning stage is provided in Figure 2.9.

The NSMM is situated above the sample stage and attached to an arm that can be adjusted and rotated freely for optimum positioning. This lever arm sits on a mechanical jack that allows for the coarse vertical approach of the probe towards the sample.

Fig.2.9 The room-temperature scanning stage set-up with the NSMM

2.4 Integration of I-V Measurement

In order to map the non-uniformity in the dissipation of a conducting sample at room temperature, a method capable of measuring small changes in the sample's resistance is required. The Wheatstone bridge network shown in Figure 2.10 allows measurement of induced voltage due to microwave irradiation as small as 1 μV. The value of the resistance R_X is chosen in such a way that it will balance out the voltage across the sample and the voltage across R_X. Since R_X is a standard ceramic resistor with fixed values, a potentiometer is attached to the other resistance R_1 for fine adjustment of the resistance ratios. The constant bias current is provided by an alternating current source (f = 500 Hz) to prevent excessive Joule heating on the sample. Once a pulse of microwave signal is radiated on the surface of the sample, the change in resistance can be detected as an induced voltage by a lock-in amplifier.

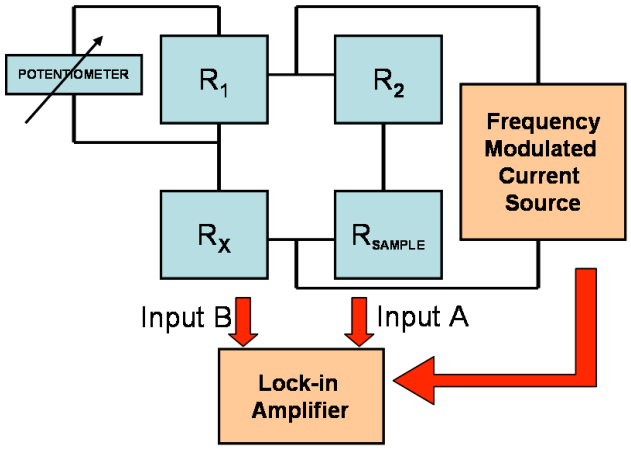

Fig.2.10 Wheatstone bridge network for I-V measurements.

For this type of measurement, the sample is mounted on a Plexiglass-based sample holder with spring-loaded pins that can secure the sample and serve as the terminals

for connection to the Wheatstone bridge network. The sample holder is about the size of a standard microscope slide and can be screwed on top of the x-y-z stage. This makes it convenient for the sample to be mounted elsewhere and easy to store once the measurement is done. Furthermore, Plexiglass was the material of choice because it is relatively lightweight and does not contribute additional heating during microwave irradiation.

To send a pulsed CW-mode microwave signal centered on the NSMM's resonant frequency, an Agilent 8762B coaxial switch is inserted between the source and the resonator input. And since the network analyzer has limited power capability, an Amplifier Research microwave signal amplifier is also used to extend the maximum input power from 0 dBm to 37 dBm (around 3.7 W). The pulsing of the microwave signal is achieved by turning the power supply of the coaxial switch ON and OFF as controlled by the computer's parallel port. The fastest switching speed achievable using this set-up is 0.7 seconds.

2.5 Low Temperature NSMM Chamber

A low-temperature vacuum chamber was constructed and assembled in-house to provide an environment to study properties of superconductors using the NSMM. Fig. 2.11 shows a schematic of the low-temperature chamber and a number of photographs of some of its parts.

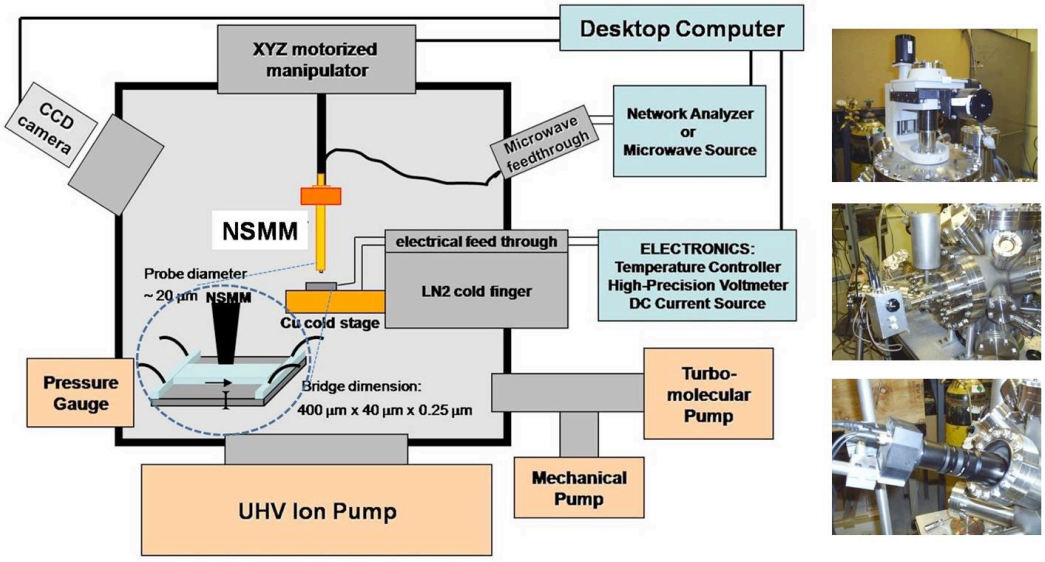

Figure 2.11 Schematic diagram of the low-temperature chamber and photographs of (from top) the Huntington xyz motorized stage, electrical feed through and CCD camera.

The vacuum chamber was equipped with a mechanical and turbo-molecular pump to bring the vacuum to about 1 x 10^{-6} Torr. This chamber is mounted on a pressure-controlled optical table that can suppress random vibrations from the building and acoustic noise. To maintain high vacuum during measurement while providing a vibration free environment for NSMM measurements, an ultra high vacuum ion pump (Varian) was additionally connected to the chamber and operates only after the first two pumps are deactivated. The sample stage was attached to an oxygen-free Cu cold finger immersed in a liquid nitrogen tank capable of providing stable cryogenic temperatures to the sample for approximately 2-3 hours. The sample temperature was measured using a Platinum resistor embedded in the sample stage and sample heating was provided by a home-made manganin wire heater attached to the sample stage.

Temperature monitoring and control was provided by a Lakeshore model 330 temperature controller. The probe can be precisely positioned by controlling an attached Huntington XYZ motorized stage with step sizes as small as 100 nm in the x and y direction and 200 nm in the z direction. Several viewports were made available in the chamber for visual inspection of the coarse probe approach and positioning while a CCD camera with zoom lens aids in fine positioning. Electrical attachments to the microbridge constituting a four-point probe configuration can be provided by thin gold wires connected to the silver contact pads by indium dots. These wires were then twisted together to reduce noise in the electrical measurements. DC current was supplied by a Keithley 220 current source which can provide a maximum 100 mA current and voltage measurements were carried out using a Keithley 224 nanovoltmeter. One of the ports on the chamber contains a feed through for the microwave signal so that either frequency-sweep or CW-mode microwave measurements can be carried out through the NSMM.

Chapter 3

Imaging Non-uniformity and Defects in Thin Conducting Films: Experiment and Simulation

The proposed technique was first demonstrated on thin conducting films to determine the viability of using the NSMM for imaging dissipation and non-uniformity. Qualitatively, macroscopic and microscopic defects were clearly identified and imaged in the experiments using this technique. In order to have a better understanding of the mechanism of how microwave heating affects the local properties of the sample, a theoretical model was also developed and the simulation results [Mishra 2005] were compared with the experimental one. This is an important step towards developing a quantitative method for obtaining the electrical current distribution in conducting and superconducting samples.

3.1 Imaging Ag Thin Film

The combination of the NSMM and I-V measurement set-ups enables measurement of multiple physical properties simultaneously at microscopic scale. In sensor mode, the NSMM can be used to perform frequency-sweep and CW-mode microwave

measurements that can detect local loss, dielectric constant, surface morphology, etc. through measurement of the probe's resonant frequency f_0, quality factor Q, reflection coefficient S_{11} and reflected power due to interaction of the tip with the sample. In emitter mode, the NSMM can be used to send pulsed, CW-mode microwave signals centered on the probe's resonant frequency to heat a local spot on the surface of a current-biased sample. By focusing the microwaves emitted at the tip of the NSMM, the hot spot dimension can be varied from hundreds of millimeters to sub-micrometers. When heated, the resistance of the hot spot changes, resulting in a voltage ΔV. Mapping the non-uniformity of the ΔV can then reveal the current-obstructing defects. Figure 3.1 shows a schematic of the interaction between probe and sample. The microwave radiation causes the charge carriers to be accelerated and their collisions with the lattice results in heat across a local spot. The increase in temperature in this "hot spot" results to an increase in local resistance and thus can be measured as an induced voltage in the experimental set-up as discussed in Section 2.4.

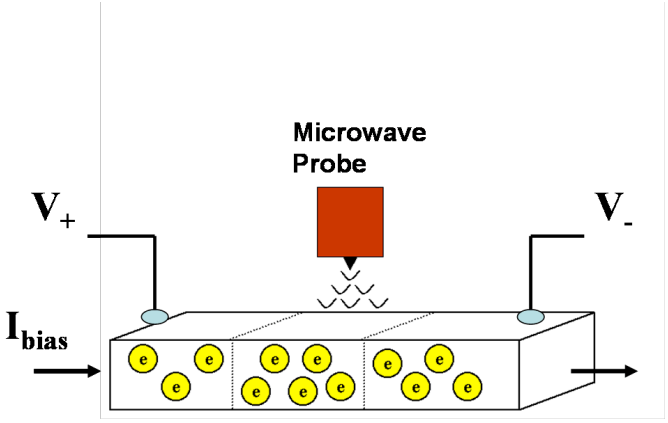

Figure 3.1 Schematic illustration of microwave radiation from NSMM interacting with charge carriers.

Figure 3.2 shows the time evolution of the induced voltage ΔV on a silver thin film with thickness t = 100 nm and width w = 500 μm which was experimentally investigated by applying two separate microwave pulses with different input powers and pulse widths (P_1 = 1 W at δt = 10 sec and P_2 = 3 W at δt = 0.7 sec) on a single spot on the film. The sample has an input bias current I_b = 5 mA and the probe has an approximate tip diameter ϕ = 900 μm (tip T1) which will cover the whole width of the silver film.

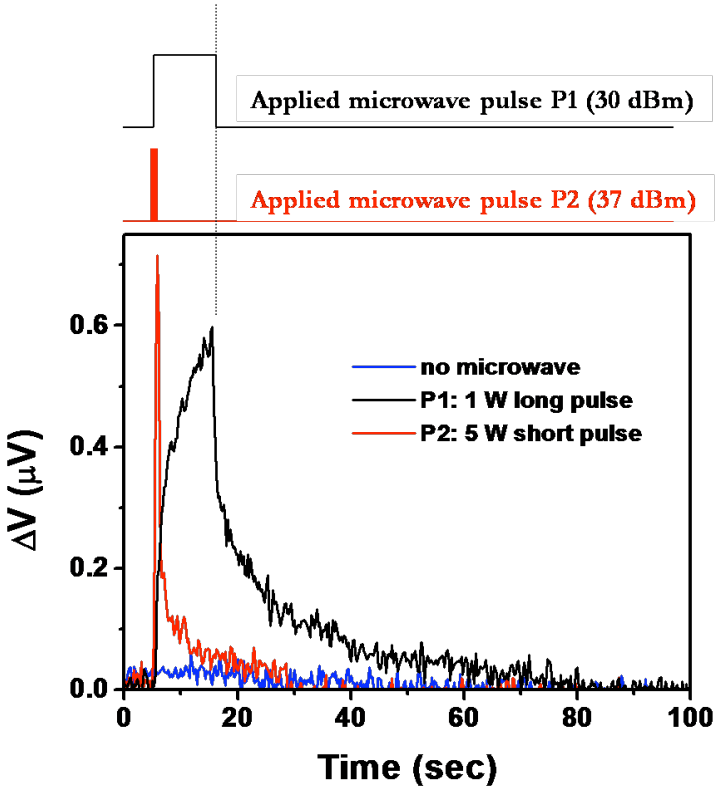

Fig.3.2 Voltage response (ΔV) of a current-biased silver microbridge to two different microwave pulses [Aga 2005]

Both cases show a fast increase in ΔV in the initial ~ 500 ms but the response to pulse P_1 shows a slow climb to the maximum value following this initial fast increase. The

induced voltage ΔV then relaxes to its original value at the end of the microwave pulse. Even though the peak value for pulse P_2 is higher than that for P_1, the relaxation time for P_2 is shorter than for P_1. This can be attributed to the fact that P_1 has a longer duty cycle during which more energy was transferred to the charge carriers, causing a wider spread of heat around the hot spot, as a consequence of heat diffusion, degrading the spatial resolution. In the succeeding measurements and scans, ΔV now refers to the difference between the peak voltage at the end of the pulse and the voltage just before the pulse was sent. Furthermore, a pulse of shorter width of 0.7 sec was always used to minimize heat diffusion.

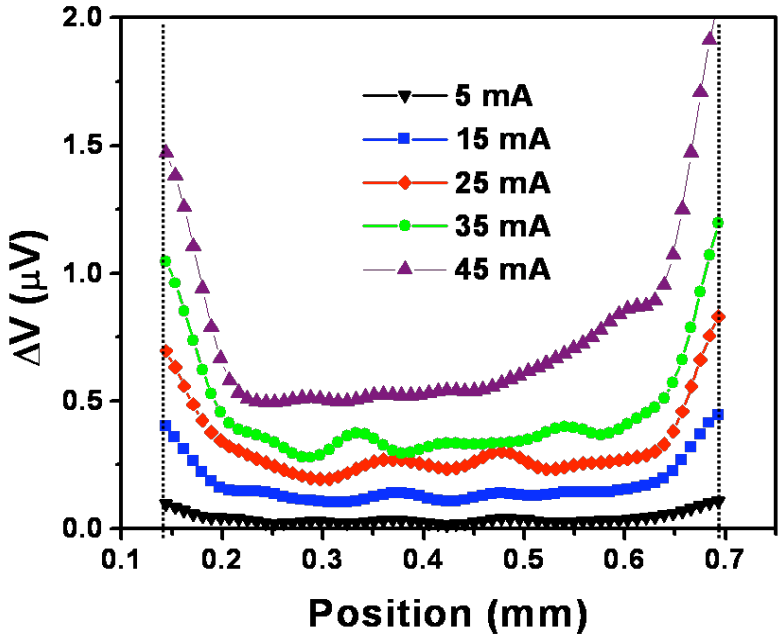

Fig.3.3 Experimental line scan profiles of ΔV across the width of a silver microbridge at various I_b values [Aga 2005].

Sending pulsed microwave radiation on successive points along a line or over an area of a current-biased sample will provide a line profile or a two-dimensional image of the induced voltage and show the non-uniformity in current distribution. Using probe tip T3, the ΔV line profile across the width of a 500-μm wide, 100-nm thick silver microbridge is investigated. Figure 3.3 shows line scans of ΔV across the width of the silver microbridge at different values of the bias current ranging from 5 mA to 45 mA. The step size is 10 μm and the dashed lines indicate the edges of the film. It is observed that the induced voltage increases sharply at the edges and is relatively flat at the center of the film. For a film free of any type of defects, it is assumed that the resistivity is uniform across the width. However, the line scans suggest that the change in resistivity at the edge due to microwave absorption is more than that at the center. This result raises a compelling question regarding the relevant mechanisms responsible for this phenomenon and invites further experiments and thoughts.

Since the step size is smaller than the NSMM tip diameter, there is also a chance for heat to accumulate as the NSMM scans through the line. This is the reason why the the magnitude of the peak at the right edge is slightly higher than the peak at the left edge, considering the probe moves from left to right. Also noticeable is the deviation of the curve corresponding to an I_b of 45 mA from the other curves. It is speculated that at this bias current level, the ΔV response is already affected by sample heating due to bias current. If normalized with respect to the bias current, all curves should coincide with each other except for the last curve.

To test the spatial resolution of this ΔV scanning imaging technique, small voids were milled off of a 200-μm wide, 100-nm thick silver film on glass substrate using a TEM grid as mask (see Fig.3.4(a)). The voids have dimensions of 20 x 20 μm^2 separated by 15 μm wide lines and will serve as obstacles to the flow of current when the silver bridge is biased. Figure 3.4(b) shows the 3-dimensional rendering of the resonant frequency image of an enclosed region measuring 150x150 μm^2. The voids are clearly resolved and this scan is consistent with the image provided by the optical microscope. Figures 3.4(c) and Fig 3.4(d) depict a 2-dimensional scan of both the resonant frequency and the induced voltage on a smaller scan area of 100x40 μm^2. Both images provide a clear identification of the microscopic defects on the silver film.

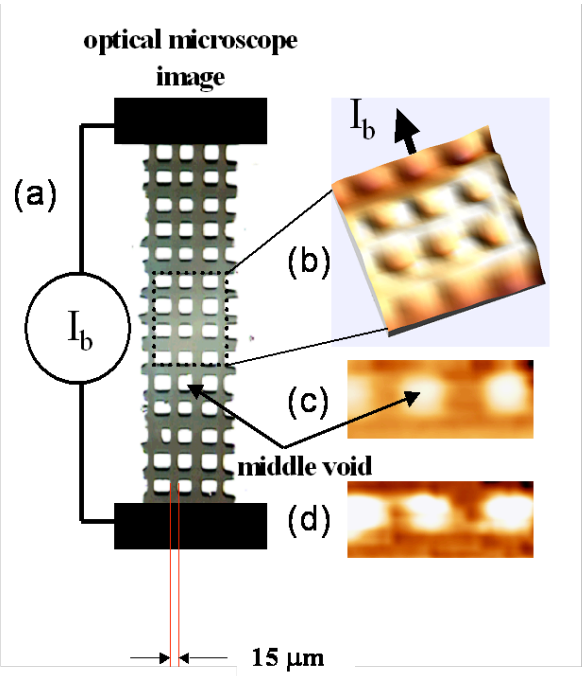

Fig. 3.4 (a) Optical microscope image of a biased silver microbridge with an array of voids. (b) 3D f_0 image of enclosed region. 2D images of (c) f_0 and (d) ΔV on a smaller area [Aga 2005].

Though the voids can be clearly identified and the current distribution can be qualitatively described using these scans, the eventual aim is to provide a technique that can map the distribution of current quantitatively. Achieving such a goal would be of great help in determining how much the current density is affected by specific types of defects and finally provide a criterion for quality control of HTS coated conductors. However, accomplishing such an objective would require a better understanding of the mechanisms governing the microwave-induced voltage response of the sample. In this light, a theoretical model was developed, simulated and compared to the experimental results [Mishra 2005] to describe how microwave radiation is absorbed in thin films and how heat energy is diffused across the sample.

3.2 Simulating Microwave Absorption in Conducting Films

3.2.1 Heat Diffusion Model

Upon absorption of the microwave energy in the thin film, the change in local temperature through time can be evaluated by solving the time-dependent heat flow equation. This thermal energy would then propagate to adjacent regions near the hot spot. Since heat could also flow out of the film through convection and radiation into the surrounding environment, these factors should be considered when formulating the mathematical equation that describes the heat flow.

Given an infinitesimal volume of material (as shown in Fig 3.5), the amount of heat accumulated is equal to the difference between the amount of heat that enters plane A and the amount of heat that leaves plane B. The rate of heat accumulation across this volume element gives the two-dimensional equation of heat diffusion: $\rho C_p \frac{\partial T}{\partial t} dxdy \bullet z_l = K\left[\frac{\partial^2 T}{\partial x^2} + \frac{\partial^2 T}{\partial y^2}\right] dxdy \bullet z_l$ where T is temperature and z_l, ρ, C_p and K are the thickness, density, specific heat and thermal conductivity of the material respectively. Subtracting heat losses due to convection and radiation to the surrounding environment, the heat diffusion equation can be modified as:

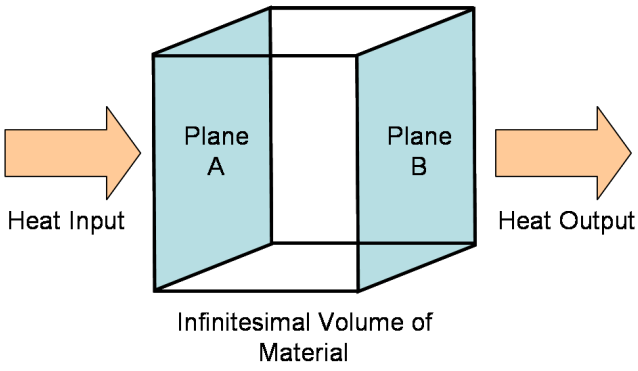

Fig. 3.5 Heat accumulation in an infinitesimal volume element

$$\rho C_p \frac{\partial T}{\partial t} = K\left[\frac{\partial^2 T}{\partial x^2} + \frac{\partial^2 T}{\partial y^2}\right] - \frac{h}{z_l}\left(T - T_{air}\right) - \frac{\varepsilon \sigma_s}{z_l}\left(T^4 - T_{air}^4\right)$$

where h is the heat transfer coefficient of air, ε is the surface emissivity and σ_s is the Stefan-Boltzmann constant. The possibility of heat loss through the substrate was mentioned but since the thermal conductivity of the substrate used (glass) is two orders of magnitude less compared to the thermal conductivity of silver, the cross diffusion of heat from film to substrate was deemed negligible [Mishra 2005].

For the simulation, a thin layer of silver film (~ 100 nm) on glass substrate is considered. A fixed bias current flows from one end of the film to the other end and a focused microwave radiation is applied on one spot given by an x and y coordinate on the two dimensional surface. A schematic of the model is given in Fig. 3.6. The right hand side of the heat diffusion equation is discretized over the grid points on this surface.

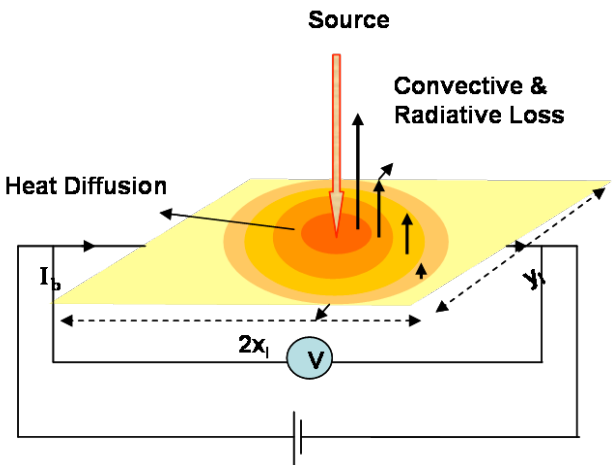

Fig.3.6 Schematic model of heat diffusion on a thin film upon application of microwave radiation.

The energy of the microwave radiation incident on the film can be reflected, transmitted or absorbed depending on the sample's properties. Since the wavelength of a 2 GHz microwave radiation is much larger than the penetration depth (~ 1.4 μm) and thickness (~ 0.1 μm) of the silver film, the fraction of microwave power absorbed in the film can be obtained using the thin film approximation as suggested by Bosman, Lau and Gilgenbach [Bosman 2003]: $A = \frac{2\xi}{(1+\xi^2)}$ where $\xi = \frac{z_l}{s}$ and $s = \frac{2\pi\delta^2}{\lambda}$. Here, δ is the penetration depth and λ is the radiation wavelength. From this equation, a maximum 50% absorption of the energy is possible when the thickness equals the value of s. To account for the power delivered by the microwave

radiation on a specific point in the sample surface, a term is added into the heat diffusion equation for one of the grid points:

$$\rho C_p \frac{\partial T}{\partial t} = K\left[\frac{\partial^2 T}{\partial x^2} + \frac{\partial^2 T}{\partial y^2}\right] - \frac{h}{z_l}\left(T - T_{air}\right) - \frac{\varepsilon\sigma_s}{z_l}\left(T^4 - T_{air}^4\right) + \frac{A \bullet P_{in}}{2z_l \Delta x \Delta y}$$

where $\boldsymbol{\Delta x}$ and $\boldsymbol{\Delta y}$ represents the size of the grid points. The central finite difference formulation allows each point to be represented by a coupled ordinary differential equation (ODE). After setting the initial condition and boundary conditions, the heat diffusion equation was solved using a FORTRAN-coded program.

3.2.2 Temperature Profile

Using a grid size of 200 μm (approx. equals the tip diameter), a microwave pulse of 0.7 sec and an incident power of 1 W, a temperature profile is obtained from simulation for a 2 mm x 2 mm square silver sample. Figure 3.7 shows an rendering of the temperature profile when the microwave is applied at the edge and at the center of the film.

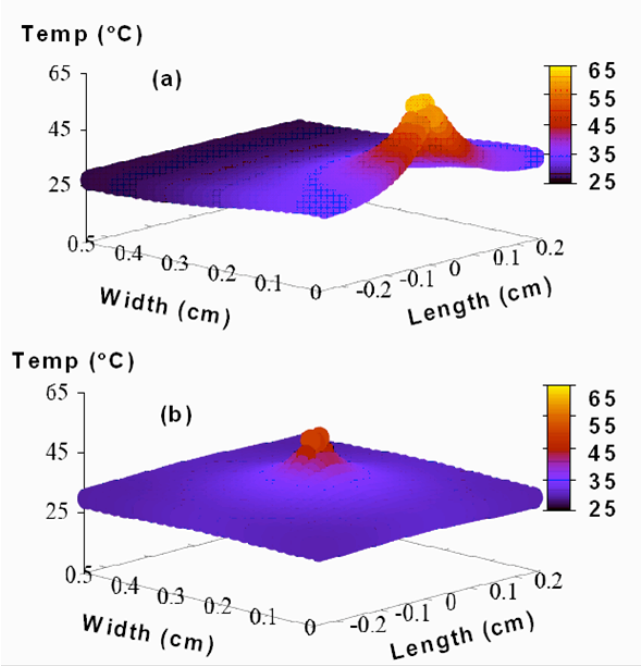

Fig.3.7 Temperature profile when microwave is incident (a) at the edge and (b) at the center of the film.

Results showed an increase of ~40 ^{0}C in temperature when microwaves are radiated on the edge of the film compared to a ~25 ^{0}C increase when microwaves are incident at the center of the film. The difference was attributed to the uniformity of heat diffusion [Mishra 2005]. When microwaves are incident at the center, heat diffuses uniformly via conduction through neighboring atoms. Whereas, when microwaves are incident towards the edge of the film, heat only diffuses to one side of the plane while the other half encounters a boundary. Heat may be lost due to convection to air but it is substantially less compared to heat lost by conduction which then leads to slower heat diffusion and higher temperature increase.

3.2.3 Solution of Continuity in Current Flux

Given a temperature profile obtained by solving the heat diffusion equation though the entire film surface, the resistivity at each point can be calculated by:

$$r = r_0 + \alpha(T - T_{air})$$

where $\boldsymbol{r_0}$ is the material's resistivity and $\boldsymbol{\alpha}$ is the temperature coefficient of resistivity. This relation allows for the calculation of the induced voltage due to microwave absorption ($\boldsymbol{\Delta V}$) at a constant bias current density because it is related to the change in resistivity ($\boldsymbol{\Delta r}$) on the specific spot by:

$$\Delta V = J_b \Delta r \bullet l$$

The voltage distribution in the film is obtained by solving the continuity equation of the current flux [Mishra 2005]: $\nabla \bullet J = 0$ where $J = \frac{\Delta}{\Delta x}\left(\frac{V(x,y)}{r(x,y)}\right)\hat{x} + \frac{\Delta}{\Delta y}\left(\frac{V(x,y)}{r(x,y)}\right)\hat{y}$.

Boundary conditions were set for the edges of the film and the bias current was set to flow into and out of the film in the x direction. Using the same grid points in the heat diffusion equation, the Gauss-Seidel iterative technique was used to solve the voltage distribution. To obtain the voltage induced due to the microwaves, the voltage drop before the microwaves were switched ON is subtracted from the total voltage rise.

This whole calculation is carried out with microwaves applied to only one grid point. Simulating the scanning procedure in one or two dimensions entails performing a sequence of calculations where the source term in the heat diffusion equation is added when microwaves are applied at every grid point one at a time.

3.3 Comparison of Simulation and Experimental Results

Using the model just described, simulations were performed to study the time evolution, bias current dependence, input power dependence and thickness dependence of the induced voltage and then compared to the experimental results. In addition, the line scan profile of ΔV was also simulated and compared.

3.3.1 Induced Voltage Due to Microwave Irradiation

For the simulation, a silver film of dimension similar to the one used for Fig. 3.2 was biased with I_b = 5 mA and radiated with a microwave pulse of power 1 W and width 0.7 sec. A tip diameter of 200 μm corresponding to the grid size was used for the simulation. The time evolution of the simulated voltage response is shown in Fig.3.8.

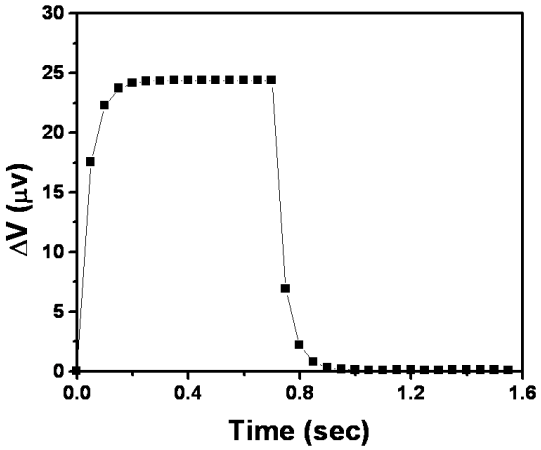

Fig.3.8 Simulated voltage response of current-biased silver film to microwave radiation [Mishra 2005]

The appearance of the curve for the simulation qualitatively resembles that of the one obtained from experiment. The discrepancy in the time constants for both rise and fall between experiment and simulation is mainly attributed to substrate heating [Mishra 2005] which was not considered in the simulation. Once the microwave pulse is switched on, the heat diffuses immediately in the film but the heat absorbed by the substrate lingers longer because of its lower thermal conductivity. As the temperature of the film returns to normal, the heat from the substrate may transfer back to the film via the substrate-film interface. This would then cause the voltage response to take longer time before it can go back to its original value.

3.3.2 Bias Current and Microwave Power Dependence

Figure 3.9(a) and (b) shows the qualitative agreement between the experimental and simulated dependence of the voltage response on the input microwave power to the NSMM at different values of the input bias current. The linear dependence of the induced voltage on P_{in} suggests that the increase in local temperature is linearly dependent on the input microwave energy. Furthermore, as the bias current is increased, a proportional increase in the induced voltage is also observed as expected from Ohm's Law $\Delta V = I_b \Delta R$.

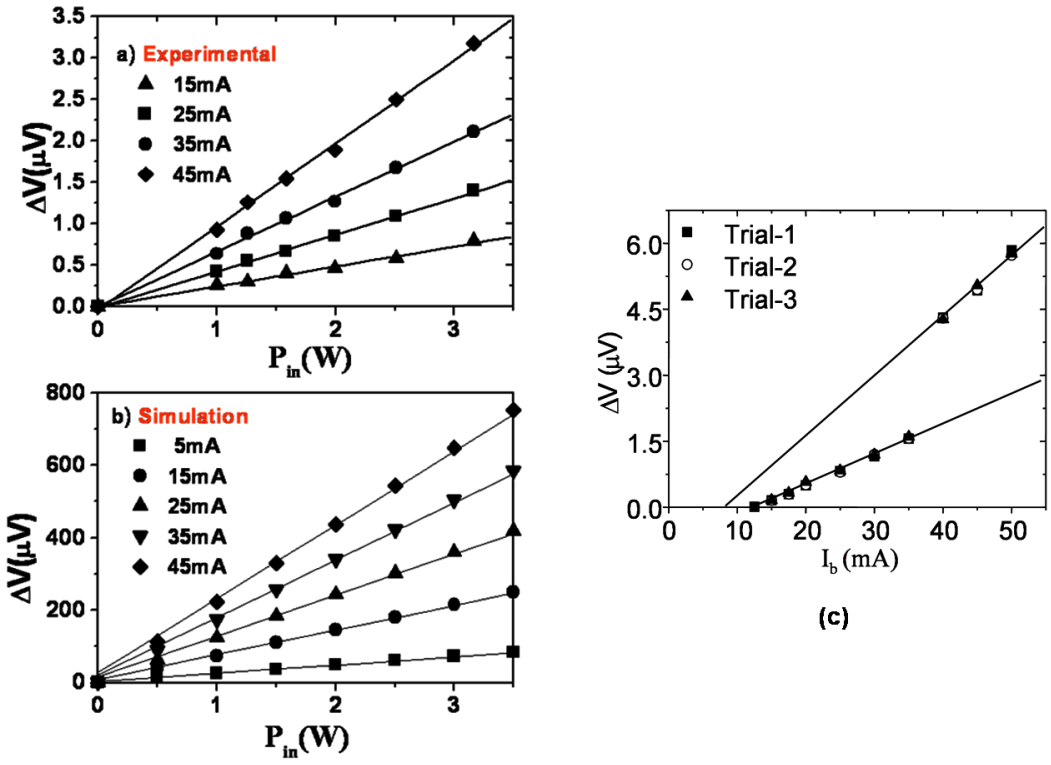

Fig.3.9 Microwave power dependence of the voltage response ΔV at different input bias currents obtained by (a) experiment and (b) simulation. (c) Bias current dependence of ΔV with nonlinearity appearing at currents above 40 mA.

For bias currents exceeding 40 mA, however, the response becomes non-linear (as shown in Fig.3.9(c)) and is accompanied by instability in ΔV due to sample Joule heating. Therefore, the linear dependence of the induced voltage to the input bias current and input microwave power only holds when sample heating by I_b is negligible as demonstrated by the deviated response in Fig.3.3.

3.3.3 Thickness Dependence

To determine the feasibility of using this technique on thicker films, the dependence of the induced voltage response to film thickness is investigated. Figure 3.10 shows that the voltage response at constant bias current decreases exponentially with increasing film thickness as given by the results from experiment and simulation. However, this result is actually a combination of two effects: the decrease in bias current density and decrease in microwave absorption as given by $A = \frac{2\xi}{(1+\xi)^2}$. Since $\Delta V = I_b \Delta R = I_b \frac{\Delta r \bullet l}{a}$ at constant bias current, increasing the film thickness will lead to an increase in effective area for the flux of charge carriers. This will then result to an effective decrease in bias current density

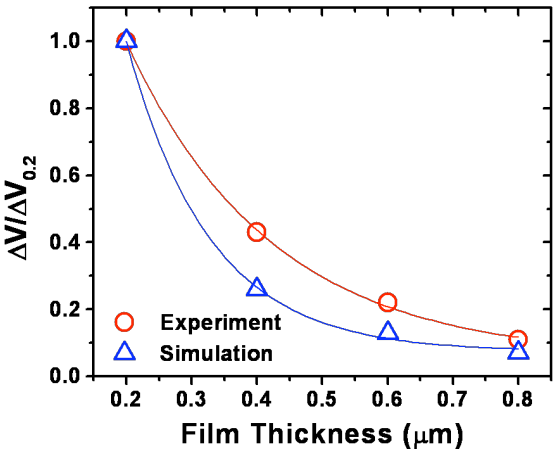

Fig.3.10 Film thickness dependence of ΔV for silver film at constant bias current obtained by experiment and simulation.

and thus a decrease in induced voltage. For the second case, since the coefficient ξ is directly proportional to film thickness $\xi = \frac{z_l}{s}$, then increasing ξ will result in a decrease in microwave absorption A. To disentangle the two effects, the two curves in Fig. 3.10 are normalized with respect to the bias current density and the resulting curves are shown in Fig.3.11. The thickness dependence curve obtained from the experiment now becomes linear while the curve obtained from simulation remains exponential. The discrepancy between the two results suggests that there may be additional mechanisms or mechanisms in the simulation that have not been considered. However, decreasing trends of ΔV in both curves imply less efficient microwave absorption in thicker films.

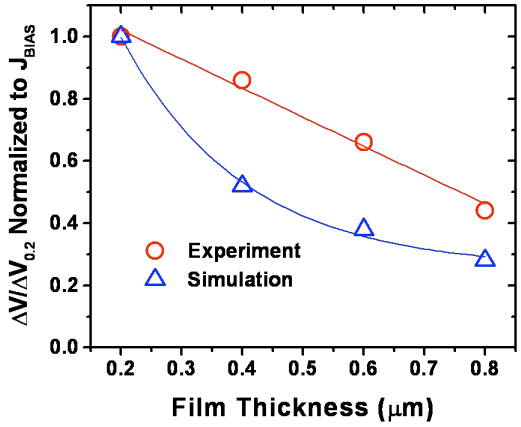

Fig. 3.11 Film thickness dependence curves normalized to bias current density.

3.3.4 ΔV Profile Across Film Width

A line scan profile of the induced voltage similar to the one acquired through experiment was obtained through simulation. A 5 mm wide bridge and a 200 μm tip diameter corresponding to the grid size were used but the ratio of the tip diameter to sample width was preserved. Fig 3.12 shows the results of the simulated ΔV line profile across the width of the silver bridge and it qualitatively agrees with

experiment. This follows from the fact that the temperature increase is greater at the edges compared to the center as provided by the temperature profile simulation and as discussed in section 3.1.2.

Simulation results show qualitatively comparable results with experiment where ΔV increases sharply at the edges while remaining flat and uniform in between. However, the ratio of ΔV at edge to center ($\Delta V_{edge}/\Delta V_{center}$) is higher for the experiment (~3) compared to the simulation (~1.04). If the heat lost to the substrate and the thermal conductivity approximation for thin films is considered, this ratio will be almost similar for experiment and simulation [Mishra 2006].

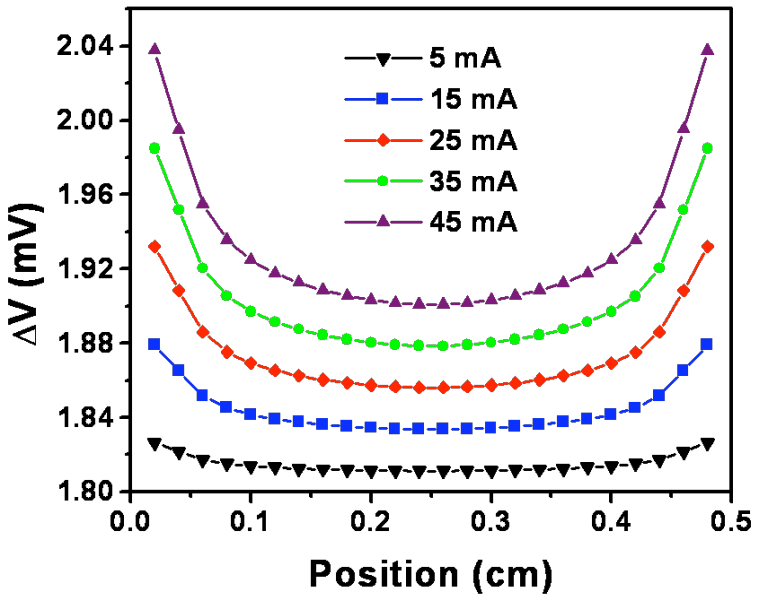

Fig.3.12 Simulated line scan profiles of ΔV across the width of a silver bridge at various I_b values [Mishra 2005].

3.4 Imaging Macroscopic Defects in Ag Films

A 1.5 mm wide and 200 μm thick silver film is deposited on a glass substrate and a transverse defect was cut out of one side forming a constriction to the current flow on the other side. A 50 μm probe tip diameter was used to perform frequency-sweep measurements and a bias current of 3 mA was used for induced voltage measurements. Figure 3.13 shows the results of the scans over a 2.5 x 1.5 mm area.

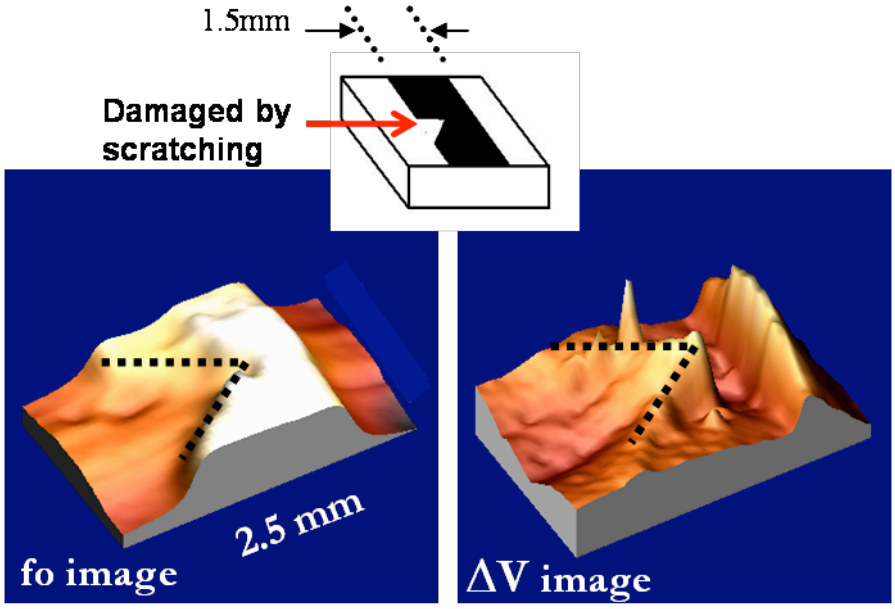

Fig. 3.13 Silver film with transverse defect cut out of one side. f_0 and ΔV images of the defect identifies defect with good sensitivity.

The bright regions in the resonant frequency f_0 image represent the silver film where the contrast is given by the change in morphology and change in material property (glass vs. silver) over the scan area. For the ΔV image, the edges of the film including the edges of the constriction are represented by the peaks in ΔV signifying higher rises in temperature due to restricted heat diffusion.

However, closer inspection of the ΔV line profiles along specific areas reveals more interesting information. Figure 3.14 shows two line scans: one along the right edge and the other across the width crossing the edge of the film and the defect.

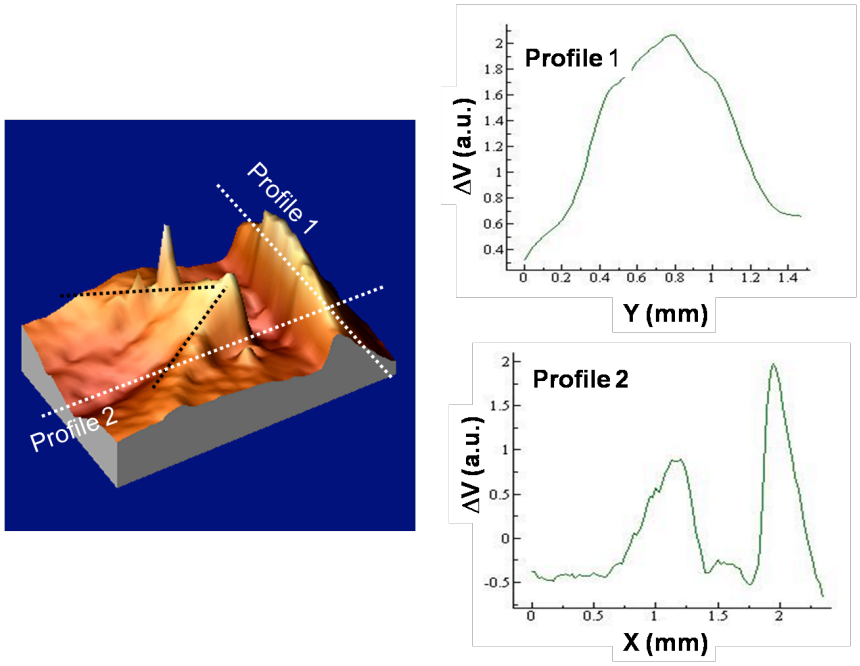

Fig. 3.14 ΔV line profiles along separate locations on the sample.

The first line profile shows non-uniform induced voltage along the right edge of the film. The peak of this line scan coincides with the location of the apex of the transverse defect. Also, the second line profile shows unequal magnitude of the two peaks corresponding to two edges. From the observations in section 3.2.4, the peaks of ΔV at the edges must be approximately the same. Therefore, the difference in magnitude in this case must be caused by either non-uniform heat diffusion or non-uniform current distribution. Since the ΔV is affected by both thermal and electrical properties of the sample, the uneven magnitude of the induced voltage cannot be attributed to a singular effect at this time.

Chapter 4

Room-temperature Application: Imaging Non-uniformities and Defects in HTS Thin Films

After performing measurements on silver films, the near-field scanning microwave microscopy (NSMM) technique showed promise and demonstrated its capability to image defects and non-uniformities with the unique feature of obtaining multiple complementary scans of the same surface area. The dependence of the induced voltage to the input bias current and input microwave power was re-investigated at room temperature for an $YBa_2Cu_3O_7$ (YBCO) thin and thick film to verify if the same heating mechanism still holds for a HTS film. At room temperature, YBCO has an electrical conductivity of about 0.33 $M\Omega^{-1}m^{-1}$ while silver has the highest electrical conductivity (~ 63 $M\Omega^{-1}m^{-1}$) and thermal conductivity (~420 W/mK) among metals. The two-orders-of-magnitude difference in electrical conductivity between YBCO and silver already gives an indication of how the two materials will also differ in terms of microwave absorption. Since the equation $A = \frac{2\xi}{(1+\xi)^2}$ *where* $\xi = \frac{z_1\sigma}{2}\sqrt{\frac{\mu_0}{\varepsilon_0}}$ shows that the amount of microwave energy absorbed by the film decreases with

increasing electrical conductivity, then YBCO should absorb more microwave radiation than silver.

The YBCO films used in these experiments were fabricated using pulsed laser deposition on 5x10 mm^2 single-crystal $LaAlO_3$ substrates. The deposition condition was optimized to yield high T_c values in the range of 89-90 K and J_c values in the range of 3-5 MA/cm^2 at 77K and self field. The deposition temperatures were in the range of 760-770 ºC and the oxygen partial pressure was ~240 mTorr. The laser energy density was around 2.5 J/cm^2 at a repetition rate of 10 Hz. Silver contact pads were laid on the edge of the samples via dc sputtering and annealed in oxygen at 500^{o}C for 30 minutes to reduce contact resistance.

Several YBCO samples with varying defects were then prepared and scanned with the NSMM to image both microwave properties and induced voltage to assess the capability of the technique for defect identification. This includes a sample with a defect whose dimension perpendicular to current flow is two orders of magnitude smaller than the sample width. These types of defects may not affect current flow as much but they are still potential sites for nucleation of hotspots that may eventually lead to thermal quench.

Finally, we also attempt to improve the sensitivity of the measured induced voltage without sacrificing the spatial resolution.

4.1 Bias Current and Microwave Input Power Dependence of the Induced Voltage for Thin and Thick Films

The large wavelengths of the microwave provide an advantage of deep penetration of microwave as compared to visible lights. To determine the experimental feasibility of applying the NSMM-transport technique to both thin and thick YBCO films, the induced voltage ΔV was measured as function of the NSMM probe's input microwave power (P_{in}) at various sample bias currents for two unpatterned 5 x 8 mm YBCO films with thicknesses of 250 nm and 2.5 μm. A probe with tip T1 was used for this experiment and microwave pulses were radiated on an area close to the edge so that optimal microwave heating will be achieved and maximum measurable response can possibly be detected. The linear dependence of ΔV on P_{in} observed on both YBCO samples, as shown in Fig. 4.1(a), is consistent with the results previously reported on silver films.

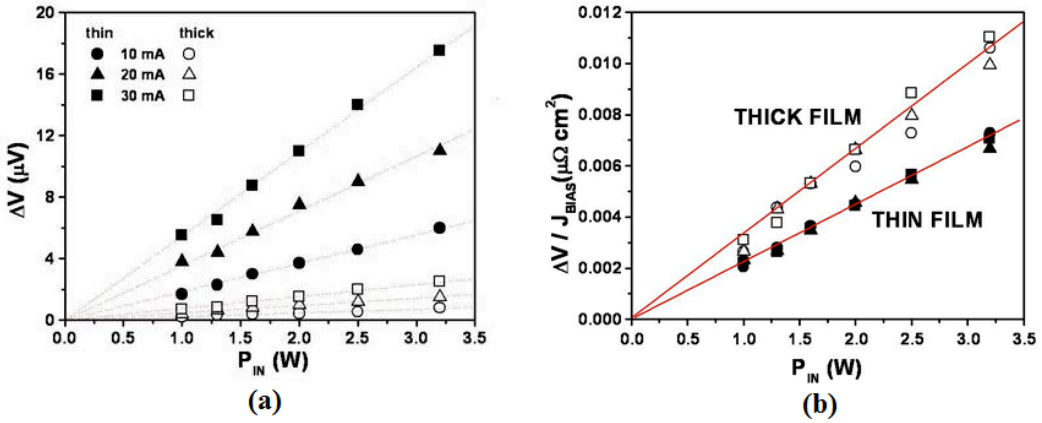

Fig. 4.1 (a) Dependence of the induced voltage to the input bias current and microwave power for a thick and thin YBCO film. (b) Normalized curve.

The magnitude of the induced voltage, however, is larger compared to silver. This is due to the fact that the YBCO room temperature resistivity is greater than that for silver. Thus, more heat is generated through energy transfer because of the increased number of collisions between the charge carriers and the lattice. Also noticeable is the fact that the induced voltage at a constant bias current decreases dramatically when the thickness is increased one order of magnitude. This is expected since an increase in thickness results in an increase of the cross-sectional area for the carriers and thus a decrease in current density.

When normalized to the current density, as shown in Fig. 4.1(b), the $\Delta V/J_{bias}$ values for either thinner or thicker sample fall on the same linear curve as expected. Interestingly, the slope of $\Delta V/J_{bias}$ vs. P_{in} curve for the thicker YBCO film is comparable to, in fact slightly higher than, that of the thinner YBCO sample even though they have an order of magnitude difference in thickness. This is in sharp contrast to what happens in silver where the ΔV decreases dramatically as thickness increases. Thus, the number of carrier-lattice collisions in YBCO doesn't reduce much when thickness is increased compared to a significant drop in the number of these types of collisions when the thickness of silver is increased. This result can be attributed mainly to the difference in electrical resistivity of the two materials. This result also reinforces the notion that microwave heating is fairly uniform through the thickness of both thinner and thicker YBCO films studied. Furthermore, the fact that the slope of the $\Delta V/J_{Bias}$ curve for the thicker film is slightly higher than that of the

thinner film may be attributed to the lesser boundary effect at larger thickness therefore reduced heat loss from the hot spot. This result suggests that the combined NSMM-transport technique is applicable to YBCO films with thicknesses of several μm.

4.2 ΔV Profile Across Film Width

Using a probe with tip T2, line profiles across the width of a 5-mm wide, 250-nm thick unpatterned YBCO sample were obtained. Fig.4.2(a) shows the resonant frequency line scan of the sample where the sharp transitions correspond to the edges of the film. The step size was 100 μm.

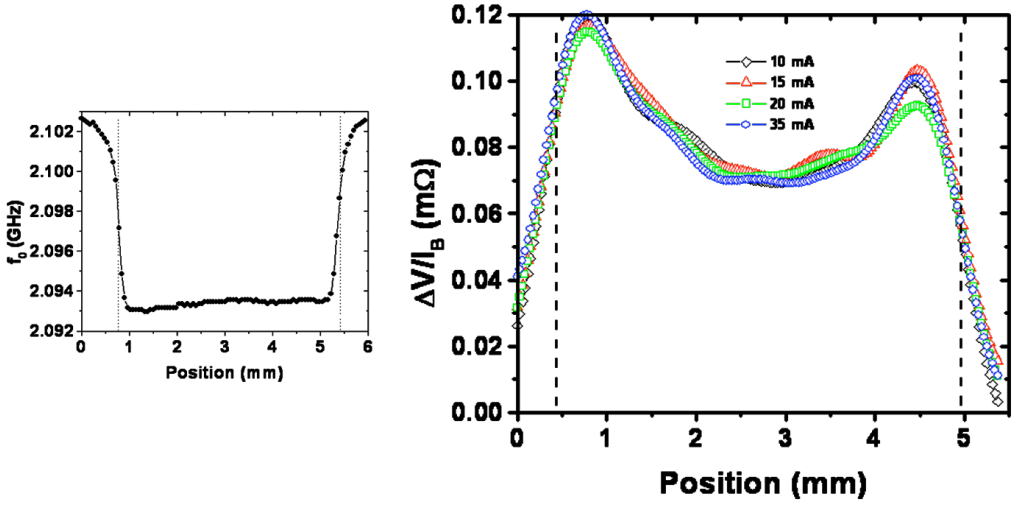

Fig. 4.2 Line scan profiles of (a) the resonant frequency f_0 and (b) induced voltage ΔV for an unpatterned YBCO thin film

Figure 4.2(b) depicts the induced voltage line scans at different bias currents for the YBCO thin film. The curves were again normalized to bias currents so they fall approximately on top of each other. Notice that the line scans obtained for YBCO extends much farther out from the edges compared to the line scans obtained for silver in Section 3.1. This was done to illustrate the effects of long-range interaction existing between the NSMM tip and the sample which becomes more pronounced and obvious in YBCO because of its higher resistivity and higher microwave absorption. Even when the probe is approximately half a millimeter away from the sample edge, the sample already shows evidence that it is affected by the microwave radiation. It should also be noted that the dashed lines in the plot represents the actual film boundaries and the assumption is that the peaks of the scan should coincide with the location of the film's edges because these boundaries will inhibit uniform heat diffusion and thus lead to higher rises in temperature. Initial observation will tell that the peaks do not exactly coincide with them. Once more, this effect is due to the varying amount of microwave power delivered to the film as the NSMM makes its approach from outside the boundaries. The probe position is assumed to be along the central axis of the probe tip (see Fig.4.3). Thus, for a tip with finite diameter, when the axis is assumed to be at the edge of the sample, only half of the tip diameter is inside the sample edge and the other half still

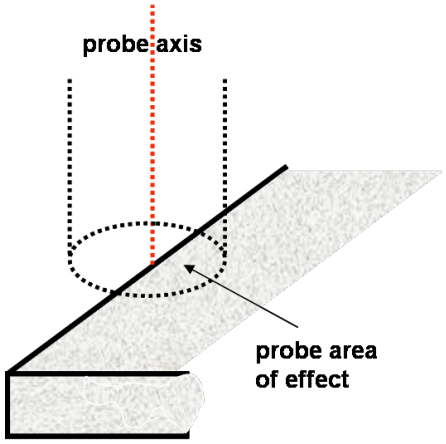

Fig. 4.3 Illustration of the NSMM probe's area of effect as it moves toward sample.

is outside. The maximum induced voltage will only be achieved after the whole tip diameter is already within the bounds of the sample. The offset in this case amounts to approximately half the tip diameter. This offset is expected to decrease if a smaller tip is used. However, using a smaller tip will then cause the dimension of the hot spot to decrease and make the induced voltage possibly undetectable.

Another observation is the difference in magnitude between the left and right peaks. A simple explanation for this is the small tilt in the sample with respect to the scan direction. This is also noticeable in the f_0 scan where one edge is a bit higher than the other. Thus, since the probe is closer to the sample on one edge than the other, a difference in microwave absorption between these two points is expected. Finally, the shape of the ΔV curve is more parabolic in the middle of the YBCO compared to a flatter shape in the silver film. This is caused by the slower heat diffusion in YBCO due to its higher resistivity. So when the probe moves to the next spot, a small amount of heat may still be present in that area. The succeeding hot spots will then be affected by the previous one.

4.3 Imaging Defects in YBCO Films

4.3.1 Mechanical Defects

Several large-area YBCO thin film samples were prepared with each one having different types of mechanical defects on the surface. The sizes of both the samples

and defects were so scaled as to approximate what might actually exist in real practical situations where coated conductors have widths of several millimeters to a centimeter.

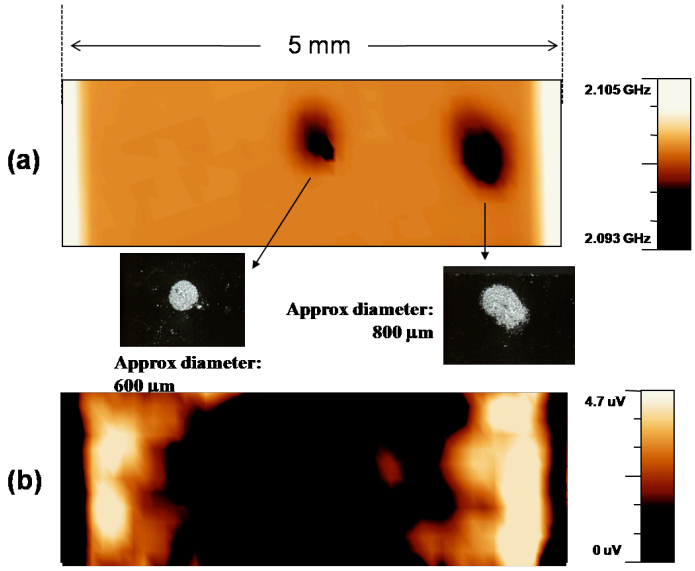

Fig.4.4 (a) Resonant frequency and (b) induced voltage scans of a YBCO sample with 2 drop of liquid Ag paste on the surface.

Two small beads of liquid Ag paste were dropped on the surface of the first sample. These types of materials can represent particulates that may adhere to the sample surface and possibly affect its properties. Figure 4.4 shows the resonant frequency and induced voltage scans of this sample. The f_0 scan was able to resolve the drops of Ag paste on the sample surface primarily because they present themselves as morphology variations. As the probe scans above these defects, the decrease in resonant frequency is due to the increase in capacitance between tip and sample brought about by the reduction of the tip-to-sample distance. Surrounding the solid black spots are lighter shades of dark color which shows that the slopes of the Ag

drops are contoured and not sharp-edged. The induced voltage scan, on the other hand, does not show the presence of the Ag spots. Instead, the familiar bright regions at the edges of the sample showing induced heating are visible. The absence of a structure or form that suggests the presence of the Ag drops in the ΔV image implies that the Ag drops do not greatly affect the heat diffusion in the YBCO sample nor do they cause non-uniformity in the current flow. The amount of heat absorbed by the small drop of Ag is either dissipated faster or is negligible compared to the heat absorbed by the YBCO sample.

Using a diamond scribing pen, three scratches, each having an approximate length of 1 mm and width of 100 μm, were carved on the surface of the second sample. Fig. 4.5(a) shows an optical photograph of the sample with the 3 manually-scratched defects. Two line-defects, perpendicular and diagonal to the current flow, were placed at the edges of the sample while the third defect was placed in the middle of the sample parallel to current flow. To scan the microwave properties, a probe with tip T4 was used to perform both frequency- and time-domain microwave measurements. An area of 5 mm x 2mm with 25 μm step size was scanned over the surface of the sample. The f_0 and $\mathbf{S_{11}}$ were imaged and depicted in Figs. 4.5(b) and 4.5(c) respectively. Since the probe was carefully tuned having high Q ~ 2000, it was sensitive enough to detect a 3 MHz change in resonant frequency and over a 30 dB shift in microwave reflectivity.

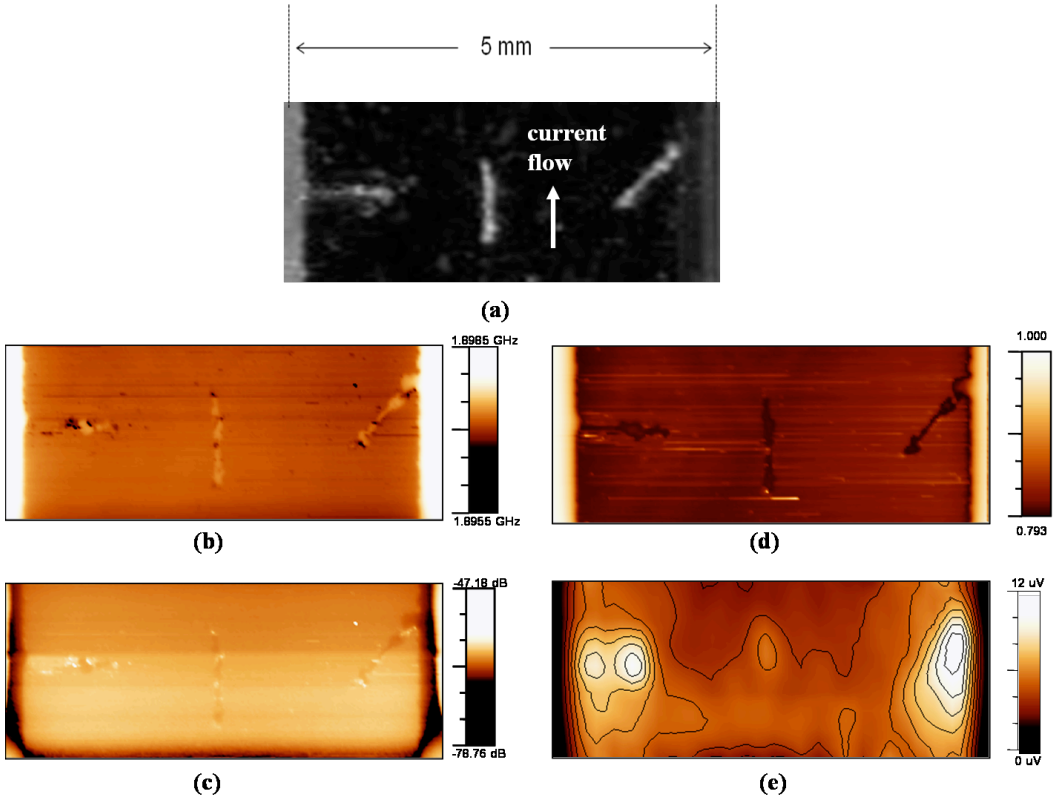

Fig 4.5 Images and 2D maps of YBCO sample with 3 manually-scratched defects. (a) Optical image from a microscope as captured by a CCD camera. Arrow points to direction of current flow. The next four images are spatial maps of (b) resonant frequency, (c) S_{11}, (d) microwave reflected power and (e) ΔV response. Maps (b), (c) and (d) were obtained with a 25 μm-tip probe while map (e) was obtained with a 200-μm tip probe.

For the f_0 scan, notice that the sample surface is represented by a darker shade and the defects are represented by light-shaded lines. When the probe scans across the defects, an increase in resonant frequency was detected due to an increase in probe tip-to-sample distance. This qualitatively describes the gap in the material created by the scratch that was carved on the sample. The opposite description applies for the $\mathbf{S_{11}}$ scan. Dark regions correspond to areas with lower microwave reflectivity and thus higher microwave absorption. From this scan, the three defects represent areas where

microwave absorption is greater and thus heating is potentially greater. Also, notice that the edges have an extremely high contrast in $\mathbf{S_{11}}$ from the rest of the sample surface. This supports the claim that microwave heating is enhanced at the edges because of restricted thermal diffusion as shown in the simulation. Fig. 4.5(d) shows the spatial distribution of the reflected microwave power over the surface of the sample with three defects. Compared to the f_0 and $\mathbf{S_{11}}$ scans, this map offers better contrast because of better instrument sensitivity. To obtain the ΔV scan, a larger probe tip T2 was required so that a detectable change in sample resistivity can be obtained. The 2D map of ΔV is shown in Fig. 4.5(e) at a fixed I_b = 20 mA. The bright spots in the image correspond to regions of higher ΔV and thus higher change in resistivity. Correlating this image with the other scans, the location and shape of the bright regions actually match the scratched defects. Furthermore, the two defects on the edges generate more heat than the one at the center. This can be attributed to two factors. First of which is the location of the defects. Higher ΔV is already expected at the edges of the sample because of the reduced heat diffusion. Defects located near or at the edges will only make the detected ΔV stronger because they can also be viewed as boundaries to heat diffusion in addition to having more charge carriers crowd around these obstacles. Secondly, the orientation of the defects (almost perpendicular to current flow) effectively makes them planar obstacles to current flow thereby introducing thermal instabilities near these regions [Gurevich 2001]. The combined effects of these two factors accounts for the higher ΔV around these defects compared to the one at the center. Also, the fractional length of the center defect that actually

affects or hinders current flow is almost an order of magnitude smaller than its edge defect counterparts. The width of this center defect is only 0.10 mm and we can imagine that current can easily go around its edges. The other two defects, meanwhile, occupy almost 1.0 mm and 0.8 mm of the sample width causing a much larger deviation in the normal current flow. In this case, defects with lengths that run parallel to the current flow may be harder to detect using the other hot spot techniques since these defects would generate only a small amount of heat.

4.3.2 Defects with Small-Dimension Current Obstruction

To further explore the capability of the current set-up, two 0.25-μm thick, 5x10 mm YBCO samples with defects located at the center and with its orientation running parallel to current flow were prepared. The first sample D1 has a defect created by manual scratching using a diamond scribing pen (YBCO is partially removed at the scratch) while the second sample D2 has a defect created with standard photolithographic processes and wet etching (YBCO was completely removed at the defect). The dimensions of both defects are approximately 100 μm wide and 1 mm in length. Figs. 4.6(a) and 4.6(c) show the two dimensional ΔV scans for samples D1 and D2, respectively.

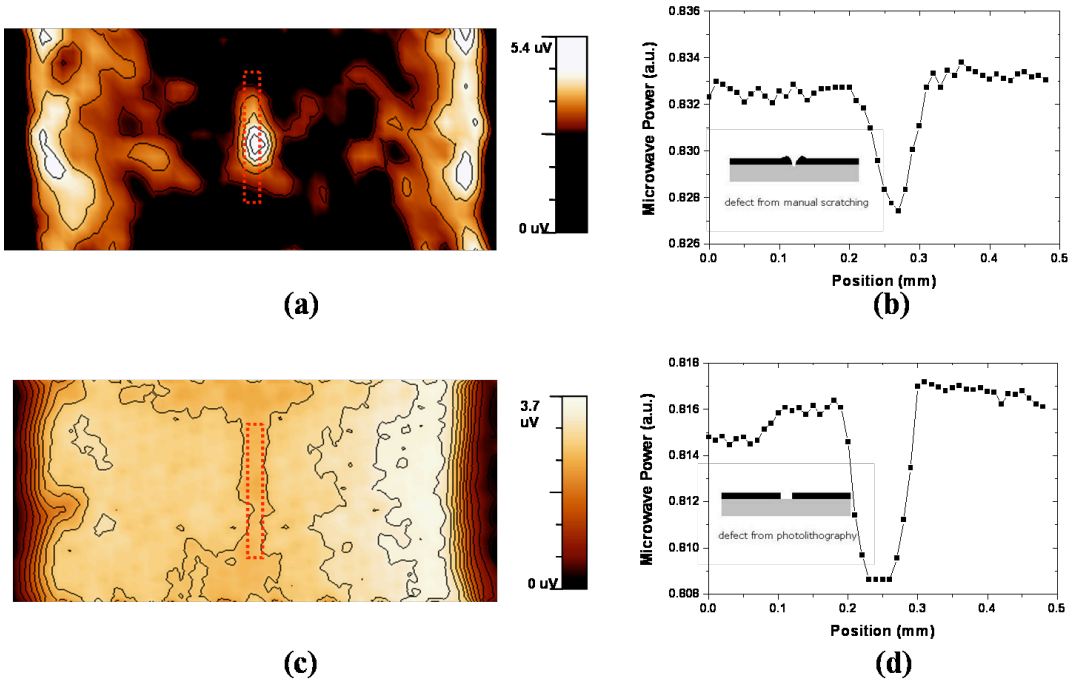

Fig 4.6. (a),(c) 2D maps of ΔV for YBCO samples with manually scratched defect and lithographically fabricated defect, respectively. Dashed rectangle depicts actual location of defect. (b),(d) Line scan profiles of the microwave reflected power across the manually-created and lithographically-created defects, respectively. Cross-sectional renderings of both defects are shown on inset of each.

For the manually-created defect in sample D1, the bright regions in the ΔV scans reveal the location of the defect. This region corresponds to higher localized heating and thus higher change in resistivity in the vicinity of the defect. However, the lithographically-created defect in sample D2 appears as a darkened region in the 2D ΔV scan. The difference can be attributed mainly to the density of material that is affected by microwave heating near these areas. When the scratch was made on sample D1, the force on the diamond scribing pen compressed the materials on the edge of this defect. Thus, it is expected that microwave heating induces higher changes in local temperature simply because of the increased density of material in this region due to scratching. For the case of the lithographically-created defect, the

material in the defect area was removed. Therefore, it is expected that the temperature will have less or no change at all when microwaves are applied to this region. In either case, the ΔV scans were able to identify each defect and show regions of non-uniform local dissipation.

It is also noteworthy that the effective dimension of the defect (100 μm in both D1 and D2) that contributes to current obstruction is only 2% of the sample width (~5 mm). The fact that these small defects can be detected by the ΔV scan demonstrates the high sensitivity of the NSMM-transport technique. Although these types of defects don't affect current flow as much, locating them may still be important to since they could still potentially be nucleation areas for hot spots that could eventually force the sample to quench. Figs. 4.6(b) and 4.6(d) represent reflected microwave power line scans from both samples across the defect. A 500 μm line scan across the defect was obtained from each sample using a 10 μm diameter tip and a step size of 10 μm. Comparing these two line scans, two observations are of important consideration. First is the shape that defines the defect. For Fig. 4.6(b), the wedge-type shape supports the idea that a sharp conical solid material created the defect. For Fig. 4.6(d), meanwhile, a flat region at the base of the defect is obtained confirming a square-well type defect created by photolithography. The second notable observation is the similarity in the magnitude of the change in the microwave power absorption between the two scans. Considering the change in microwave reflectivity may quantitatively correlate to the depth of the defect, Fig. 6(d) shows an

approximate 0.007 a.u. change in the reflected microwave power, which roughly translates to the thickness of the sample. Since Fig. 6(b) also shows a similar 0.007 a.u. change at the same experimental setting, the scratch on sample Y1 may puncture through, or at least close to, the entire thickness of the film. Lastly, if the resolution is defined to be 10% to 90% of a step width, then both reflected power line scans reveal a 30 μm resolution over the 5mm sample width. Also, the obtained resolution of 100 μm per 5 mm sample width in ΔV scan is significantly better than the 60 μm resolution per 100 μm sample width obtained in room temperature laser scanning microscopy (RTLSM) [Klein 2002]. Since the ΔV maps correlate well with the microwave maps, non-contact diagnostics may be possible by simply using the NSMM to map microwave properties at room temperature with an even better spatial resolution. These results show that the combined NSMM-transport technique can provide complementary information necessary for identification of the current-obstructing defects (CODs) and for understanding their role in electrical current obstruction.

4.3.3 Secondary Phase Inclusions

Secondary phases are non-conducting or insulating materials embedded in the HTS material. This type of defect reduces the effective area where the supercurrent can flow in the material thereby limiting its current carrying capability. Furthermore, they can act as weak pinning centers for the magnetic vortices and eventually lower the critical current density of the superconductor. Thus, identifying this type of defect is

as important as locating the mechanical ones. However, the ability to locate them in a given sample remains a challenge because they don't necessarily take a definite form and the extent of their effect on the flow of current is not something that can be readily known, especially at room temperatures.

Since the microwave probe is capable of detecting materials of different conductivity and dielectric constant, the developed technique may be used to identify secondary phase inclusions even at room temperature. To verify this capability, a YBCO sample with a patterned material modulation was prepared for scanning. A standard TEM grid was used as a mask to etch away part of the YBCO thickness via ion milling. The holes generated were then backfilled with MgO material at a thickness approximately equal to the amount of thickness etched away. This is done to ensure that morphology variations due to the patterns that separate the YBCO and MgO materials will be kept to a minimum.

A microscope photograph and cross sectional schematic of the fabricated sample is shown in Fig. 4.7(a) and 4.7(b), respectively. A probe with tip T5 was used to scan a 60 μm x 60 μm area on this surface with a step size of 1 μm. The 2D image of the reflected power is shown in Fig. 4.7(c). The dark regions in this scan signify regions of lower microwave absorption and in this case also represent the MgO material. Although the material variation could be clearly identified, the boundaries were not as sharp as the one given in the optical microscope photograph. One factor that could

have affected this is the size of the probe which is approximately half the size of the void. Therefore, the probe will be above one specific boundary for several steps and detecting several levels of reflected power as it moves across the sample surface.

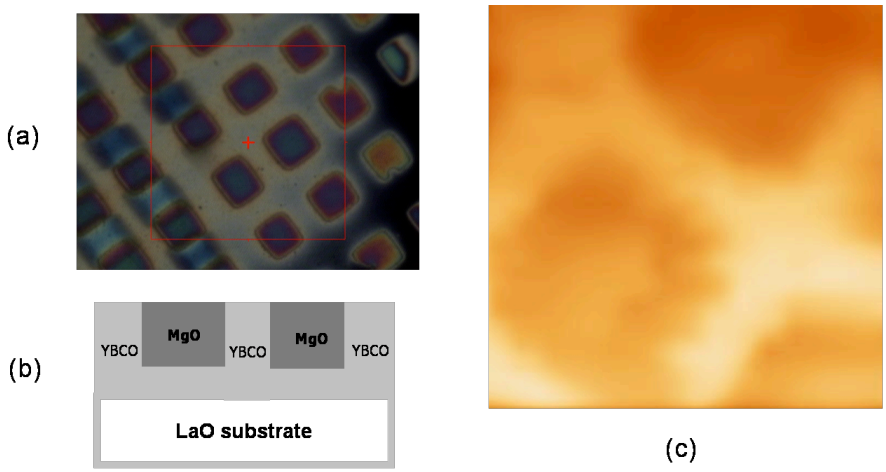

Fig.4.7 (a) Microscope photograph (200 x 150 μm) and (b) cross-section schematic of the YBCO sample with embedded MgO pattern to form material modulation. (c) 2D 60 x 60 μm image of the reflected power obtained using the NSMM.

An attempt to image the induced voltage on the sample surface was unsuccessful. A simple justification would be that the YBCO material was not completely etched through before the MgO material was grown on top of the milled holes. This allowed current to be shorted beneath the MgO patterns and avoid passing through the obstacles. When the microwave probe was used to heat the local spots on the sample, the heat diffusion was uniform and no modulation was detected.

4.4 Improving Spatial Resolution and Sensitivity

One of the apparent contradictions in the current NSMM-transport system is the need for two separate tips: (i) a small tip tapered to submicron size for NSMM imaging of

high spatial resolution and (ii) a large tip for emission of adequate microwave irradiation to generate detectable hot spots for sensitive detection of the ΔV. Since $\Delta V = J_{bias} l \bullet \frac{\partial \rho}{\partial T} \Delta T$ directly correlates with the hot spot dimension (which is comparable to the NSMM tip diameter ϕ), temperature coefficient of resistivity and the temperature variation at the hot spot, the detectability of ΔV is dictated by ΔT if ϕ is small. To address this issue, we have adopted a higher harmonic resonance of NSMM to significantly enhance the local microwave power density, which generates higher ΔT and results in a detectable ΔV at a submicron tip diameter of the NSMM.

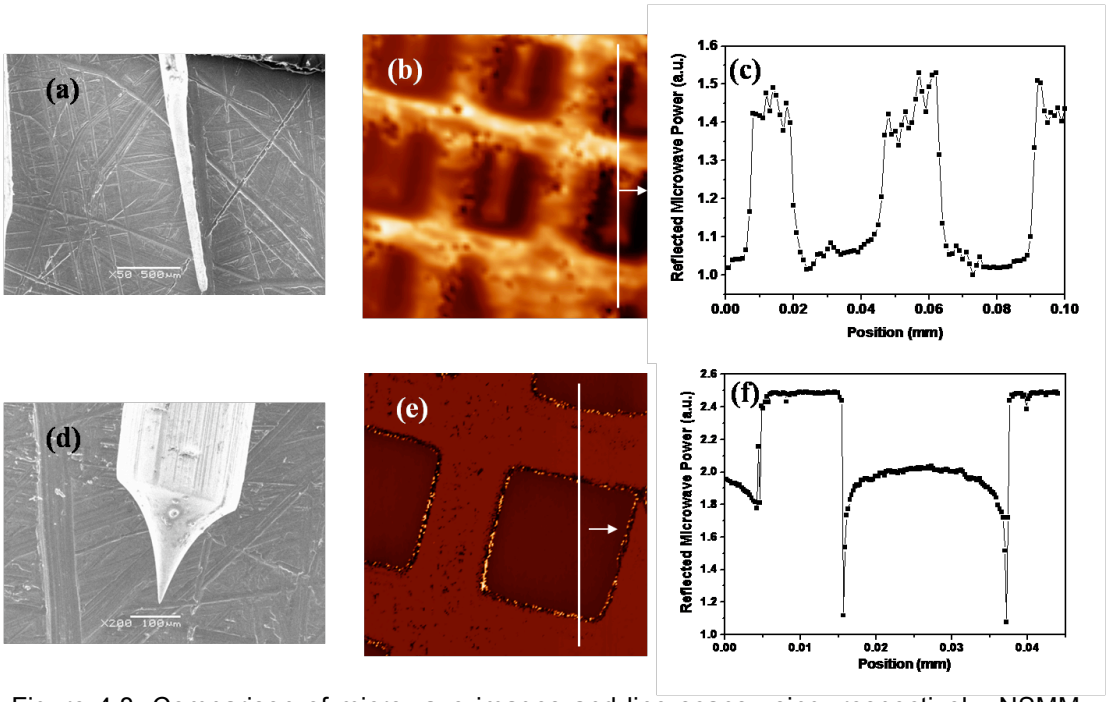

Figure 4.8. Comparison of microwave images and line scans using, respectively, NSMM probe tips T5 and T6: (a) SEM image of a 5 μm Cu tip (T5) and the corresponding (b) 2D (c) and 1D reflected microwave power scans of a TEM grid showing a step resolution of ~ 3 μm; (d) SEM image of an 800 nm W tip (T4) and the corresponding (e) 2D and (f) 1D reflected microwave power scans of the same TEM grid. Sub-micron step resolution of 400 nm was achieved.

Figures 4.8(a) and 4.8(d) show the SEM images taken of the chemically-etched long and thin Cu tip T5 and the electrochemically-etched tungsten (W) tip T6, respectively. A two-dimensional microwave scan of the reflected power from a TEM Cu grid was obtained using each tip. Fig 4.8(b) shows a 60x60 μm area scanned by the Cu tip in 1 μm step sizes while Fig 4.8(e) shows a 40x40 μm area scanned by the W tip in 200 nm step sizes. It was not appropriate to use the same step sizes for both scans since the differences in tip diameters almost approximate an order of magnitude. Using a very small step size on the large-diameter tip would make some of the points on the scan redundant in addition to the long scan time. Using a large step size on the small-diameter tip, on the other hand, would defeat the purpose of increasing spatial resolution since it would definitely force the scan to miss some points of interest. The difference in resolution is clearly evident from the 2D scans and can be further supported by the line scans [Fig 4.8(c) and 4.8(f)] obtained across the grid using each tip. In contrast to a spatial resolution of about 3 μm achieved using T5, a much better spatial resolution of about 400 nm was obtained with tip T6, which is ~2.6×10^{-6} λ (microwave wavelength).

With the significantly reduced tip diameter, this W probe tip is expected to generate a very small hot spot on which the ΔV may be undetectable without further increasing the intensity or power of the incident microwave radiation. Indeed, no ΔV can be detected by simply implementing the new W tip on our NSMM-transport system even at the maximum power allowed by our microwave source. To resolve this issue, the

NSMM was tuned to its 2nd harmonic frequency to take advantage of a superconductor's frequency-dependent surface resistance. Increasing the frequency of the incident radiation should increase the intensity of the induced voltage because the microwave surface resistance of a superconductor increases with frequency. Fig. 4.9 compares the induced voltage ΔV normalized with respect to the bias current density on both the thin [Fig. 4.9(a)] and thick [Fig. 4.9(b)] YBCO samples using probe tips T5 and T6. The resonant probe was tuned to the fundamental frequency f_0 when T5 was used while the tuning was adjusted to the 2nd harmonic frequency $2f_0$ when T6 was used. Notice that the $\Delta V/J_{bias}$ obtained for both films is higher with T6 at the 2nd harmonic frequency. This supports the fact that the microwave radiation at the 2nd harmonic frequency results in a higher change in hot spot temperature and larger $\Delta V/J_{bias}$.

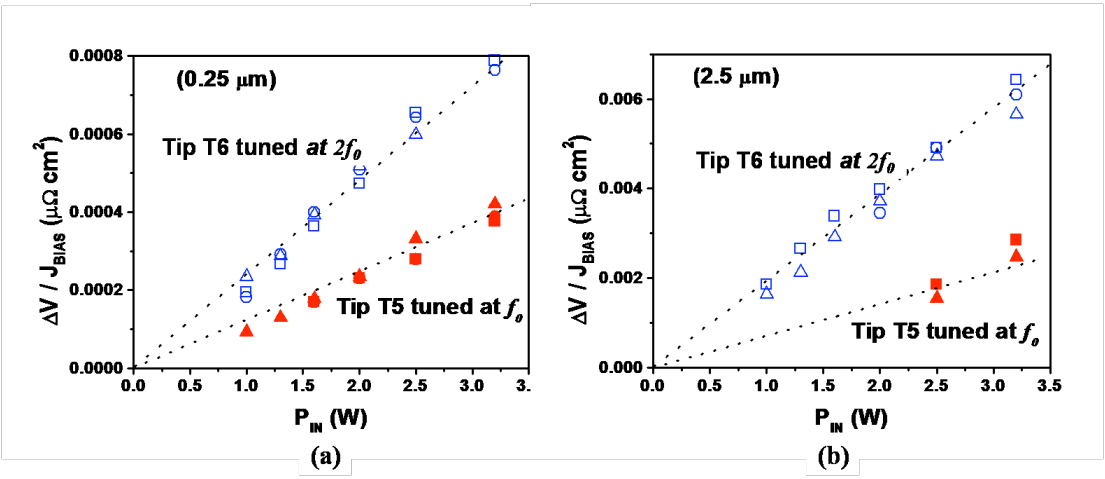

Figure 4.9. Comparison of the induced voltage normalized to bias current density using probe tip T5 tuned to the fundamental resonant frequency and probe tip T6 tuned to the 2nd harmonic frequency on the (a) thin and (b) thick YBCO samples, respectively.

Chapter 5

Low-temperature Application: Detecting Local Dissipation in Bulk and Grain-Boundary Regions in YBCO Microbridges

At room temperature, the capability of the NSMM to image various types of defects that may affect the current-carrying capability of the superconductor was demonstrated. At low temperatures, changes in the material properties (most notably, dissipation) of the superconductor experience a drastic change during the normal-superconducting transition. With improved sensitivity, this portion of the study seeks to demonstrate the capability of the system to detect temperature- and current-dependent dissipation at low temperature and show that the NSMM can be used as a non-destructive and non-contact system to observe dissipation. If the system demonstrates sufficient sensitivity, the NSMM may be able to detect dynamical evolution of the dissipation below the transport critical current criterion. This unique capability can then be utilized to observe thermal instability of the self-heating effects of a superconducting sample by measuring the time evolution of voltage and the reflected microwave signal at a constant bias current and fixed temperature which could provide insight on how dissipation locally evolves in the sample.

The sensitive detection of low-level dissipation by the NSMM can then be utilized to compare dissipation both at a grain boundary (GB) and in bulk regions for low-angle and high-angle misorientations. These results may provide insight into how the dissipation develops across a grain boundary versus a bulk region of a superconducting sample.

The YBCO films used in these experiments were fabricated using a method similar to the one used for the previous samples. Microbridges of dimension of 400 μm (Length) x 40 μm (or 20 μm in width) were then patterned on the 250 nm-thick sample using standard photolithography. Silver contact pads were laid on the edges of the samples via dc sputtering and annealed in oxygen at 500 ^{o}C for 30 minutes to reduce contact resistance.

5.1 Detection of Temperature and Current-dependent Dissipation at the Superconducting State using NSMM

Fig. 5.1 depicts the dependence of the microwave reflectivity (S_{11}) on the sample temperature at three different points along the length of the microbridge (see top right-hand corner inset). A resistance-temperature (R-T) curve was obtained simultaneously and is shown as an inset. Although both S_{11}-T and R-T curves reveal the superconducting transition, the transition detected in the S_{11}-T curves seem to vary from spot to spot. In addition, the transition temperature on the S_{11}-T curve is

typically lower by 1-2 K than that on the ***R-T*** curve of T_c = 88.5 K. A possible explanation is the microscopic inhomogeneity across the sample. Since the NSMM probe measures a local spot while the transport measurement detects the global effect, the transition measured by the NSMM is the transition on the selected local spot while that by transport, disappearance of the superconducting "shorts" in the microbridge occurring typically at a higher temperature. Below T_c, S_{11} is almost constant since the surface impedance of the superconductor at this temperature becomes infinitely small and further changes can no longer be detected by the NSMM. At temperatures above T_c, however, the surface impedance has weak temperature dependence which should account for the variations in S_{11} in this temperature range.

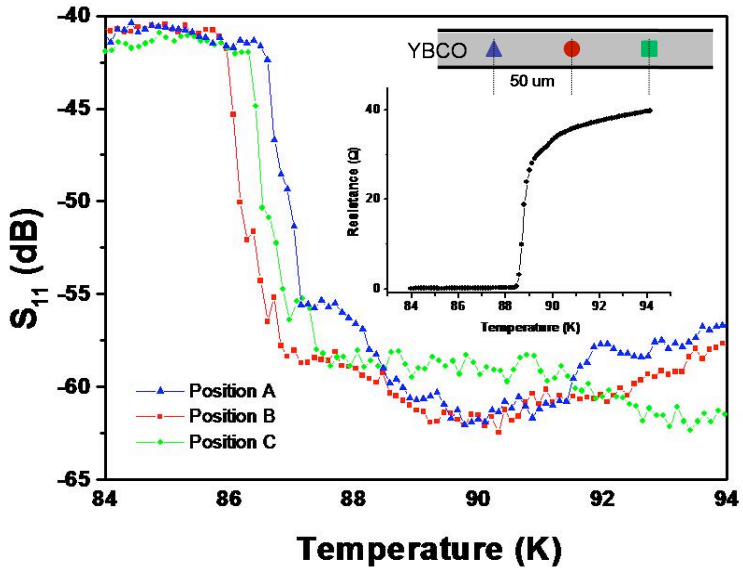

Fig 5.1. Temperature dependence of the microwave probe's reflectivity S_{11} at various points along the length of the HTS sample. Curve Inset: R-T curve obtained simultaneously. Top-most Inset: Approximate locations of the measurements separated by distances of 50 μm.

Previous works have shown the capability of the NSMM to correlate changes in the resonator's properties with the transition to superconductivity when the temperature is increased [Anlage 1999, Lann 1999b, Wu 2002, Feng 2003]. The S_{11}-T curve obtained in this work exhibits a sharper transition demonstrating improved sensitivity in our NSMM. Furthermore, our experimental set-up provides simultaneous measurements of S_{11}-T and R-T which enables a direct correlation between the information obtained using the NSMM and transport approaches.

The superconducting-to-normal transition can also be induced by ramping the electrical current up to exceed the I_c at a given temperature. Such a process has not been studied so far with NSMM although the information is important to understanding the dissipation evolution in a superconductor. Fig. 5.2 shows the changes in the 2nd harmonic frequency $\Delta(2f_0)$ with increasing bias current at 84 K. The corresponding current-voltage (I-V) measurement conducted simultaneously with the microwave measurement is superimposed for comparison.

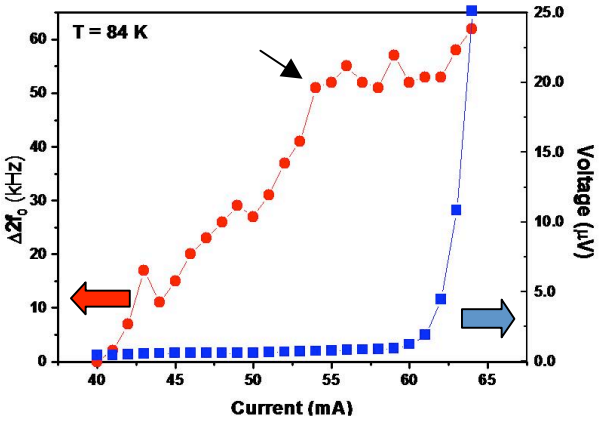

Fig 5.2. Voltage and $\Delta 2f_0$ as a function of current at 84 K.

The I_c was reached at around 62 mA using the criterion of 1 μV/cm. Interestingly,

$\Delta(2f_0)$ increases monotonically with the bias current in the entire range of the current. In the lower current range below I_c in which the transport measurement detected only "noise" background, the slope of the $\Delta(2f_0)$-I curve is approximately linear indicating a steady development of dissipation with increasing current. This monotonic increase in $\Delta(2f_0)$ suggests that the NSMM can sensitively detect low-level dissipation that is not apparent in the transport measurement. For type II superconductors, it has been well established that dissipation can occur at any temperature below T_c as soon as magnetic vortices start to penetrate the superconductor. With increasing current through the YBCO microbridge, the driving force on the vortices increases monotonically, in addition to the increasing number of the vortices due to the self field. The results shown in Fig. 5.2 seem to be qualitatively consistent with the enhanced vortex motion and indicate the higher sensitivity of the NSMM in detection of the low-level dissipation that cannot be detected with the transport approach.

It is important to quantify the sensitivity limit of the NSMM. Recently, Thompson *et al.* provided a unique approach in characterizing supercurrent conduction over ~8 decades of dissipation [Thompson 2008]. They supplemented the results from conventional transport by using magnetometry in a swept magnetic field and "flux creep" measurements to obtain I-V characteristics below the limit of the transport measurement. Their results demonstrated continuity of the I-V curve in the form of $V \sim I^n$ and provide clear evidence that dissipation indeed develops even at extremely low currents. Based on this discussion, we measured the microwave resonance

frequency shift $\Delta(2f_0)$ when the bias current through the sample is ramped across six decades from ~10^{-7} A to I_c to assess the sensitivity limit of the NSMM.

Fig. 5.3 shows the result obtained at temperatures of 84 K and 87 K. It is clearly shown that the monotonic $\Delta(2f_0)$-I curve extends to low currents, about 3-4 orders of magnitude smaller than the I_c defined by the transport measurement. This limit may be extended to lower current with optimization of the NSMM. At higher temperature, the dissipation develops faster, which is expected since less energy is required to de-pin a vortex. Interestingly, a kink indicated with black arrows in Figs. 5.2 and 5.3, is visible on the $\Delta(2f_0)$-I curve as the slope of the $\Delta(2f_0)$-I curve reduces considerably when approaching I_c. While the microscopic mechanism is unknown at this point, we speculate that the development of dissipation in an YBCO microbridge may experience a bi-modal pattern: nucleation of isolated hot spots followed by spreading/coalescing of them via self-heating [Vina 2008].

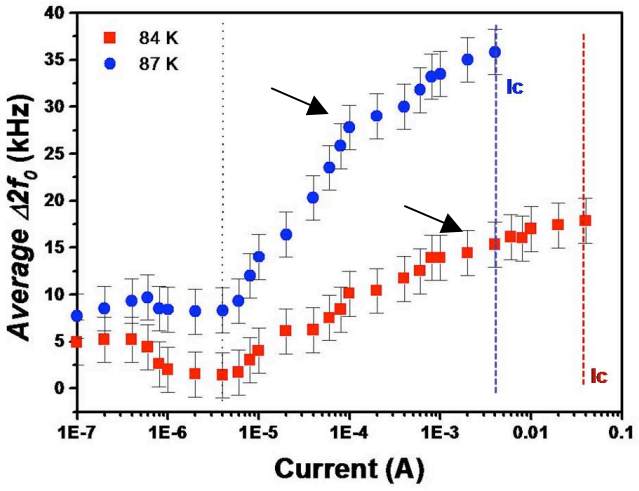

Fig 5.3. Average $\Delta 2f_0$ as a function of applied current over several decades of dissipation.

5.2 Time Evolution of Dissipation and Self-heating

To shed some light on this dynamic process, the self-heating effect was investigated. At fixed temperatures and bias currents, the time evolution of the transport voltage and the NSMM response were recorded simultaneously. In order to perform fast time-dependent data acquisition of the NSMM response, the alternative CW-mode type of microwave measurement described in the introduction was used to detect a reflected microwave signal, P_{ref}. Fig. 5.4 shows the time (t) evolution of the transport voltage and P_{ref} at a bias current I_{bias} = 0.6I_c at 84 K and 87 K, respectively. At 87 K, which is closer to T_c, the self-heating due to the presence of the I_{bias} forces the superconductor to quench much faster than at lower temperature as depicted by the V-t curves. The former took ~ 20 seconds and the latter, about 36 seconds. However, this transition is not shown in the P_{ref} curves. Instead, a monotonic increase in P_{ref} represents a continuously developing Joule heating caused by the constant I_{bias} as the sample is brought to quench. As the self-heating effect escalates, which is faster at temperatures closer to T_c, the dissipation

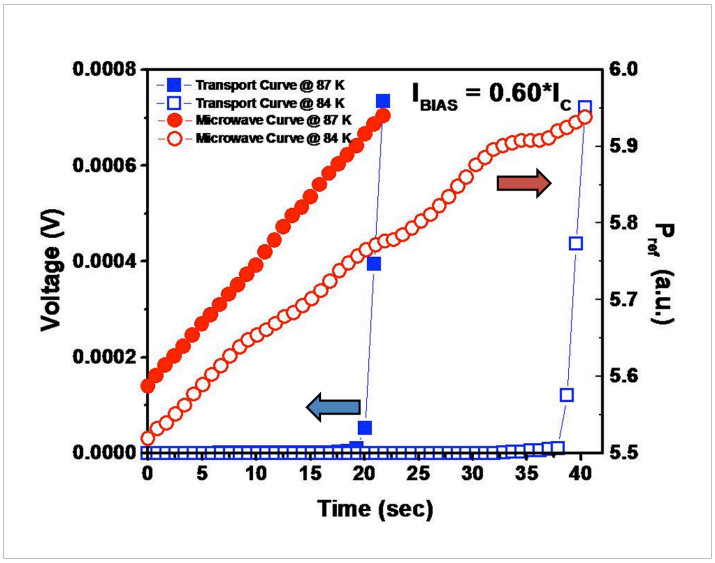

Fig 5.4. Time evolution of the dc transport voltage and the reflected microwave signal P_{ref} at temperatures 84 K and 87 K with I_{bias} = 0.6I_c.

becomes the driving force of thermal quench from superconducting to normal state. Since the transport technique measures a global effect across the length and width of the sample, it cannot sensitively detect or monitor dynamic development of localized dissipation until the global effect occurs. In contrast, NSMM can provide a quantitative monitoring of this dynamic process from the early stage of hot spot nucleation immediately after I_{bias} was applied, and the hot spot evolution until the quench occurs. Some subtle differences may be noticed in the P_{ref}-t curves in Fig. 5.4. At the higher temperature, the curve looks approximately straight while at the lower temperature, shallow steps appear. These steps become more prominent at even lower temperatures and therefore are the representative features of the P_{ref}-t curves. As we argued earlier, the steps in the dissipation with either increasing I_{bias} or time may have the same origin of a bi-modal dissipation evolution pattern: nucleation of isolated hot spots followed by spreading/coalescing of them via self-heating. At lower temperatures, the evolution of well-isolated hotspots is slower, allowing each mode of the bi-modal steps to be clearly detected. At higher temperatures, this effect is diminished because of faster hot spot growth. Also, spreading may occur in a continuous way and cannot be distinguished.

Fig. 5.5(a) shows two sets of time-evolution measurements of P_{ref} at different I_{bias} at 84 K and 87 K, respectively. The increasing I_{bias} not only speeds up the quench process but also diminishes the step features. This is probably due to the fact that increasing I_{bias} brings the sample closer to the superconducting-normal state transition

and self-heating is accelerated in a similar way to the elevated temperature case shown in Fig. 5.4. From curves in Fig. 5.5(a), the relationship between P_{ref} and the I_{bias} can be derived. As shown in Fig. 5.5(b), the dissipation taken at a selected moment ranging from 1.7 seconds to 6.0 seconds of the self-heating process increases monotonically with I_{bias}. In addition, the time needed for the self-heating to develop into a quench is depicted as a function of the normalized I_{bias} at 84 and 87 K, respectively, in Fig. 5.5(c). The curves can be fitted approximately by an exponentially decreasing function, indicating a large margin from the I_c could effectively increase the response time for protection of the HTS devices from quench-caused damages.

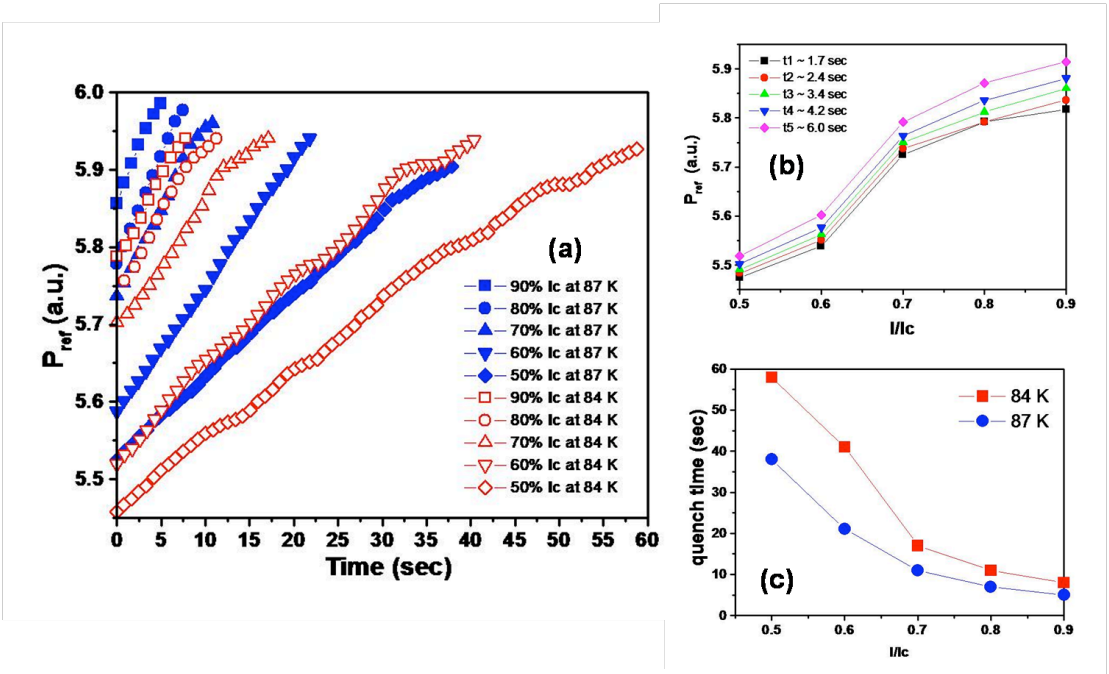

Fig 5.5 (a) Time evolution of P_{ref} taken at 84 K and 87 K using different values of the bias current. (b) Bias current dependence of P_{ref} at 84 K. (c) Bias current dependence of the quench time for samples at 84 K and 87 K.

5.3 Comparison of Low-level Dissipation at the Bulk and Grain Boundary Regions of a YBCO Microbridge

Figure 5.6 shows the two regions of interest where microwave measurements were obtained: (i) directly above the grain boundary and (ii) somewhere along the bulk of the thin film. To isolate the transport properties of the two regions corresponding to the distinct microwave measurements, two separate sets of electrical attachments to the microbridge constituting four-point probe configurations were placed by connecting thin gold wires to the silver contact pads using indium dots.

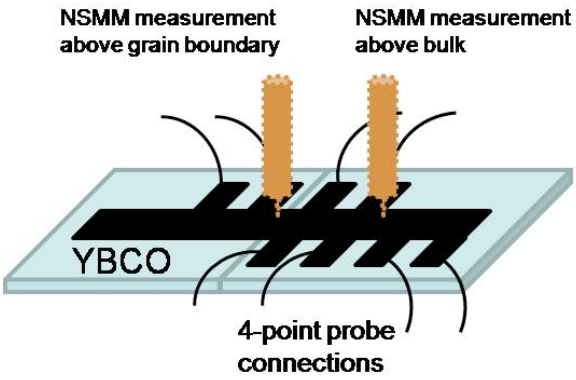

Fig. 5.6 Schematic of electrical connections and probe position during microwave measurements at GB and bulk regions of the sample.

Fig. 5.7(a) shows the changes in the 2nd harmonic frequency $\Delta(2f_0)$ with increasing bias current at 80 K for the 24^0 GB sample. The corresponding current-voltage (I-V) measurement conducted simultaneously with the microwave measurement is superimposed for comparison. The solid symbols represent the measurements obtained when the NSMM is directly above the GB and the open symbols represent measurements obtained when the NSMM is above the bulk. For our experimental set-up, 80 K is the lowest attainable temperature and represents a temperature limitation of our measurements. At this temperature, it was observed that

the sample is already quenched as depicted by the immediate increase in voltage across the sample upon application of low bias currents. This observation is confirmed by the corresponding monotonic increase in $\Delta(2f_0)$ at the GB spot as the bias current is ramped up. It has been confirmed numerous times that GBs with higher angles of misorientation significantly reduce the J_c of the sample. In this case, the transition from superconducting to normal state cannot even be observed because the temperature can no longer be decreased. When the measurements are obtained from the bulk of the sample, however, we notice no significant dissipation is detected by either technique at this current level, which is very far from the measured critical current of I_c = 23 mA at T = 80 K. This, thus, demonstrates the substantial effect of the high-angle GB misorientation on the superconducting properties of the sample. Figure 5.7(b) depicts the time evolution of the dissipation when a fixed bias

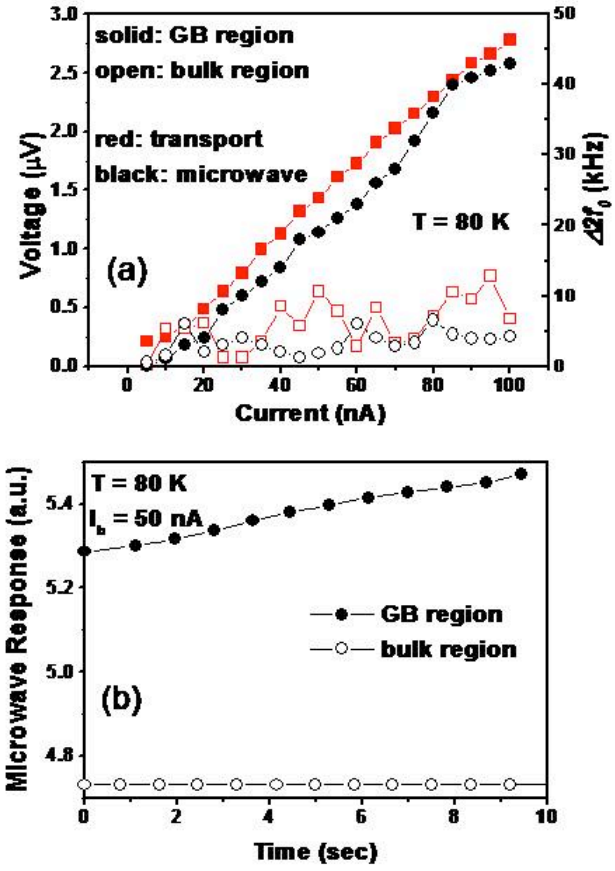

Fig 5.7. (a) Voltage and $\Delta 2f_0$ as a function of current at 80 K and 81 K obtained at the GB and bulk regions of sample with 24^0 misorientation. (b) Time evolution of the reflected microwave signal P_{ref} at T = 80 K and I_{bias} = 50 nA obtained at the GB and bulk regions of sample with 24^0 misorientation.

current of I_{bias} = 50 nA is applied to the sample at a fixed T = 80 K. This is obtained using the alternative CW-mode microwave measurement described above to accommodate the fast data acquisition requirement of the time-dependent evolution of the dissipation. The monotonic increase of P_{ref} at GB in a 10 second span with a very low applied current as compared to the constant value of P_{ref} obtained at the bulk, verifies that the sample is in its normal state almost immediately upon the current being supplied to the sample.

In order to observe the development of dissipation at the GB more carefully and deliberately, a sample with low-angle GB misorientation is needed. Fig. 5.8(a) depicts the changes in the 2nd harmonic frequency $\Delta(2f_0)$ with increasing bias current at 80 K and 81 K for the 9^0 GB sample along with the corresponding I-V curves when the NSMM is at the GB.

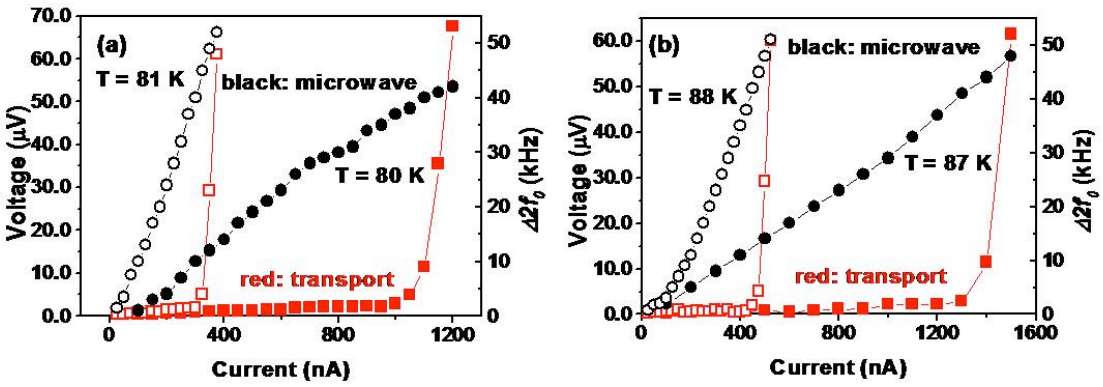

Fig 5.8. Voltage and $\Delta 2f_0$ as a function of current at obtained at the (a) GB and (b) bulk regions of sample with 9^0 misorientation. The open symbols represent data taken at the higher temperature while closed symbols represent those taken at lower temperatures. The data obtained for the bulk regions are at the reduced temperature-equivalent of the GB region where $T_{c(GB)}$ = 82 K.

The transition, which was not observed in the 24^0 sample, is now visible for these two temperature values and the critical current $\boldsymbol{I_c}$ was found to be 1050 nA and 300 nA for T = 80 K and 81 K, respectively. At a higher temperature, the dissipation develops faster, which is expected from less energy required to de-pin a vortex. Interestingly, the kink representing non-linear growth in dissipation observed previously appears again at lower temperatures. We speculated that this bi-modal pattern of dissipation development in an YBCO microbridge starts out by nucleation of isolated hot spots, followed by spreading/coalescing of them via self-heating. Thus, the same mechanism is observed at the GB. This is not unexpected since it is known that GBs provide weak links to supercurrent flow in a superconductor. As the applied current is increased, these weak links are more susceptible to nucleating hot spots and, therefore, dissipate at a much earlier stage than the rest of the sample. The fact that the growth is bi-modal further suggests that the nucleation of hot spots in the GB takes a more deliberate and slow process, possibly due to the low-angle of GB misorientation. Increasing the temperature by a degree Kelvin, though, eliminates this feature and the rate of dissipation development becomes more rapid and linear as the sample is closer to the transition. If the temperature is raised one more degree to 82 K, the transition disappears altogether and a similar quenched state, as in the 24^0 sample, is observed. Therefore, the temperature T = 82 K could essentially represent the critical temperature of the GB region as the sample exhibits dissipative behavior at the application of even a small bias current. In the bulk region, the absence of the grain boundary would definitely change the transport properties and conditions of the

sample. Thus, in order to make meaningful comparisons on how the development of dissipation occurs at the GB and away from the GB, the measurement needs to be at approximately the same conditions.

For a bulk region T_c = 89 K, the reduced temperature equivalent of 81 K and 80 K was found to be 87 K and 88 K respectively. Fig. 5.8(b) shows the corresponding $\Delta(2f_0)$-I and V-I curves obtained for 87 K and 88 K when the NSMM is in the bulk region of the YBCO sample. The transport I_c of 1300 nA and 400 nA for each temperature is only slightly higher than their GB reduced-temperature counterparts which suggests that the transport conditions are almost similar. The microwave measurement, however, reveals that the kinks or nonlinear features which were present in the development of dissipation at the GB are no longer visible. Since the reduced-temperature measurement was meant to isolate the effects of critical temperature at the GB and in the bulk regions, this discrepancy means that the temperature of the sample may be a significant factor in how dissipation develops at the grain boundary.

Figs. 5.9(a) and 5.9(b) depict the time-evolution of the transport voltage and the reflected microwave signal P_{ref} at fixed temperatures and bias currents for the GB and bulk regions, respectively. In both cases, the applied current is set at 60% of the critical current I_c and the reduced temperatures discussed above are also used.

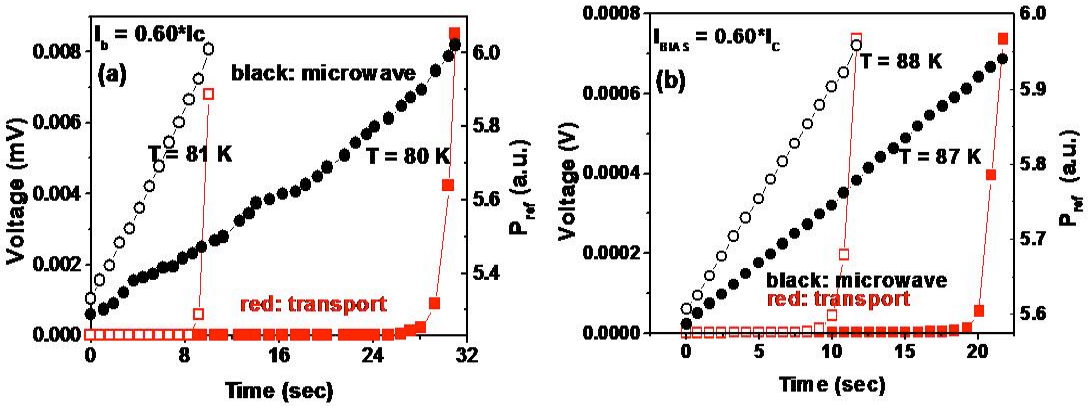

Fig 5.9 Time evolution of the reflected microwave signal P_{ref} obtained at the (a) GB and (b) bulk regions of sample with 9^0 misorientation. The open symbols represent data taken at the higher temperature while closed symbols represent those taken at lower temperatures. The data obtained for the bulk regions are at the reduced temperature-equivalent of the GB region where $T_{c(GB)}$ = 82 K.

As expected, self-heating due to the presence of I_{bias} forces the superconductor to quench much faster at higher temperatures. Also the monotonic increase in P_{ref} representing a continuously developing Joule heating caused by the constant I_{bias} is evident in both cases. Again, the subtle difference between the two sets of curves lies in the fact that the kinks/nonlinear features in the microwave curves obtained from the GB region are no longer seen in the those obtained from the bulk region.

In order to make more direct comparisons, the microwave curves are re-plotted without the transport curves in Fig. 5.10(a). The first observation that can be seen is the almost similar slopes of the solid-symbol curves (representing the lower reduced temperature). Thus, dissipation developing in either the bulk or GB regions occurs at almost the same rate but the mechanism of spread is different (as suggested by the kinks) and is dependent on the temperature of the sample.

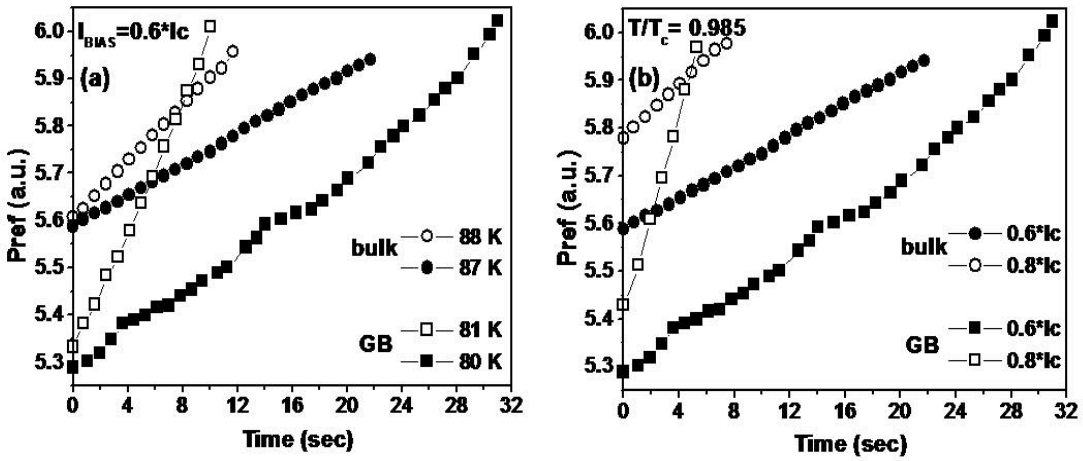

Fig 5.10 Microwave curves obtained from GB and bulk regions at (a) the same reduced current and (b) the same reduced temperature.

At the higher reduced-temperature (open-symbol curves), the obvious effect of the grain boundary can now be observed, which is to accelerate the development of dissipation in the particular localized area as shown in the steep slope of the microwave curve obtained in the GB region. Fig. 5.10(b) shows microwave curves all at the same reduced temperature but with applied bias currents of $\boldsymbol{I_{bias}} = 0.6\boldsymbol{I_c}$ and $\boldsymbol{I_{bias}} = 0.8\boldsymbol{I_c}$ compared with each other. Expectedly, the magnitude of the reflected power will be higher when the bias current is increased but the increased slope in the microwave curve obtained from the GB region also suggests that an increase in bias current gives a more rapid development in dissipation.

Finally, Fig. 5.11 shows the quench times, as given by the time-evolution measurements of $\boldsymbol{P_{ref}}$, for both the GB and bulk regions at different bias currents and at the two designated reduced temperature values. At reduced temperatures closer to

T_c (circle-symbol curves), the quench times for both GB and bulk regions at any bias current are almost the same. This statement takes into account that the T_c at the GB is less than the bulk T_c. As such, the GB region can then be considered as a 'bad' superconducting region where thermal quench can occur much earlier. Another interesting observation from this plot is the longer quench times for the GB region at bias currents below $0.7I_c$ when the temperature is less than the critical value. At these points, the difference in actual temperature between the GB and bulk regions still suppresses the development of dissipation in the localized areas. As the applied currents approach the value of I_c, the dissipation at the GB regions becomes more pronounced and the quench time approximates that of the bulk regions for the same reduced temperature.

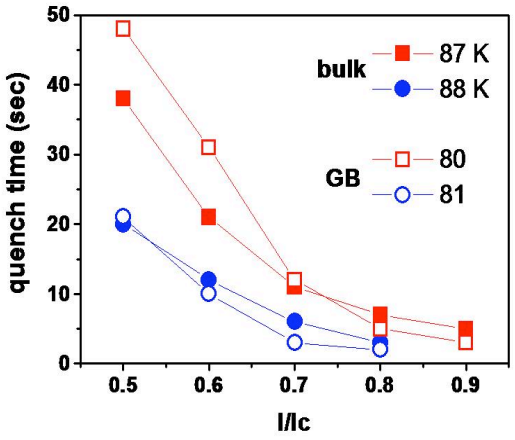

Fig 5.11. Bias current dependence of the quench times for sample with 9^0 misorientation obtained at GB and bulk regions obtained at different reduced temperatures.

Conclusions

A technique that combines a near-field scanning microwave microscope with a transport measurement system was developed to characterize dissipation in conducting and high-T_c superconducting films at variable temperatures. The proposed technique takes advantage of the unique capability of the microwave probe to function as both field emitter and detector to measure more than one physical property at a time. As a microwave emitter, the probe can be used to locally heat areas on the surface of a current-biased sample and map the current flow and dissipation. As a detector, the microwave probe can map the spatial non-uniformity in electrical properties of the sample by measuring the shifts in the resonant probe's microwave properties. Obtaining multiple sets of complementary information on the same sample area allows the correlation of different physical properties at the microscopic scale in both steady-state and dynamic modes.

The technique was first demonstrated on thin conducting films to determine the viability of using the microwave microprobe for imaging dissipation and non-uniformity. Qualitatively, macroscopic and microscopic defects on conducting films were clearly identified and imaged in the experiments using this technique. In order to have a quantitative understanding of the data, a theoretical model was developed,

simulated and compared with the experimental results. Considerable qualitative agreement between the model and the experimental results were observed in terms of bias current dependence, microwave input power dependence and line profiles of the induced voltage.

In addition, YBCO films with different kinds of mechanical defects and even secondary phase inclusions were prepared and scanned using the technique. Both microwave scans and induced voltage scans were able to identify mechanical defects with adequate sensitivity and resolution.

At low temperatures, the capability of the NSMM to detect low-level dissipation was tested by observing its response during the sample's transition from superconducting to normal state. The dynamics of thermal instability due to hot-spot nucleation was studied by measuring the time-dependent self-heating effect in response to a fixed temperature and applied current. When the HTS is far from the transition state, a bi-modal evolution of the thermal quench was observed beginning with a nucleation of a local hot spot followed by a spreading/coalescing of them via self-heating. As the sample is brought close to the transition by either increasing the temperature or applied current, this effect is diminished because of faster hot spot growth and continuous spread by self-heating. Measurements were done and observations were obtained for both the bulk and grain boundary regions of a superconductor.

Based on the results and observations obtained in this study, the combined NSMM – transport system proved to be a versatile multi-environment and multi-scale diagnostic and research tool to characterize dissipation in conducting and high-T_c superconducting films.

Further improvements and modifications to the system may be done to expand its capabilities, foremost and first of which is supplementing the measurements with a built-in variable magnetic field source. This will allow for a quantitative study of how much applied magnetic fields can affect the development of local dissipation.

Bibliography

Abu-Teir M., Golosovsky M., Davidov D., Frenkel A. and Goldberger H. *Rev. Sci. Instrum.* **72**, 2073 (2001).

Abraimov D., Feldmann D.M., Polyanskii A.A., Gurevich A., Daniels G., Larbalestier D.C., Zhuravel A.P. and Ustinov A.V. *Appl. Phys. Lett.* **85**, 2568 (2004).

Aga R.S. *PhD Dissertation* University of Kansas (2003).

Aga R.S., Wang X., Dizon J.R., Noffsinger J. and Wu J.Z. *Appl. Phys. Lett* **86**, 234101 (2005).

Anlage, S.M., Steinhauer, D.E., Vlahacos, C.P., Feenstra, B.J., Thanawalla, A.S., Hu, W., Dutta, S.K. and Wellstood, F.C. *IEEE Trans. Appl. Supercond*. **9**, 4127 (1999).

Ash E.A. and Nicholls G. *Nature* **237**, 510 (1972).

Babcock, S.E. and Larbalestier, D.C. *J. Phys. Chem Solids* **55**, 1125-1136 (1994).

Bellis, R.H. and Iwasa, Y. *Cryogenics* **34**, 129 (1994).

Binnig G., Rohrer H., Gerber C., and Weibel E. *Physica* **109 & 110B** 2075 (1982).

Binnig G., Quate C.F. and Gerber C. *Phys. Rev. Lett.* **56**, 930 (1986).

Browning, N.D. and Pennycook, S.J. *J. Phys. D: Appl. Phys.* **29**, 1779-1798 (1996).

Browning, N.D., Buban, J.P., Nellist, P.D., Norton, D.P., Chisholm, M.F., and Pennycook, S.J. *Phys. C* **294**, 183-193 (1998).

Bosman H., Lau Y.Y. and Gilgenbach R.M. *Appl. Phys. Lett*. **82**, 1353 (2003).

Chaudhari, P., Mannhart, J., Dimos, D., Tsuei, C.C., Chi, J. Oprysko, M.M., and Scheuermann, M. *Phys. Rev. Lett* **60**, 1653 (1988).

Copetti, C.A., Ruders, F., Oelze, B., Buchal, Ch., Kabius, B., and Seo, J.W. *Phys. C* **253**, 63-70 (1995).

Copty A., Sakran F., Golosovsky M., Davidov D. and Frenkel A. *Appl. Phys. Lett*. **84**, 5109 (2004)[a].

Copty A., Golosovsky M., Davidov D. and Frenkel A. *IEEE Trans. Microwave Theory Tech.*. **52**, 1957 (2004)[b].

Dimos, D., Chaudhari, P., Mannhart, J., and LeGoues, F.K. *Phys. Rev. Lett* **61**, 219-222 (1988).

Dimos, D., Chaudhari, P. and Mannhart, J. *Phys. Rev. B* **41**, 4038-4049 (1990).

Divin Y.Y. and Shadrin P.M. *Physica C* **232**, 257 (1994).

Duewer F., Gao C., Takeuchi I. and Xiang X.D. *Appl. Phys. Lett.* **74**, 2696 (1999).

Durig U., Pohl D.W. and Rohner F. *J. Appl. Phys*. **59**, 3318 (1986).

Dutta S.K., Vlahacos C.P., Steinhauer D.E., Thanawalla A.S., Feenstra B.J., Wellstood F.C., Anlage S.M. and Newman H.S. *Appl. Phys. Lett.* **74**, 156 (1999).

Feng, Y.J., Wu, L.Y., Wang, L., Jiang, T., Kang, L., Yang, S.Z. and Wu, P.H. *IEEE Trans. Appl. Supercond*. **13**, 2901 (2003).

Feldmann D.M., Reeves J.L., Polyanskii A.A., Kozlowski G., Biggers R.R., Nekkanti R.M., Maartense I., Tomsic M., Barnes P., Oberly C.E., Peterson T.L., Babcock S.E. and Larbalestier D.C. *Appl. Phys. Lett.* **77**, 2906 (2000).

Gao C., Wei T., Duewer F., Lu Y. and Xiang X.D. *Appl. Phys. Lett*. **71**, 1872 (1997).

Gao C., Duewer F., Lu Y., Xiang X.D. *Appl. Phys. Lett.* **73**, 1146 (1998).

Gao, Y., Merkle K.L., Bai, G., Chang, L.M., and Lam, D.J. *Phys C* **174**, 1-10 (1991).

Grabovickic, R., Lue, J.W., Gouge, M.J., Demko, J.A., and Duckworth, R.C. *IEEE Trans. Appl. Supercond.* **13**, 1726 (2003).

Golosovsky M. and Davidov D. *Appl. Phys. Lett*. **68**, 1579 (1996).

Gurevich A. *Appl. Phys. Lett.* **78**, 1891 (2001).

Hamers R.J., Tromp R.M. and Demuth J.E. *Phys. Rev. Lett.* **56**, 1972 (1986).

Harrabi, K., Cheenne, N., Lam, V.D., Ladan, F.R., and Maneval, J.P. *Jour. of Supercond*. **14**, 325 (2001).

Hilgenkamp, H., Mannhart, J. and Mayer, B. "*Phys.Rev. B* **53**, 14586 – 14593 (1996).

Hilgenkamp, H. and Mannhart, J. *Rev. Modern Phys.* **74**, 485-549 (2002).

Hong S., Kim J., Park W. and Lee K. *Appl. Phys. Lett.* **80**, 524 (2002).

Hu W., Thanawalla A.S., Feenstra B.J., Wellstood F.C. and Anlage S.M. *Appl. Phys. Lett.* **75**, 2824 (1999).

Hug H.J., Stiefel B., van Schendel P.J., Moser A., Martin S.and Guntherodt H.J. *Rev. Sci. Instrum.* **70**, 3625 (1999).

Humphreys, R.G. and Edwards, J.A. *Phys. C* **210**, 42-54 (1993).

Imtiaz A. and Anlage S.M. *Ultramicroscopy* **94**, 209 (2003).

Ishiyama, A., Tanaka, Y., Ueda, H., Shiohara, Y., Machi, T., Iijima, Y., Saitoh, T., Kashima, N., Mori, M., Watanabe, T., and Nagaya, S. *IEEE Trans. Appl. Supercond.* **17**, 3509 (2007).

Karapetrov G., Cambel V., Kwok W.K., Nikolova R., Crabtree G.W., Sheng H. and Beal V.W. *J. Appl. Phys.* **86**, 2682 (1999).

Kim J., Kim M.S., Lee K., Lee J., Cha D. and Friedman B. *Meas. Sci. Technol.* **14**, 7 (2003)[a].

Kim J., Kim M.S., Kim H., Song D., Lee K. and Friedman B. *Appl. Phys. Lett.* **83**, 1026 (2003)[b].

Kim M.S., Kim J., Kim H., Kim S., Yang J., Yoo H., Kim S., Lee K., and Friedman B. *Rev. Sci. Instrum.* **75**, 684 (2004).

Kim S., Yoo H., Lee K., Friedman B., Gaspar M.A. and Levicky R. *Appl. Phys. Lett.* **86**, 153506 (2005).

Kiss T., Inoue M., Yasunaga M., Tokutorni H., Iijima Y., Kakimoto K., Saitoh T., Tokunaga Y., Izumi T., Shiohara Y. *IEEE Trans. Appl. Supercon.* **15**, 3656 (2005).

Klein B.E., Seo S., Kwon C., Park B.H. and Jia Q.X. *Rev. Sci. Instrum.* **73**, 3692 (2002).

Lann A.F., Abu-Teir M., Golosovsky M., Davidov D., Goldgirsch A., and Beilin V. *Appl. Phys. Lett.* **75**, 1766 (1999)[a].

Lann A.F., Abu-Teir M., Golosovsky M., Davidov D., Djordjevic S., Bontemps N. and Cohen L.F. *Rev. Sci. Instrum.* **70**, 4348 (1999)[b].

Larbalestier, D. Gurevich, A., Feldman, D.M., Polyanskii, A. *Nature* **414**, 368-377 (2001).

Lee S.C., Vlahacos C.P., Feenstra B.J., Schwartz A., Steinhauer D.E., Wellstood F.C. and Anlage S.M. *Appl. Phys. Lett.* **77**, 4404 (2000).

Lee S.C. and Anlage S.M. *Appl. Phys. Lett.* **82**, 1893 (2003).

Lehndorff, B. R. *High-T_c Superconductors for Magnetic and Energy Technology: Fundamental Aspects.* Springer, Berlin (2001).

Lu Y., Wei T., Duewer F., Lu Y., Ming N., Schultz P.G. and Xiang X.D. *Science* **276**, 2004 (1997).

Lewis A., Issacson M., Haratounian A. and Murray A. *Ultramicroscopy* **13**, 227 (1984).

Mamin H.J., Gueturer P.H. and Rugar D. *Phys. Rev. Lett.* **65**, 2418 (1990).

Mannhart, J., Mayer, B and Hilgenkamp, H. *J. Phys. B* **101**, 175– 179 (1996).

Marx A., Husemann K.D., Mayer B., Nissel T., Gross R., Verhoeven M.A. and Gerritsma G. *Appl. Phys. Lett.* **64**, 241 (1994).

Meyer, E., Hug, H.J., and Bennewitz, R. *Scanning probe microscopy: the lab on a tip.* Springer, Berlin (2004).

Mishra S. *Master's Thesis* University of Kansas (2005).

Mishra S., Dizon J.R., Aga R.S. and Wu J.Z. *to appear in J. Appl. Phys.* (2006).

Pohl D.W., Denk W. and Lanz M. *Appl. Phys. Lett*. **44**, 651 (1984).

Pozar D.M. *Microwave Engineering*. Addison-Wesley Publishing Co. Inc. (1990).

Roseman M. and Grutter P. *J. Appl. Phys.* **91**, 8840 (2002)

Rosner B.T. and van der Weide D.W. *Rev. Sci. Instrum.* **73**, 2505 (2002).

Rous P.J., Yongsunthon R., Stanishevsky A., and Williams E.D. *J. Appl. Phys.* **95**, 2477 (2004).

Schuermann M., Lhota J.R., Kuo P.K. and Chen J.T. *Phys. Rev. Lett.* **50**, 74 (1983).

Shadrin P.M. and Divin Y.Y. *Physica C* **297**, 257 (1998).

Soohoo R.F.. *J. Appl. Phys*. **33**, 1276 (1962).

Steinhauer D.E., Vlahacos C.P., Dutta S.K., Wellstood F.C. and Anlage S.M. *Appl. Phys. Lett.* **71**, 1736 (1997).

Steinhauer D.E., Vlahacos C.P., Dutta S.K., Feenstra B.J., Wellstood F.C. and Anlage S.M. *Appl. Phys. Lett.* **72**, 861 (1998).

Steinhauer D.E., Vlahacos C.P., Wellstood F.C., Anlage S.M., Canedy C, Ramesh R., Stanishevsky A. and Melngailis J. *Appl. Phys. Lett*. **75**, 3180 (1999).

Steinhauer D.E., Vlahacos C.P., Wellstood F.C., Anlage S.M., Canedy C, Ramesh R., Stanishevsky A. and Melngailis J. *Rev. Sci. Instrum.*. **71**, 2751 (2000).

Steinhauer D.E. and Anlage S.M. *J. Appl. Phys.* **89**, 2314 (2001).

Sugimoto A., Yamaguchi T., Iguchi I. *Appl. Phys. Lett.* **77**, 3069 (2000).

Synge E.H., *Philos. Mag*. **6**, 356 (1928).

Tabib-Azar M., Shoemaker N.S., Harris S. *Meas. Sci. Technol.* **4**, 583 (1993).

Tabib-Azar M., Su D.P., Pohar A., LeClair S.R., and Ponchak G. *Rev. Sci. Instrum*. **70**, 1725 (1999) [a].

Tabib-Azar M., Pathak P.S., Ponchak G., and LeClair S.R. *Rev. Sci. Instrum*. **70**, 2783 (1999) [b].

Tabib-Azar M., Akinwande D., Ponchak G., and LeClair S.R. *Rev. Sci. Instrum*. **70**, 3083 (1999) [c].

Tabib-Azar M., Akinwande D., Ponchak G., and LeClair S.R.. *Rev. Sci. Instrum*. **70**, 3381 (1999) [d].

Tabib-Azar M., Ciocan R., Ponchak G., and LeClair S.R. *Rev. Sci. Instrum*. **70**, 3387 (1999) [e].

Tabib-Azar M. and Sutapun B. *Rev. Sci. Instrum*. **70**, 3707 (1999) [f].

Tabib-Azar M., Katz J.L. and LeClair S.R. *IEEE Trans. Instrum. Meas.* **48**, 1111 (1999) [g].

Tabib-Azar M. and Akinwande D. *Rev. Sci. Instrum*. **71**, 1460 (2000).

Talley C.E., Lee M.A. and Dunn R.C. *Appl. Phys. Lett.* **72**, 2954 (1998).

Thompson, J.R., Polat, O., Christen, D.K., Kumar, D., Martin, P.M., and Sinclair, J.W. *Appl. Phys. Lett*. **93**, 042506 (2008).

Tien, C.L., Flik, M.I. and Phelan, P.E. Cryogenics **29**. 602 (1989).

Tselev A., Anlage S.M., Christer H.M., Moreland R.L., Talanov V.V. and Schwartz A.R. *Rev. Sci. Instrum.* **74**, 3167 (2003).

Verebelyi, D.T., Christen, D.K., Feenstra, R., Cantoni, C., Goyal, A., Lee, D.F., Paranthaman, M., Arendt, P.N., DePaula, R.F., Groves, J.R., and Proteau, C. *Appl. Phys. Lett.* **76**, 1755-1757 (2000).

Vina, J., Gonzales, M.T., Ruibal, M., Curras, S.R., Viera, J.A., Maza, J. and Vidal, F. *Appl. Phys. Lett.* **93**, 042506 (2008).

Vlahacos C.P., Black R.C., Anlage S.M., Amar A., Wellstood F.C. *Appl. Phys Lett*. **69**, 3272 (1996).

Vlahacos C.P., Steinhauer D.E., Dutta S.K., Feenstra B.J. and Anlage S.M. *Appl. Phys. Lett.* **72**, 861 (1998).

Wei T., Xiang X.D., Wallace-Freedman W.G. and Schultz P.G. *Appl. Phys. Lett*. **68**, 3506 (1996)

Wu, L.Y., Feng, Y.J., Wang, K.L., Jiang, T., Kang, L., Yang, S.Z. and Wu, P.H. *IEEE Trans. Supercond. Sci and Technol*. **15**, 1771 (2002).

Yongsunthon R., Stanishevsky A., Williams E.D. and Rous P.J. *Appl. Phys. Lett.* **82**, 3287 (2003).

Weisendanger, R. *Scanning probe microscopy and spectroscopy: methods and applications.* Cambridge Univ. Press, Cambridge (1994).